Universidad del País Vasco Euskal Herriko Unibertsitatea

CIC nanoGUNE
MEMBER OF BASQUE RESEARCH & TECHNOLOGY ALLIANCE

MODELS OF RADIOLYSIS IN LIQUID REACTORS FOR TRANSMISSION ELECTRON MICROSCOPY

Giuseppe De Salvo

A DISSERTATION

in

Physics of Nanostructures and Advanced Materials

Presented to the Faculties of the University of Basque Country

in

Partial Fulfillment of the Requirements for the

Degree of Doctor of Philosophy

2025

Supervisor of Dissertation

Prof. Andrey Chuvilin

Ikerbasque Research Professor

Co-Supervisor of Dissertation

Dr. Stefan Merkens

Post Doctoral Researcher

Le acque del golfo rinfreschino il tuo spirito,

i venti della piana inebrino il tuo cammino,

le montagne sinuose elevino i tuoi sogni,

le spiagge setose accolgano i tuoi passi.

A mio padre, Francesco, dedico questo libro.

Giuseppe

ACKNOWLEDGEMENT

Completing this thesis stands as one of my greatest achievements, a work that would not have been possible without the synergy of many individuals whose support, guidance, and collaboration have been indispensable throughout this journey. I am deeply grateful to everyone who contributed to its success, and I would like to take this opportunity to individually acknowledge them.

I sincerely acknowledge Jose Maria Pitarke De la Torre as tutor of my Thesis and director of the research centre CIC Nanogune, where I had the opportunity to carry out my research. The support and resources provided by the institution have been invaluable in the development of this work.

I extend my deepest gratitude to my supervisor, Prof. Andrey Chuvilin, whose expertise, and encouragement have been fundamental for solving the problems that arose during the work. I also take the chance to deeply thank Dr. Stefan Merkens, for his wise and fruitful supervision even tough being younger than its student! Their feedback and support have significantly shaped my understanding and approach to science.

I would also like to express my appreciation to the entire EMers (Electron Microscopers) group, whose collaboration, discussions, and mountain adventures shared with Chris and Evgeny and again Stefan have enriched my view to the world, from towering peaks to the dance of atoms below!

And how can I forget all my beloved colleagues, who supported my craziness, whose sweet words lifted me up to conquer the title? They never chickened out on any occasion and, most importantly, fed me intensively. Now it's time to list them and give their acknowledgment: Konstantina, Karina, and Kristina (A.K.A. the triple K) for their alcoholic, food, and party plans consulting; Diana for her mental health support; Friederich for being inspirational in the world of overall sports activities; Theo for the shared moments in the crazy desks island, where we learned that the audio of videos must sometimes be turned off... (cough, cough). Arantxa, for being the sweetest creature on Earth, and Federico, the Venetian hardcore

soulmate I miss from my Paduans adventures. Speaking of Italians... let's talk about Gabriele, the love problems counselor (always failing in his consultancy), and his other half, Katerina, the strong Balkan support that should never be missing from the friend pot. And now, the ones who left a huge hole, mostly in the joke department of this journey, which we desperately needed between scientific tasks: Natalia and Mauro as the main protagonists, followed by the rest of the troupe—Maricarmen, Maiara, Jon, Marina, Stefan (again), Susan, Matteo, Evangelis, and Steven. And many others whom I forgot—since the PhD started, I lost my memory!

Now it's the moment to acknowledge my flatmates, who also mean family, home, and many other sentimental things I'm bad at describing. Jules, for delighting me with the rhythm of harp sounds, thank God you chose this instrument. Pablo, for his silent presence, always appreciated, and for the many kilometers shared, from the lost highway to Santiago to the broken, rocky downhill trails in the Basque lands. Finally, 'The' Vincent, who was a great counselor in all fields and a poteau, introducing me to proper French and finally erasing my Gen Z vocabulary, which had been inculcated by Jules.

Last but not least, the friends, whom I will list in groups to keep it short (WhatsApp groups): Hippie Squad, as the name suggests, for the dirty, nature-filled, and healthy adventures. The San Fausto and Bicicleteros fellows for the comparable adrenaline left on the rocks. The Pintxo Mafia, which I recognize as a great starting fusion of Basque and Italian cultures. And even if they were not part of the Basque adventure, the 3 Coinqui + 3, who are always in my heart, and the FantaArtePoveri for the battles in the Russanis league and for reminding me of my roots.

Special acknowledgment to a person, Marie, who has been by my side through a great part of this journey. She has been my support and has touched and transformed the person I have become in these last years. Now, we finally share of our success, and we can smile together.

Finally, a few words for the most important people in my life—my brother Antonio and my mother Rachele. I will always be with you, to spend moments with you, even in the battles

I face throughout my life.

ABSTRACT

Liquid-phase transmission electron microscopy (LP-TEM) has revolutionised the ability to directly observe dynamic nanoscale processes in liquids under native sample conditions. This achievement was catalysed by advancements in the microfabrication of fluidic, heating, and biasing holders, along with the development of liquid cells equipped with electron-transparent membranes such as silicon nitride and graphene. These innovations enable liquid samples to be encapsulated within the high vacuum of an electron microscope. As a result, LP-TEM has propelled the monitoring of liquid specimens, including colloidal nanocrystals, polymers, minerals, and viruses, uncovering insights into chemical and physical phenomena previously beyond reach. However, LP-TEM experiments face challenges from electron beam-induced effects, particularly radiolysis, which generates reactive chemical species that are likely to cause artefacts. This has created a pressing demand for a better understanding, and ultimately mitigation, of these effects.

Given the intricacy of measuring radiolytic species in LP-TEM setups, computational modelling has played a crucial role. In 2014, Schneider et al. introduced a basic numerical radiolysis reaction kinetic model. The model was constructed from the vast knowledge on radiolysis acquired in the context of nuclear reactor research. Over the past decade, the model has been adapted to address a series of fundamental questions, but concerns regarding its appropriateness for describing experimental realities have been growing.

There are two major challenges regarding the modelling of radiolysis in LP-TEM. The first is related to oversimplified assumptions that fail to capture the complexity of an experimental setup. Existing models often assume a homogeneous irradiation, overlooking the heterogeneity of chemistry and mass transport phenomena. Manufacturers are continuously pushing the boundaries of fluidic reactor designs, creating environments dominated by convection, diffusion, or a combination of both. Accurately modelling these physics is critical to bridging the gap between purely kinetic models and the complex physical phenomena observed in LP-TEM experiments. Additionally, a commonly used operational mode in experiments, such as scanning TEM (STEM), complicate the boundary problem by introducing a scan-

ning beam across the liquid. This lead to spatial and temporal variations in the evolution of radiolysis.

Secondly, the initial conditions used in existing radiolysis models require verification across theoretical aspects. The chemical evolution of reactions within the first microseconds after irradiation is crucial for determining radiolysis yields. Current theoretical assumptions are based on low irradiation density techniques, which differ significantly from the high electron irradiation density typical in electron microscopy. A re-evaluation of the spatio-temporal dynamics of early radiolysis under high-density conditions is necessary to confirm whether the yields derived from low-density studies remain valid.

This thesis aims to contribute to the understanding of radiolysis by developing advanced simulation tools, thereby advancing LP-TEM into a more quantitative technique. The focus is on developing spatial and temporal numerical models that integrate diffusion, convection, and reaction kinetics to replicate the radiochemical environment within the liquid cell under electron microscopy irradiation.

A versatile and semi-automatic computational approach is introduced that expands existing radiochemical models by integrating coupled differential equation systems through finite element methods (FEM). This approach reproduces expanded experimental scenarios, including high electron density irradiation, liquid cell geometries, the mass transport regimes, and both stationary and scanning irradiation (i.e., TEM and STEM mode). This thesis establishes procedures to validate the implementation of realistic radiolysis models and explores strategies to reduce computational costs. The analysis of these models has led to new insights in the field of radiolysis, such as the impact of flow on the chemical network, correlations with experiments reporting anisotropies at liquid-sample interfaces driven by scanning mode, and predictions regarding the behaviour of open and closed cells, as well as flow-based scavenging strategies. Furthermore, the development of methodologies for dose-dependent radiolysis quantification has demonstrated applicability across the irradiation regimes of TEM and STEM, offering significant advances for estimating microsecond radiolytic yields.

The thesis guides the reader from the foundational theory of radiolysis to the development and application of the simulation framework. Initial chapters provide an overview of electron-sample interactions in liquids and established methodologies for radiolysis modelling. Subsequent chapters detail technical implementations, validate models against references and experimental data, and highlight discoveries made through novel simulations. By addressing both theoretical and correlative challenges, this work establishes a groundwork for computational radiolysis research, offering tools to advance automatic numerical modelling and the know-how necessary to expand the framework for more precise solutions in the field of LP-TEM.

RESUMEN

La microscopía electrónica de transmisión en fase líquida (LP-TEM, por sus siglas en inglés) ha revolucionado la capacidad de observar directamente procesos dinámicos a escala nanométrica en líquidos bajo condiciones nativas de la muestra. Este logro ha sido impulsado por avances en la microfabricación de soportes fluidodinámicos, térmicos y de polarización, junto con el desarrollo de celdas líquidas equipadas con membranas transparentes a los electrones, como el nitruro de silicio y el grafeno. Estas innovaciones permiten encapsular muestras líquidas dentro del alto vacío de un microscopio electrónico. Como resultado, la LP-TEM ha impulsado el monitoreo de especímenes líquidos, incluidos nanocristales coloidales, polímeros, minerales y virus, revelando conocimientos sobre fenómenos químicos y físicos que antes estaban fuera de alcance. Sin embargo, los experimentos de LP-TEM enfrentan desafíos derivados de los efectos inducidos por el haz de electrones, en particular la radiólisis, que genera especies químicas reactivas propensas a causar artefactos. Esto ha generado una demanda urgente de una mejor comprensión y, en última instancia, de la mitigación de estos efectos.

Dada la complejidad de medir las especies radiolíticas en configuraciones de LP-TEM, la modelización computacional ha desempeñado un papel crucial. En 2014, Schneider et al. introdujeron un modelo numérico básico de cinética de reacción de radiólisis. Este modelo se construyó a partir del vasto conocimiento sobre radiólisis adquirido en el contexto de la investigación en reactores nucleares. Durante la última década, el modelo se ha adaptado para abordar una serie de cuestiones fundamentales, pero han ido en aumento las preocupaciones sobre su idoneidad para describir las realidades experimentales.

Existen dos desafíos principales en la modelización de la radiólisis en LP-TEM. El primero está relacionado con suposiciones demasiado simplificadas que no capturan la complejidad de un experimento. Los modelos actuales suelen asumir una irradiación homogénea, sin considerar la heterogeneidad de los fenómenos químicos y de transporte de masa. Los fabricantes están ampliando continuamente los límites del diseño de reactores fluidodinámicos, creando entornos dominados por la convección, la difusión o una combinación de ambas.

La modelización precisa de estas físicas es crucial para cerrar la brecha entre los modelos puramente cinéticos y los fenómenos físicos complejos observados en los experimentos de LP-TEM. Además, un modo de operación común en experimentos, como la microscopía electrónica de transmisión en modo de barrido (STEM), complica aún más el problema de los límites al introducir un haz de electrones que escanea la muestra líquida, lo que genera variaciones espaciales y temporales en la evolución de la radiólisis.

En segundo lugar, las condiciones iniciales utilizadas en los modelos existentes de radiólisis requieren una verificación desde un punto de vista teórico. La evolución química de las reacciones en los primeros microsegundos tras la irradiación es crucial para determinar los rendimientos de radiólisis. Las suposiciones teóricas actuales se basan en técnicas de baja densidad de irradiación, que difieren significativamente de la alta densidad de electrones típica de la microscopía electrónica. Es necesario revaluar la dinámica espacio-temporal de la radiólisis temprana en condiciones de alta densidad para confirmar si los rendimientos derivados de estudios en baja densidad siguen siendo válidos.

Esta tesis tiene como objetivo contribuir a la comprensión de la radiólisis mediante el desarrollo de herramientas avanzadas de simulación, promoviendo así el avance de la LP-TEM hacia una técnica más cuantitativa. El enfoque se centra en el desarrollo de modelos numéricos espacio-temporales que integren difusión, convección y cinética de reacción para replicar el entorno radioquímico dentro de la celda líquida bajo irradiación en microscopía electrónica.

Se introduce un enfoque computacional versátil y semiautomático que amplía los modelos radioquímicos existentes mediante la integración de sistemas de ecuaciones diferenciales acopladas a través de métodos de elementos finitos (FEM). Este enfoque permite reproducir escenarios experimentales ampliados, incluidos regímenes de alta densidad de electrones, geometrías de celdas líquidas, regímenes de transporte de masa y modos de irradiación tanto estacionarios como de barrido (es decir, TEM y STEM). La tesis establece procedimientos para validar la implementación de modelos realistas de radiólisis y explora estrategias para reducir los costos computacionales. El análisis de estos modelos ha llevado a nuevos avances en el campo de la radiólisis, como el impacto del flujo en la red química, correlaciones con

experimentos que reportan anisotropías en las interfaces líquido-muestra impulsadas por el modo de barrido y predicciones sobre el comportamiento de celdas abiertas y cerradas, así como estrategias de eliminación de especies reactivas basadas en flujo. Además, el desarrollo de metodologías para la cuantificación de la radiólisis en función de la dosis ha demostrado su aplicabilidad en los regímenes de irradiación de TEM y STEM, proporcionando avances significativos para la estimación de los rendimientos radiolíticos en microsegundos.

La tesis guía al lector desde la teoría fundamental de la radiólisis hasta el desarrollo y la aplicación del marco de simulación. Los capítulos iniciales presentan una visión general de las interacciones electrón-muestra en líquidos y las metodologías establecidas para la modelización de la radiólisis. Los capítulos posteriores detallan las implementaciones técnicas, validan los modelos con datos experimentales y de referencia, y destacan los descubrimientos obtenidos mediante simulaciones novedosas. Al abordar tanto los desafíos teóricos como los correlativos, este trabajo establece una base para la investigación computacional en radiólisis, proporcionando herramientas para avanzar en la modelización numérica automática y el conocimiento necesario para ampliar el marco hacia soluciones más precisas en el campo de la LP-TEM.

TABLE OF CONTENTS

ACKNOWLEDGEMENT iii

ABSTRACT vi

RESUMEN ix

CHAPTER 1 : INTRODUCTION 1

1.1 General Introduction 1

1.2 Scope & Objectives. 4

1.3 Structure of the Thesis. 6

1.4 List of Dissemination 8

CHAPTER 2 : ELECTRON-SAMPLE INTERACTIONS IN LIQUID PHASE TRANSMISSION ELECTRON MICROSCOPY 10

2.1 Electrons as Probes of Atomic Matter 10

2.1.1 Resolution Considerations and Imaging Principles 10

2.1.2 Electrons-Sample Interactions 12

2.1.3 Radiation Damage In Electron Microscopy 13

2.2 Radiolysis of Water 15

2.2.1 Historical Remark 15

2.2.2 Radiolysis of Water - Basics 16

2.2.3 From Heterogeneous to Homogeneous Models 17

2.2.4 Radiolysis Yields Estimation Models 22

2.2.5 Homogeneous Kinetic Modelling 25

2.3 Radiolysis Modelling in the context of LP-TEM 27

2.3.1 Radiolysis Models Extensions 30

2.3.2 Impact of Dose Rate on Radiolytic Yields in TEM. 32

2.3.3 Other Simulation and Experimental Attempts 33

CHAPTER 3 : METHODOLOGY OF A RADIOLYSIS MODEL IMPLEMENTATION. 35
3.1 Introduction 35
3.2 Geometric Modelling 37
3.3 Physics Modelling 39
3.3.1 Chemical Reactions 39
3.3.2 Radiolytic Generation 41
3.3.3 Convection-Diffusion-Reactions Coupling. 43
3.3.4 Diffusion Mass Transport 44
3.3.5 Fluid Dynamics 47
3.4 Mathematics 51
3.4.1 Meshing 51
3.5 Informatics 55
3.5.1 Scientific Programming 55
3.5.2 Data Analysis 56

CHAPTER 4 : A FRAMEWORK FOR ANALYSING DIFFUSION AND FLOW DYNAMICS IN LIQUID CELL GEOMETRIES 62
4.1 Introduction 62
4.2 Non-Uniform Irradiation Modelling 65
4.2.1 The Reaction-Diffusion Model 67
4.3 The Reaction-Diffusion-Convection Models 69
4.4 The Model Framework for LP-TEM Geometries 71
4.5 Radiolysis & Transport Predictions 74
4.5.1 Exploring Comparisons in Closed vs. Open Cells 74
4.5.2 Spatial Reaction Network Separation 76
4.5.3 Practical Implications for Experiments 82
4.5.4 Effect of Flow on Species Concentrations 87

CHAPTER 5 : PREDICTIVE SCANNING TEM MODELLING 94
5.1 Introduction 94

5.2 Building the STEM Radiolysis Model . . . 97
5.2.1 NanoRad-STEM: A Subroutine for Radiolysis Modeling . . . 102
5.3 Anisotropic Dissolution in Silica Nanoparticles . . . 104
5.3.1 Experimental observations, hypothesis, chemistry . . . 104
5.3.2 Model Description . . . 106
5.3.3 Results and Discussion . . . 109
5.3.4 Conclusions . . . 111

CHAPTER 6 : RADIOLYSIS MODELLING AT HIGH DENSITY AND ENERGY ELECTRON FLUXES . . . 113
6.1 Introduction . . . 113
6.2 Short Time Radiolysis Kinetics . . . 114
6.3 The "Spur" model . . . 116
6.4 Model Validation . . . 121
6.5 High LET Simulations - Results Discussion . . . 126
6.6 Conclusions . . . 132

CHAPTER 7 : SUMMARY AND OUTLOOK . . . 134
7.1 Development of radiolysis modelling framework . . . 134
7.1.1 Methods Development . . . 134
7.1.2 Geometrical and Physical Expansion . . . 134
7.1.3 Implementation of STEM Simulations . . . 136
7.2 Basic Knowledge Obtained from Simulations . . . 136
7.3 Correlation to Experiments. . . . 138
7.4 Future Outlook on Radiolysis modelling . . . 138

APPENDIX A : RADIOLYSIS KINETICS MODEL . . . 140

APPENDIX B : RADIOLYSIS SPUR MODEL . . . 143

BIBLIOGRAPHY . . . 145

CHAPTER 1

INTRODUCTION

1.1. General Introduction

It has not been long since the world of nanoscience was first introduced by Richard Feynman in his famous lecture, *"There is Plenty of Room at the Bottom: An Invitation to Enter a New Field of Physics",* delivered at the annual American Physical Society meeting in 1959.[1] Nanoscience fundamentally turns around the idea that materials at the nanometre scale (10^{-9} m) exhibit distinct properties compared to their bulk.[1, 2, 3, 4] For instance, metals shaped at these dimensions demonstrate unique magneto-optical behaviours, which are vastly different from those observed in bulk metals. These properties have a strong influence in fields including energy storage and conversion catalysis, quantum information, and biomedicine, among others. The development of nanoscience from 1950 to the present has been constantly advancing by the advent and evolution of sophisticated imaging and manipulation techniques, notably electron microscopy and scanning probe microscopies, which have enabled revolutionary observation and control at the nanometre scale. Indeed, surpassing the resolution limits imposed by light wavelengths has been crucial in nanoscience. Techniques such as scanning tunnelling microscopy (STM) and atomic force microscopy (AFM) use quantum mechanical effects and atomic forces to bypass these restrictions. However, the primary focus of this dissertation is on advancements in electron microscopy, which employs electron beams to illuminate and interact with materials at atomic resolutions. [5, 6] Electrons, functioning as both particles and waves with a wavelength as small as 1/20 of an angstrom (10^{-10} m), have overcome the diffraction limit of light imaging microscopes, opening up a new realm of exploration of condensed matter.

For decades, microscopists were content to observe metals, semiconductors, catalysts, and other advanced materials under operational conditions such as heating, biasing, and mechanical loading. Monitoring these materials and the dynamics they undergo, in liquid environments, has long been out of reach because of the high vacuum requirements of electron microscopes. This goal was ultimately achieved thanks to advances in microfabrication

and the development of thin, electron-transparent membranes, introducing the concept of a liquid cell for microscopy.[7] In 2004, Thiberge [8] demonstrated nanometre resolution imaging of fully hydrated cells using a 145 nm thick polyimide film in scanning electron microscopy (SEM). In the same year, silicon nitride (Si_3N_4) membranes [9] were used to encapsulate liquid samples, making transmission electron microscopy (TEM) imaging of liquid specimens possible. This led to the emergence of liquid phase TEM (LP-TEM).

LP-TEM rapidly established as a technique uniquely capable of providing direct *in situ* observation of nanoscale processes occurring in liquids. It holds potential in uncovering fundamental insights into chemical and physical phenomena that were previously accessible only through theoretical physics. These include the formation and dissolution of colloidal inorganic nanocrystals,[10, 11] the assembly of polymers in solution,[12] and electrochemical catalysis at the electrode-liquid interface.[13, 14]

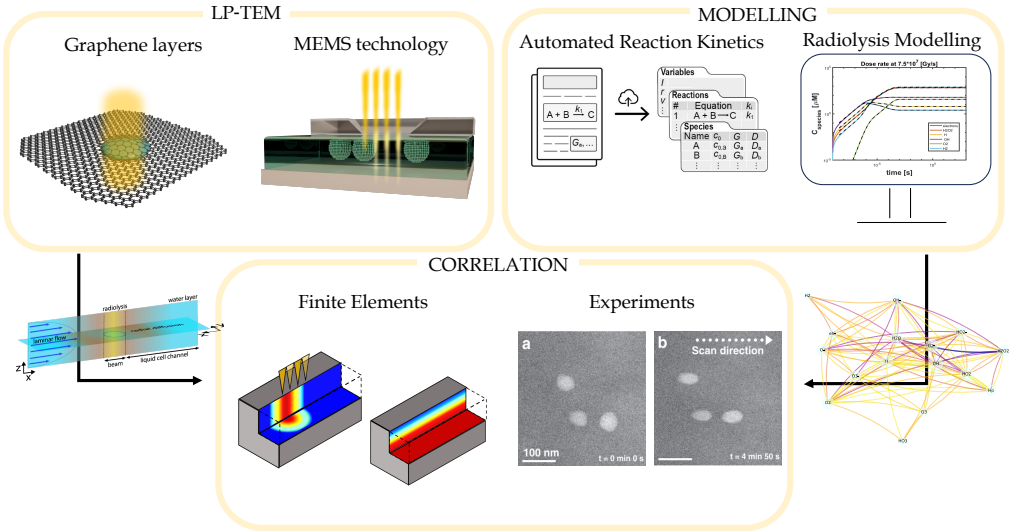

Figure 1.1: The schematic outlines the key areas crucial to advancing LP-TEM into a quantitative technique, focusing on liquid cell (LC) designs and radiolysis simulations. The third box highlights finite elements (FE) as a numerical modelling technique required to achieve a correlation between theory and real scenario of the experiment, e.g. diffusion plus radiolysis (left geometry) and flow (right geometry), and in this case scanning beam inducing elongation of nanoparticles (micrographs adapted from Zecevic et al. Copyright 2017, Advanced Science News).

The technique has harnessed the extraordinary electronic and mechanical properties of graphene as electron transparent membrane to achieve atomic visualisation in high-resolution

liquid phase TEM (Fig. 1.1).[15] From this point forward, the fabrication of novel graphene liquid cells has evolved into a truly cross-disciplinary endeavour,[16, 17] one that not only enhances our ability to visualise individual atoms but also allowed researchers to observe complex structures, such as viruses, as they might behave within the native environment.[18] Another branch of fabrication advanced toward the development of miniaturised devices, specifically liquid cell architectures using MEMS technology (Fig. 1.1). Innovation in this field has been the ability to integrate external stimuli in the liquid cell inside the microscope. In fact, dedicated TEM holders are equipped with channels for liquid flow along with contacts for thermal heating and electrical biasing. These features make it possible to initiate and observe dynamic behaviours beyond the standard Brownian motion of particles in liquid.

However, during LP-TEM experiments, it became evident that the effects induced by electron beams are unavoidable and have a significant impact on the irradiated sample.[19, 20] These effects, resulting from energy exchange of the probe electron with solid membranes, contacts, or liquid, include temperature changes,[21] interactions at the metal-liquid interface,[22] and, most notably, radiolysis.[23] Radiolysis describes the generation of chemical species which can alter the composition of the solvent and eventually trigger unwanted side reactions.[24] For instance, radiolytic effects were observed to influence surface interface reactions,[13] suppress or enhance the nucleation and growth of nanocrystals,[25] and can lead to the formation of observable gas bubbles.[26] As a result, the demand for correlative tools to quantify radiolysis effects has grown (Fig. 1.1) leading to significant advancements in modelling [23] and experiments.[27] While experimental approaches are mostly hampered by the complexity of the experimental setup, modelling approaches could substantially advance by relying on previous knowledge acquired in the context of nuclear reactor research, where radiolysis was also a challenge. Previous theoretical efforts have also led to the implementation of increasingly sophisticated simulation methodologies.[28, 29] At the same time, all simulations currently rely on assumptions derived from low-density electron fluxes, which implies that these assumptions are appropriate for previous interest in nuclear power reactors [30] rather than for the significantly higher electron beam fluxes encountered in

microscopes. This fundamental assumption, which urgently requires verification, has yet to be addressed in a modelling study.

Thus, so far, numerical modelling has handled two primary purposes: 1) to replicate the kinetics of the numerous reactions triggered during radiolysis within both the sample solution (mostly water) and the sample itself, where water alone involves more than 70 reactions [30], and 2) to account for the correct reproduction of the irradiation geometries in TEM (e.g., beam volumes, scanning) and the multiscale liquid cells used and additional stimuli applied.

Although the first task is well-established, with a wealth of literature on reaction rate constants available,[31] (Fig. 1.1), the second task has been less explored. Previous efforts have frequently relied on oversimplified assumptions, primarily concerning radiolysis yields, or incomplete geometrical descriptions of species mass transport in specific LP-TEM setups and irradiation modes. These limitations can substantially affect the accuracy of the observed reaction dynamics. Despite many experiments being conducted under specialised conditions, the models used have mainly relied on basic, unrefined calculations.

1.2. Scope & Objectives.

The main motivation behind this thesis is that the way to convert LP-TEM from a qualitative observation technique, as it is currently, to a quantitative methodology for studying nanoscale dynamics in liquids lies through extensive and realistic simulations of the chemical environment in the liquid nano reactor under rigorous electron beam irradiation.

The premature state-of-the-art in this field, described in the introduction, defines the main aim of this thesis: the development of a simulation framework that advances the existing state-of-the-art. This global aim can be separated into several work objectives:

- Expansion of existing radiochemical reaction 0D and 1D models into realistic 3D geometries that account for actual boundary conditions. (Chapters 3 and 4)
- Implementation of relevant transport mechanisms (diffusion, convection) in realistic 3D model geometries. (Chapters 3 and 4)

- Developing approaches for reducing the computational cost of 3D Multiphysics FE simulations, enabling their use as a versatile tool for a wide range of applications. (Chapters 4)

- Extension of the existing irradiation scenario for a broader range of application cases (e.g. STEM case), implementation of a framework for automation of this task. (Chapters 5)

- Verification of developed models on existing experimental data. (Chapters 5)

- Verification of the basic assumptions of existing models, in particular the low-LET approximation and dose rate independent G-values. Implementation of a simulation framework to generate dose-dependent G-values. (Chapters 6)

Integrating all transport processes into radiolysis models in realistic experimental scenarios (e.g., flow setups, electrodes, and irradiation modes) should establish a benchmark methodology for improving the potential of such simulations. Consequently, investigating these models in relation to additional complexities, such as geometries and symmetries (ranging from diffusion to flow, including STEM geometries or eventually electrochemical currents), by modifying assumptions (initial or final yields) is the merged scope of this work. All the hypotheses and models that will be developed to address the spatial and temporal regimes of radiolysis in LP-TEM are summarised in Fig. 1.2.

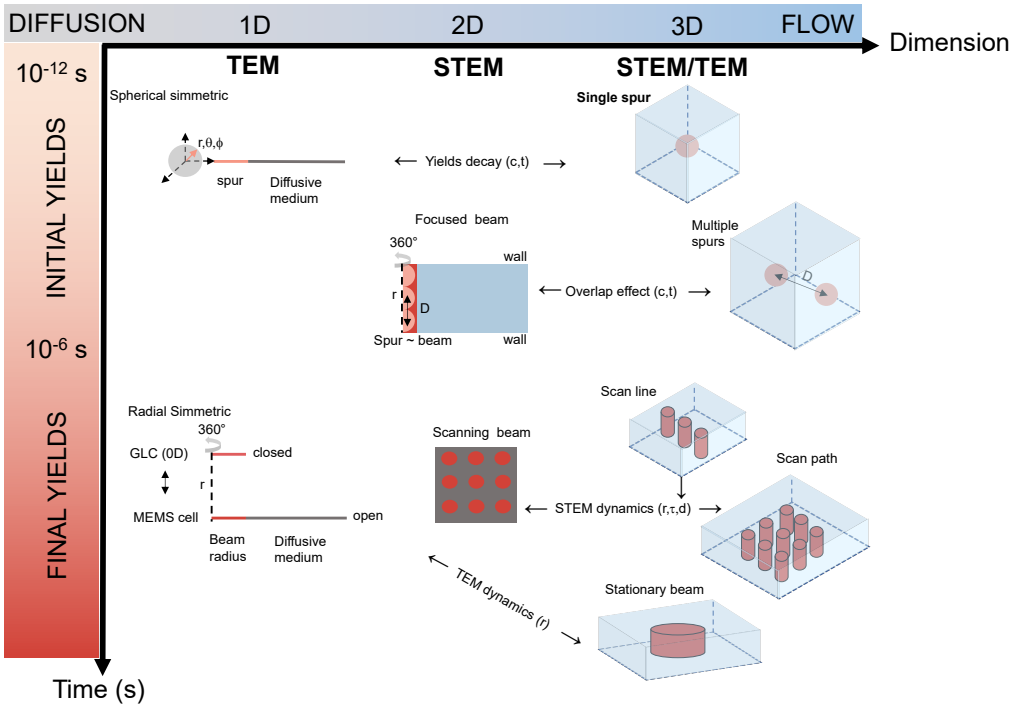

Figure 1.2: The schematic illustrates a spatio-temporal graph, including the models and their geometries/symmetries addressing the various scenarios in LP-TEM. The *horizontal axis* shows the models for diffusion (1D for spurs or TEM and 2D for STEM) with spherical symmetry (spur) or cylindrical symmetry of the beam (TEM). A transition to 2D or 3D geometries is needed when adding flow (or eventually electrochemical drift). The *vertical axis* addresses changes in the yields as input values for radiolysis generation for the timescale in which the reactions and diffusion are evolving.

1.3. Structure of the Thesis.

This fully computational thesis presents a comprehensive approach to theoretical studies of radiolysis, with a specific focus on applications in LP-TEM research. Chapters 2 and 3 provide an overview of the current state-of-the-art in the field and discuss the fundamental theories and methodologies used and developed to advance these radiolysis models. Chapters 4, 5, and 6 present the results of this work. Each chapter of results begins with a summary of the knowledge pertinent to the specific investigations undertaken. Following this, the focus is on the technical aspects that validate the model and consequently the results and predictions, while enhancing the understanding of experimental observations.

Chapter 2 specifically establishes the foundation by providing an overview of electron-sample

interactions, with a focus on radiolysis damage in liquids. Thereafter, the focus shifts to the development of radiolysis theory and its recent adaptation to models, highlighting unresolved questions that need to be addressed with contemporary modelling approaches: replication of experimental scenarios, imaging modes, and quantification of yields.

Chapter 3 establishes the foundational methodology for implementing FE models and provides a comprehensive workflow for radiolysis kinetics and species transport in liquid media, applicable to techniques beyond LP-TEM. These aspects are referenced from the following chapters as needed.

Chapter 4 focusses on this comprehensive solution, hereafter referred to as the framework, developed to model radiolysis under realistic LP-TEM conditions. The first section outlines a strategic optimisation that achieves computational efficiency without compromising solution accuracy in multiphysics models. The chapter explores the possibility of reducing the model dimensions and accelerating the solution process by factors ranging from tens to hundreds. The chapter then provides an in-depth analysis of the impact of reactions, diffusion, and convection on radiation chemistry,[28] advancing the theoretical understanding and supporting LP-TEM experiments under stationary irradiation (TEM).

In Chapter 5, the complex challenge of simulating locally and temporally varying electron flow is addressed, with a focus on STEM. A simulation approach, based on newly developed codes, allowed the discovery of previously unknown features of this imaging technique. The model was validated against documented experimental cases in the literature, semiquantitatively reproducing observed phenomena.

Finally, Chapter 6 revisits the basic assumptions applied in previously reported models to advance radiolysis quantification. For the first time, it reproduces a "spur" model—an event in which radiolysis is initiated—using a deterministic approach rather than the traditional stochastic method, which is challenging to apply to the electron densities of LP-TEM. This model has been validated against existing pulse radiolysis data. The new method enables the estimation of primary species generation at very high electron fluxes, addressing limitations in previous estimates that were more applicable to lower fluxes, typical of macroscopic

configurations.[32]

The thesis concludes with a summary and future outlook for the automated radiolysis simulation workflow in Chapter 7.

1.4. List of Dissemination

A substantial portion of the results presented in this thesis were published in or submitted to peer-reviewed journals.

- Merkens, S.*; **De Salvo, G.***; Chuvilin, A. The effect of flow on radiolysis in liquid phase TEM flow cells. *Nano Express* 2023, *3* , 045006. Equally contributing authors* [1]

- Merkens,S., **De Salvo, G.**; Kruse, J.; Modin, E.; Tollan, C; Grzelczak, M; Chuvilin, A. Quantification of reagent mixing in liquid flow cells for Liquid Phase-TEM. *Ultramicroscopy* 2023, *245* , 113654.

- Yang, Y; Feijóo,J; Briega-Martos, V.; Li, Q; Krumov, M; Merkens, S.; **De Salvo, G.**; Chuvilin, A.; Jin, J; Huang, H.; Pollock, C.J.; Salmeron, M.B.; Wang, C.; Muller, D.A.; Abruña, H.D.; Yang, P. Operando methods: A new era of electrochemistry. *Current Opinion in Electrochemistry* 2023, 101403.

- Merkens, S.; Tollan, C.; **De Salvo, G.**; Bejtka, K.; Fontana, M; Chiodoni, A.; Kruse, J; Aime Iriarte-Alonso, M; Grzelczak, M; Seifert, A.; Chuvilin, A. Toward sub-second solution exchange dynamics in flow reactors for liquid-phase transmission electron microscopy. *Nature Communications* 2024, 15, 2522.

- **De Salvo, G.**; Merkens, S.; Korner, A.; Fritsch, B.; Hutzler, A; Malgaretti, P; Chuvilin, A. A workflow for modeling radiolysis in chemically, physically, and geometrically complex scenarios. *Manuscript under review at iScience.*

[1] This work is also discussed in Stefan Merkens' PhD thesis, *"Orchestrated Mass Transport for Quantitative LP-TEM"*, October 2023, presented as a compendium of articles and in full compliance with the rules of the University of the Basque Country.

Further manuscripts, currently in the drafting process, are mentioned at the beginning of the chapters in which they are discussed.

CHAPTER 2

ELECTRON-SAMPLE INTERACTIONS IN LIQUID PHASE TRANSMISSION ELECTRON MICROSCOPY

This chapter discussed the basic concepts of electron-matter interaction from the perspective of electron microcopy. By integrating both chemical and physical concepts, the discussion builds on the fundamentals of electron-sample interactions and the associated damage, which, in part, has given rise to the field of radiation chemistry. The applications of radiation chemistry within the specific constraints of liquid-phase transmission electron microscopy (LP-TEM) are then explored, and the state of the art in the field is highlighted.

2.1. Electrons as Probes of Atomic Matter

Electron microscopy emerged as an effort to overcome limitations of light microscopy primarily in terms of resolution. Besides a much shorter wavelength of electrons as compared to visible-range photons, electrons have non-zero mass and charge, which lead to a much stronger interaction with the matter. Thus, while visible light microscopy can be considered as 'inert' relative to samples, i.e. not producing notable damage in a majority of cases of waste, in electron microscopy, sample damage, in its broad meaning, is an essential concept directly related to signal-to-noise ratio of the data, noise-determined resolution, imaging artefacts, and, in the end, correct interpretation of observations.

2.1.1. Resolution Considerations and Imaging Principles

Resolution in wave-based imaging methods is determined by the so-called diffraction limit introduced by Abbe [33] in 1873 as (for the case of coherent illumination):

$$d = \frac{\lambda}{2NA} \tag{2.1}$$

where d is the attainable resolution, λ is the wavelength and NA is the numerical aperture of the objective lens defined elsewhere.[34] It should be noted that although Abbe considered light in his work, the derivation of the formula is independent of the nature of the illumination and is general for any lens-based imaging system. The ultimate resolution of the normal

optical microscope operating in the visible light wavelength range is about 200 nm. There are many techniques to achieve super-resolution, e.g., by usage of incoherent illumination, immersion oils, fluorescence etc., but it always comes at some cost, e.g., limited application range or low contrast.

After the invention of Busch of the electromagnetic lens in 1926 [35] and his patent on the electron microscope in 1928 (without actual implementation), Ernst Ruska and Max Knoll made an effort to construct a working prototype of an electron microscope with the idea in mind of overcoming the diffraction limit by using particles for imaging.[6] To their great disappointment, they learnt from the lecture of de Broglie in the summer of 1931 that electrons also have a wavelength defined by their rest mass and velocity.[36] Thus, the resolution of the electron microscope is also diffraction limited. However, the application of de Broglie's formula for fast-moving electrons is as follows:[37]

$$\lambda = \frac{h}{p} \tag{2.2}$$

where λ is the wavelength, h is Planck's constant and p is the momentum of the particle. For fast-moving electrons, the wavelength 3-4 orders of magnitude (e.g., 3.7 pm for 100 kV and 1.97 pm for 300 kV) was smaller than for visible light, which ensured further development of electron microscopy.[38]

In 1940s Albert Rose introduced (in relation to uprising television) the concept of noise limited recognition of the features[39] and has defined the well-accepted 'Rose criterium': the feature can be recognised on the image if the signal-to-noise ratio (SNR) exceeds 5. The application of this criterium to electron microscopy [40] leads to a concept of dose-limited resolution, which is crucial for many application areas. Thus, if D is an electron dose (in e^-/nm^2), C is a contrast of the feature to be recognized ($(I_{\text{feature}} - I_{\text{background}})/I_{\text{background}}$), then in an ideal imaging system with an infinitely small instrumental resolution the resolution will be defined by:

$$d_{\text{SNR}} = \frac{5/C}{D^{1/2}} \tag{2.3}$$

In a more general case of a real imaging system the resolution can be written as:

$$d = \sqrt{d^2_{\text{instrumental}} + d^2_{\text{SNR}}} \tag{2.4}$$

As we have discussed above, in light microscopes, generally there is no influence of the illumination light on the sample, and thus infinite dose can be acquired, making SNR-defined resolution obsolete. This is very different in electron microscopy, where strong electron-matter interactions may lead to unrecoverable changes in the sample, and thus an affordable critical dose should always be accounted for whenever resolution is discussed.

2.1.2. Electrons-Sample Interactions

Electrons interactions with matter with respect to electron microscopy are generally classified as elastic and inelastic electron scattering.[34]

Elastic scattering involves the interaction of an electron with the electrostatic potential of an atom or a magnetic field, resulting in a change in the electron's momentum but without any energy exchange. In simpler terms, the electron's propagation direction changes, but its speed remains constant. This process can be effectively described using both a particle and a wave model. The particle model depicts the electron as a charged particle deflected by the Coulomb forces of the atomic nuclei and the electron clouds surrounding them. The wave model, on the other hand, views the electron as a wave whose propagation is influenced by the varying electromagnetic fields within the material. In this wave analogy, the electrostatic potential and magnetic flux act as refractive indices, bending the electron wavefront as it passes through the sample. Important features of elastically scattered electrons are relatively small scattering angles (below 10 deg) and preservation of coherence. Elastically scattered electrons are those used for high-resolution phase contrast imaging in TEM mode.[41]

Inelastic scattering assumes energy loss by the incident electron (in very special cases – energy gain), which happens via two primary mechanisms: radiation (Bremsstrahlung and Cherenkov radiation) and energy transfer to the sample. The latter is especially valuable in respect to electron microscopy as it is related to the excitation of specific processes (and thus to characteristic energy losses) in the matter, and thus can be utilised in different kinds of

spectroscopy: X-ray spectroscopy (EDX, WDX), electron energy loss (or gain) spectroscopy (EEL (G) S), and cathodoluminescence (CL).

The interaction of incident electrons with the nucleus is characterised by low energy transfer (10 to 100 meV for phonon excitations, up to a few eV for atom displacement) and high scattering angles up to 180 deg. The study of phonon losses has become popular in the last decade after the commercialisation of ultra-high resolution EELS spectrometers,[42] while atom displacement by focused electron beams is widely used for nanopatterning of 2D materials.[43]

There is a set of terms related to scattering events that will be referenced throughout the chapter. The probability that an electron is scattered in a particular way is described in terms of a cross section σ, or a mean free path λ_{MFP}. The cross section represents the effective area through which two particles must pass, relative to their motion, in order for them to interact and scatter. If there are N particles per unit volume in the sample, and the cross section σ for a particular scattering event is known, then the probability of a single electron being scattered as it passes through the thickness dx of the sample is given by $N\sigma dx$. Alternatively, to express the same concept, the mean free path for the scattering is:

$$\lambda_{MFP} = \frac{1}{N\sigma} \tag{2.5}$$

λ_{MFP} has the dimension of length and represents the average distance an electron will travel before being scattered in a specific manner.

2.1.3. Radiation Damage In Electron Microscopy

The signals generated by inelastic interactions of incident electrons are useful for analysis but come at a cost: sample damage by an electron beam, often called radiation damage.[44] This damage, which affects both the structure and the chemistry of the sample, is linked to the energy of the incident electron beam and varies depending on the material. If the structure or chemistry are changed, the sample no longer represents an initial state. As discussed in Section 2.1.1, the resolution in electron microscopy is dose-dependent and radiation damage effectively limits the dose accessible for imaging. This is a principal limitation

of the technique in addition to the diffraction limit.

Three principal damage mechanisms can be distinguished: knock-on damage, heating, and radiolysis.

Knock-on damage is a process of atom displacement/removal from its position in a solid or in a molecule as a result of a direct collision of an electron with a nucleus. This process has an energy threshold for atoms of different mass and bonding energy, i.e. the process takes place only if the energy of the primary electrons exceeds a particular value. The most known threshold values are 140 keV for graphite [45] and 80 keV for the graphene monolayer.[46] The rate of the process increases rapidly with the primary beam energy after the threshold, but then stabilises at relatively high energy values.[44] The process does not depend on the phase of matter (liquid or solid), as well as its electrical or heat conductivity. However, it has a weak dependence on the temperature.

Heat is generated in the samples as a manifestation of phonons excitation. For good heat conductors, such as metals, diamond, or graphene, locally generated heat is efficiently dissipated, and the local temperature rise typically does not exceed 1 K.[44] On the other hand, for polymers and other organic materials with poor heat conductivity, heating can be substantial, which complicates electron microscopy studies of those.[47] Freezing the samples to cryogenic temperatures and using low dose rate imaging is a common way to overcome this issue.

The most significant damage mechanism for the topic of this thesis is radiolysis – a process arising from electron-electron collisions and excitation of an electron from atomic orbital either to continuum or to one of excited states. This excitation leads to bond breakage and displacement of the potential atom. However, in good electrical conductors (metals, semiconductors) such electron vacancies are filled (and thus the bond recovers) much faster than the atom moves from its place, and thus radiolysis in conducting samples does not play a role. On the other hand, in polymers, biological materials, ceramics, ionic salts, and minerals, electron excitations lead to unrecoverable chemical and/or structural changes. For these classes of materials, radiolysis is the main damage mechanism that leads to amorphiza-

tion, cross-linking, and even carbonisation. The consequences of radiolysis can be reduced to some extent at cryogenic temperatures, as this suppresses the mobility of the atoms but cannot be eliminated completely. The rate of radiolysis is surprisingly inversely proportional to the beam energy, so utilisation of higher accelerating voltages is a common method to reduce this kind of damage. It should be noted here that electron excitations happen equally in solids and liquids, but in liquid phase atoms/molecules mobility is much higher than in solids, and highly reactive species generated by electron excitations - ions and radicals - have freedom to move and initiate secondary reactions. However, liquids do not possess 'structure, and thus radiolysis in liquids can be considered mainly as a chemical phenomenon. Radiolysis in liquid, mostly in water, is the key topic of this thesis and will be described in detail in the following sections.

2.2. Radiolysis of Water

This is the main section of this theoretical chapter. In the following subsections, the theory of radiolysis, developed in various research fields and adapted to LP-TEM, is reviewed to provide the background for understanding the results presented in this thesis. Throughout the text, the focus will remain on water-based systems, as water is the fundamental solvent used in liquid sample imaging.

2.2.1. Historical Remark

The first efforts to observe the effects of ionising radiation on matter date back to the early 1900s, shortly after Wilhelm Röntgen's discovery of X-rays.[48] Most of the relevant studies addressed radiation sources from X-rays (greater than 100 eV), the decay of radioactive nuclei, and beams of accelerated charged particles (e.g. electrons, protons, and heavy ions). Over time, targeted experiments on ionising radiation led to simplified reaction schemes for radiolysis.[49, 50] These schemes have been continuously expanded by newly discovered chemical species, such as the hydrated electron in 1962 by Hart and Boag's experiments.[51] The challenge of directly quantifying the concentrations of radiolytic species gave rise to an independent research field in 1942, when Milton Burton inaugurated a new branch of study of Radiation Chemistry at the University of Chicago. Driven by the demands of nuclear research, the primary commitment at the time was to understand the decomposition of water

used as a coolant in nuclear power plants. On the theoretical front, significant progress was made in understanding the primary phenomena that contribute to the generation of radicals and molecules by the ionisation of water. The yields of these products and their reaction pathways were identified either experimentally or calculated through theoretical models. A general scheme was proposed and has been continuously refined over the years,[52] still serving as the foundation for studying radiolysis today.

2.2.2. Radiolysis of Water - Basics

Radiolysis consists of a series of phenomena by which molecules are destabilised by ionising irradiation, involving physical, chemical, and a combination of both processes. Figure 2.1 shows a scheme for the radiolysis of pure water, integrating insights from a century of studies in radiation chemistry. This scheme covers various time regimes, mostly dependent on the chemical or physical description of the processes involved.[52] In the initial time frame, ending at $t \leqslant 10^{-15}$ s, molecules can be considered static, with energy deposition compensated through their fast relaxation. In the subsequent phase, ending at 1 picosecond, a slight molecular motion is possible, allowing interactions among nearest neighbours. By the third time scale, diffusion becomes active, and reactions on a larger time scale commence. The interactions and processes that occur are detailed below.

- In the *physical* regime ($t \leqslant 10^{-15}$ s), the electron traverses the aqueous medium and deposits the energy primarily through inelastic interactions between electrons and electrons with solvent molecules (t=0). This process triggers the ionisation and excitation of the water molecule (see Figure 2.1). Ionisation leads to the secondary generation of low-energy electrons, each following a brief, independent trajectory.

- In the *physico-chemical* regime (spanning from 10^{-15} to 10^{-12} s), the medium rapidly equilibrates to changes resulting from the production of electrons and excited and ionised water molecules (thermalisation). This involves processes such as ion-molecule reactions, dissociative relaxation, autoionisation of excited states, and hydration of electrons. This results in the creation of nine primary species, namely $e_h{}^-$, H_3O^+, $O(^1D)$,$H^\bullet$, $HO^\bullet$, $HO_2{}^\bullet$, H_2, H_2O_2 and OH^-.

- In the *chemical* regime, transport phenomena become increasingly important. As the primary species at the end of the physico-chemical regime barely moved away from their localised region of generation, diffusion begins to counteract the emerging concentration gradients starting at 1 picosecond. Meanwhile, chemical reactions are ongoing, with radical recombination playing a significant role in the formation of more stable products [53]. Around $t \sim 1\,\mu$s, radical recombination ceases to mark the end of a heterogeneous chemical phase but the beginning of a homogeneous chemical phase. This chemical development can be calculated from radiolysis yields, with the conventional metric for assessing the impact of ionising radiation being the number of species produced per 100 eV of absorbed energy. This metric is known in radiation chemistry as generation values. A.O. Allen was a pioneer of the concept of generation values [49]. There is a convention that small letter g refers to the initial g^0 yield measured on the picosecond scale, while the capital G describes the microsecond yields, that is, the G values.

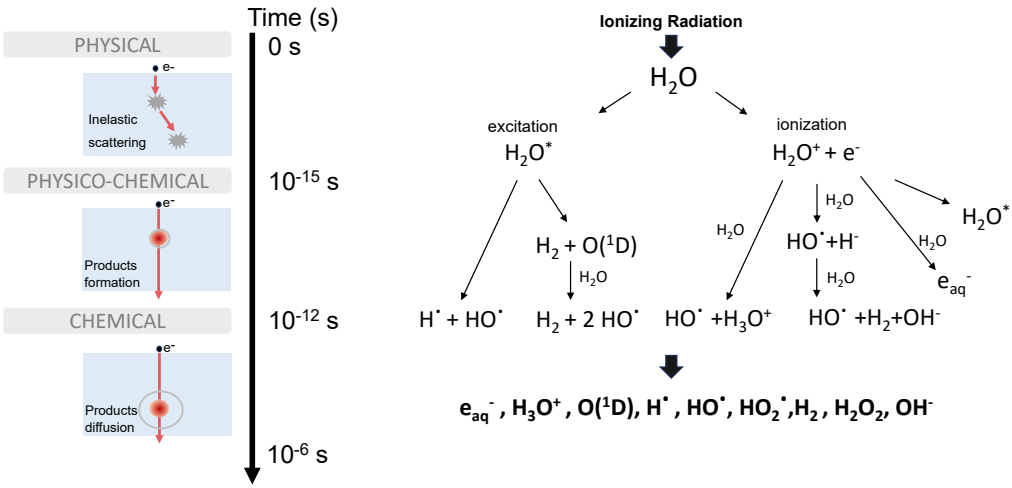

Figure 2.1: The schematic illustrates the temporal progression of water radiolysis. On the left side, it outlines the time regimes and the scenario for a single electron hitting water. The right side shows the evolution of ionising radiation chemistry, starting from dissociation and continuing until the species react and diffuse, beginning approximately from 1 ps onwards.

2.2.3. From Heterogeneous to Homogeneous Models

Once the reaction scheme became more clear, researchers began to develop increasingly sophisticated models to define a diffusion theory applicable to radiolysis. The first math-

ematical approaches were quasi-homogeneous and suggested that radiation yields depend on the "background" variation of ionisation density, a particle track experiencing the influence of others, as first proposed by Magee (1951).[54] This work was expanded by the same group,[55] who introduced the first realistic heterogeneous geometry in a model, initially with equally separated tiny volumes ($\approx$ nm) known as *spurs*, and later incorporating random generation along the primary track.[56] These spurs arise from either primary or secondary collisions, with secondary collisions deviating from the primary track. Together, these insights established the theory of geometrical effects caused by the scattering path of a particle, known as the track structure (Fig. 2.2a). This theory evolved through more precise studies that provided detailed information on the shapes and frequency of occurrence of these volumes, including reference values for electrons in water, values of particular interest for the field of electron microscopy.

The Electron Track in Water. The nature of the electron track was elucidated by Mozumder through the classification of energy loss processes [57, 58]. Mozumder built on the "random" model previously introduced,[56] allowing a deeper look at the stochastic characteristics of the structure of the track. This classification used an energy-loss partition algorithm based on calculated cross sections.[59]

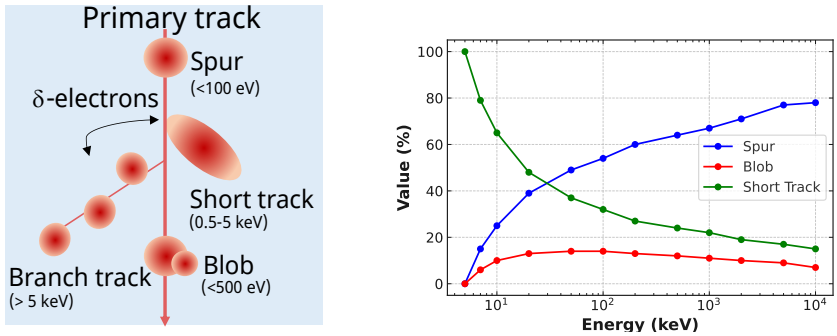

Figure 2.2: Schematics of **a)** heterogenous electron track structure and associated energy loss processes in water radiolysis, **b)** The distribution of energy among spurs, blobs, and short tracks by an electron in water, within the irradiation energy range of 5 keV to 10 MeV, as documented in Table I from Mozumder, 1966.[57]

In essence, along the trajectory of a primary particle, are identified spurs, which are primary collisions (with the energy transferred up to 100 eV) in which any secondary electron has the capability to further ionise water (see Fig. 2.2a). Spurs have the diameter of 1.2-10 nm [60] and are separated by an inelastic mean free path, which is about hundreds of nm,[61] thus these volumes can be considered independent of each other on the 3^{rd} chemical stage. Secondary electrons escaping from the vicinity of the primary track form *blobs* (100-500 eV) and *short tracks* (500-5000 eV); however, within these volumes, the inelastic events are sufficiently close such that they cannot be considered isolated from the primary track. A secondary electron ejected with an energy exceeding 5 keV travels along a branched track, distanced from the primary track of the particle.

In Figure 2.2b the frequency of these events that come from electrons at different energies is summarised. At low primary energies ($\leq$ 30 eV), most of the track resembles a single short track. In contrast, at higher energies, spur contributions become more dominant for two main reasons: first, due to relativistic effects; and second, the branch tracks that are generated lead to the creation of additional spurs (Fig. 2.2a). Blob generation reaches a moderate peak between the two regimes, approximately at 100 keV. However, as a first approximation, a linear track structure of primary events could be considered valid and applicable at high relativistic energies, with $\geq 60 - 80\%$ of the energy deposited as spurs

at 300 keV (Fig. 2.2b). This is one of the primary approximations used in homogeneous models, later applied for LP-TEM, which assumes a continuous energy loss of the particle in the medium. The nature of both the particle and the medium can result in different regimes of linear energy transfer (LET).

Low and High LET Regimes. The mean energy loss of an electron as it passes through a liquid can be approximated using the continuous slowing down approximation (CSDA).[59] This approximation often used to describe radiation damage helps simplify the heterogeneous scenario outlined in the previous paragraph.

The energy loss per unit distance reflects the electron's deceleration as its kinetic energy decreases linearly and is often normalised to the mass density of the material. This leads to the concept of *stopping power*,[24] and is crucial for quantifying the total absorbed dose in materials. This approximation reduces the complexity of the incident particle track into two types: (1) low LET radiation, characterised by the formation of isolated spherical spurs, representing discrete energy deposition, and (2) high LET radiation, where the tracks appear as continuously overlapping spurs, indicating denser energy deposition, as shown in Fig. 2.3a.

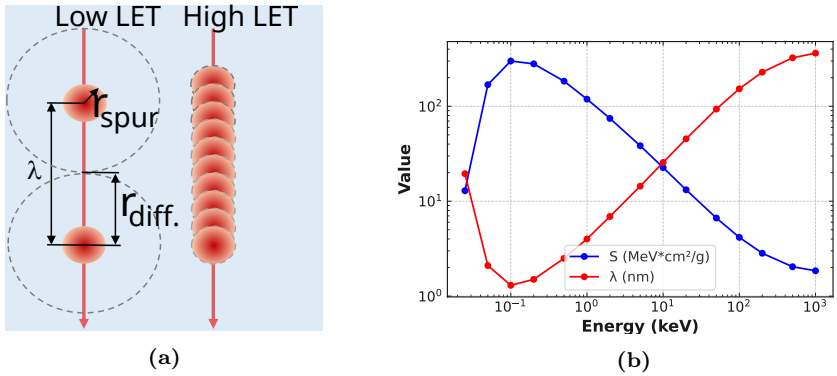

(a) (b)

Figure 2.3: Schematics of **a)** Low and high LET regime representative tracks and characteristic quantities of mean inelastic free path (λ), spur radius (r_{spur}) and minimum radius of diffusion before overlap (r_{diff}). **b)** Stopping power and inelastic mean free path of electrons in water, in the irradiation energy range of 25 eV to 1 MeV, data extracted from LaVerne table I (1995).[61]

Albeit it may seem that considering these regimes oversimplifies the track, stopping power accounts for long-range secondary events, meaning that only the geometry of the track is

streamlined, not the energy. At lower energies (below 1 MeV), the frequent occurrence of close collisions over a limited trajectory significantly affects both the stopping power and the mean free path, which exhibit an inverse relationship, as shown in Fig. 2.3b. These parameters tend to remain constant when relativistic effects predominate (above 1 MeV for electrons).

Changes in Yields of Radiolysis. So far, the discussion has focused on the single-electron irradiation scenario, which can be described using a complete (electron track) or partial (low and high LET) geometrical model of energy deposition. However, the key factor influencing the transition from heterogeneous to homogeneous irradiation (i.e., the chemical regime) is the density of the irradiation, the combined effect of many electrons, which ultimately determines an accurate estimate of the final G values for irradiation greater than a microsecond.

In the context of low electron flux densities, such as that encountered in nuclear and biological radiation damage, the main distinction between the two regimes depends largely on the nature of the particle and the material it traverses. In these fields, electrons, being 'light' particles, do not cause extensive damage and thus fall into the low-LET regime. The corresponding yields can be calculated by assuming single, non-interacting electrons (Fig. 2.4a).

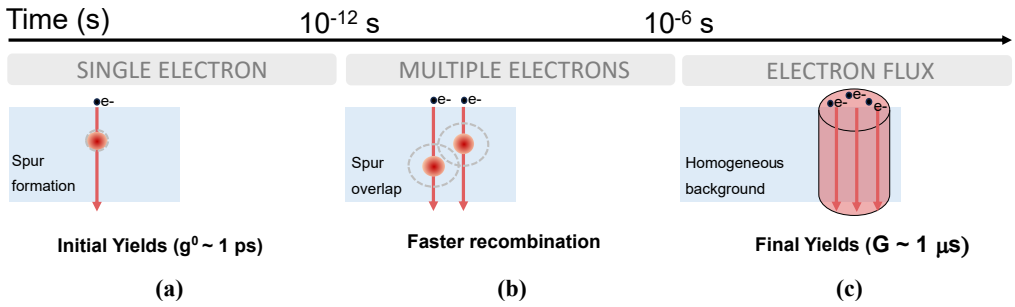

Figure 2.4: The timeline of the chemical regime highlights two yield regimes: at low fluxes, electrons do not interact, whereas at higher fluxes, spur overlap occurs, leading to interactions between electrons and changes in chemical generation or G value.

On the other hand, in electron microscopy and other radiation probe techniques (e.g., X-ray) that involve high-flux irradiation, this rule may not apply. The highly reactive species

produced along the tracks interact more frequently because the primary tracks are very close and the spurs eventually overlap (Fig. 2.4b), leading to rapid recombination and increased formation of other by-products under homogeneous irradiation conditions (Fig. 2.4c). This phenomenon has long been hypothesised and observed experimentally,[53, 62] but has only been reproduced to a limited extent in models for the estimation of final G values (discussed in 2.2.4).

Primary Reactions. The reaction set used to describe the chemical regime (Fig. 2.4) is limited to tens of reactions involving primary radiolysis products, which are generated at 1 ps in highly concentrated spurs, as previously illustrated (see Fig. 2.1). The primary products of water radiolysis include e_h^-, $H^\bullet$, $OH^\bullet$, $HO_2^\bullet$, OH^-, H^+, H_2, and H_2O_2. Among these, the radical $OH^\bullet$ is highly reactive as an oxidising agent, while the e_{aq}^- and the H atom act as reducing agents. All of these species are notable for having the highest initial yields (g^0). When these species react in close proximity (refer to the scenario in Fig. 2.4b and c), the main recombination products are predominantly H_2 and H_2O_2, and their yields change consistently over time.

This overproduction will be analysed in Chapter 6 using spur models and a detailed reaction set for the chemical regime of pure water (see the Appendix B.3). For systems beyond pure water, additional reactions should be included to account for changes in yields. The e_{aq}^- species, for instance, participates in electron attachment reactions with various solutes.[31] The H atom can also abstract hydrogen, particularly from saturated organic molecules, to form H_2. Moreover, in aerated water, the high reactivity of O_2 as a scavenger for both e_h^- and H atoms drastically decreases their yields (scavenger reactions in B.3).

2.2.4. Radiolysis Yields Estimation Models

The calculations of the radiolysis yields have evolved significantly since the 1980s. These models use the initial yields (g^0) of the primary products and a reaction-diffusion approach to determine the final yields (G). Initial yields can be obtained from experiments or estimated by simulating the particle track structures, calculated from optical cross sections, which allows for *ab-initio* calculation of the corresponding physical and physicochemical stages in radiolysis (see scheme 2.1).

At the time, pulse radiolysis experiments allowed the direct observation of short time ($\sim 1\,\mu$s) dependence of species. However, this technique has several limitations and measurements have been mostly restricted to hydrated electrons and $OH^{\bullet}$ radicals.[63, 64] Consequently, significant effort has been devoted to fitting the experimental decay profiles of detectable species to simulated yields in particular for primary species that are not directly detectable.

Deterministic Approach. After the pioneering mathematical treatments of reactions and diffusion by the Magee group,[54, 55, 56, 57] a deterministic approach emerged some years later. In this approach, usually a single spur is described by an average initial distribution, and its kinetics is modelled using a system of differential equations.[65, 66] Initially, the species were restricted to a Gaussian distribution, known as the 'prescribed diffusion' implementation.[67] However, other implementations have since removed this restriction, allowing alternative distributions, such as a central minimum in the centre of the spur, which aims to reflect immediate ($t \leq 10^{12}$) reactions at high radical densities without the time for diffusion.[68, 62] Table 2.1 below presents the initial and final values for a single spur, taken from a comparison study using the FACSIMILE code:[69, 70]

Ref.	g^0 (mol/100 eV)	G (mol/100 eV)	Energy Loss (eV)
Trumbore[62]	6.0 ($OH^{\bullet}$)-4.7 ($e_h{}^-$)	3.8 ($OH^{\bullet}$)-2.95 ($e_h{}^-$)	60
Schwarz[67]	5.7 ($OH^{\bullet}$)-4.78 ($e_h{}^-$)	3 ($OH^{\bullet}$)-2.8 ($e_h{}^-$)	62.5

Table 2.1: Initial (1 ps) and final (1 μs) yields with deterministic diffusion-kinetic models.

These values were also reproduced using the same modelling approach and are discussed in Chapter 6.

Stochastic Approach. The stochastic approach to spur dynamics generates the coordinates of primary products at 1 ps (initial yields g^0) from particles track structures (i.e. *ab-initio*), which are further elaborated in the chemical (diffusive) regime using a simulation method called independent reaction time (IRT),[71, 72] leading to the estimation of final G values at 1 μs (Tab. 2.2).

Ref.	g^0 (mol/100 eV)	G (mol/100 eV)	Energy (keV)
Hill & Smith[32]	6.1 ($OH^\bullet$)-4.9 ($e_h{}^-$)	3.38 ($OH^\bullet$)-3.21 ($e_h{}^-$)	1000

Table 2.2: Initial and final yields with Stochastic models. Note that the initial energy is the one of the electron not the loss by an event.

Calculations like those of Hill & Smith,[32] represents the G values used in current modelling for LP-TEM, as will be discussed in Section 2.3.

Comparison of Deterministic and Stochastic Models. A deterministic diffusion model exhibits certain limitations. It struggles to accurately replicate the experimental results at low pulsed energies, where blobs and short tracks dominate (see Fig. 2.2b).[73] Consequently, it may not be the most suitable tool for *ab-initio* radiation studies, i.e. stochastic, as a discrete chemical species description is often more advantageous in capturing random variations in distances, unlike the spur approximation provided by the deterministic model.[71, 74]

Nevertheless, deterministic approaches can be adjusted to fit yield estimations when linear energy transfer (LET) is assumed, with the spur as the sole event generating species (see Fig. 2.3a). Applications of these models have successfully described overlap yields by estimating "interspur" reactions. However, these studies were typically correlated with pulse radiolysis experiments, and not in the context of denser TEM irradiations. The first successful attempt at such modelling is presented in Chapter 6.

This overlap scenario could be difficult for a stochastic implementation, which requires a lot of computation cost to simulate multiple electron tracks. However, this research initiated precise investigations into the correlation between particle tracks and the evolution of the respective yields.[75, 32] For example, works by Pimblott and LaVerne highlighted the importance of spatial details in the calculation of single electron tracks in liquid water.[60] They found that the average energy loss for both integral (spurs only) and differential (short tracks, blobs, branched tracks) tracks converges to the same values, approximately 34 and 38 eV/event, at energies greater than 100 kV. Additionally, for this energy range, spurs account for about 80% of events, with short tracks and blobs each contributing around 10%.

These quantities serve as a benchmark for accessing assumptions in liquid electron microscopy, confirming that the spur fraction initially discussed by Mozumder (60%, see Fig. 2.2b) is further supported by more accurate models from Pimblott and La Verne, increasing the estimate to 80%.

2.2.5. Homogeneous Kinetic Modelling

When the irradiation times exceed 1 μs, in contrast to spur models, such a scenario can be represented in a homogeneous model. This geometric simplification is accompanied by an increase in chemical complexity, and the radiolytic species continue to react, the initially limited set of primary reactions expands, also generating other *secondary* species. The complex interplay of all species as they interconvert and react within a network becomes difficult to track without the aid of homogeneous kinetic models.

The Extensive Reaction Set of Water. The construction of a reaction set posed significant challenges and led to the development of numerous numerical studies to understand radiolysis in large-scale applications, such as industrial nuclear power reactors.[30, 76] The reaction rate constants were experimentally measured using pulse radiolysis,[77, 78] flash photolysis,[79] and time correlation methods,[80] thus establishing a consistent database for these models.[31]

These numerical studies consist of a set of ordinary differential equations (ODEs) describing the temporal evolution of species concentrations c_i for all radiolytic species i involved, as shown in Eq. 2.6:

$$\frac{dc_i}{dt} = -\sum_j k_{ij} c_i c_j + \sum_{j,k \neq i} k_{jk} c_j c_k + R_i \tag{2.6}$$

The right-hand side of the equation includes terms that account for the generation and consumption of species through chemical reactions, with the respective rate constants k_{ij} and k_{jk}. The term R_i represents the rate of radiolytic volume generation and should be applied with final yields under homogeneous assumptions (G_i), depending on the case of irradiation (e.g., radiation, medium, particles flux density).

Elliot [30] developed an extensive set of water radiolysis reactions and includes 75 reactions, among 15 species in addition to water (see the Appendix A.1). Of these, only 8 species

are designated as primary radiolytic products, as already discussed within the primary network for the chemical regime of radiolysis (e_h^-, $H^\bullet$, $OH^\bullet$, $HO_2^\bullet$, OH^-, H^+, H_2, and H_2O_2). Meanwhile, O_2, O_2^-, HO_2^-, O^-, $HO_3^\bullet$, O_3, and O_3^- are generated later and are considered secondary products. Radicals and ions deplete rapidly, resulting in very short lifetimes. In contrast, more stable molecular species can persist in the medium and react at later stages. Some of these stable species, such as O_2 with e_h^- or H_2O_2 with $H^\bullet$, exhibit a high probability of reacting and are therefore recognised as *scavengers*. Their role will be further emphasised in the analysis of species mass transport properties in Chapter 4.

The complexity of this network is visualised in Fig. 2.5 using graph theory tools integrated into the NetworkX library in Python.[81] In this representation, each reactant is depicted as a node, and each connection represents a chemical reaction within the set.

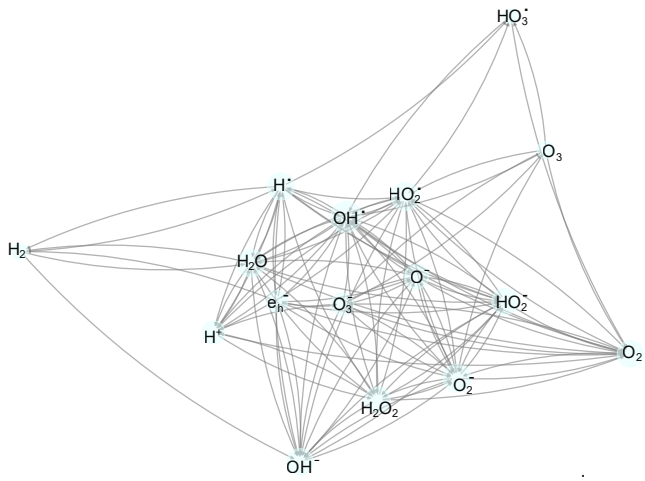

Figure 2.5: NetworkX representation of the water set for radiolysis. Node size is based on degree, indicating the number of edges (connections) adjacent to each node, thereby highlighting the connectivity and importance of each species in the network. The arrows indicate direction from reactants to products, with node positions determined using the Fruchterman-Reingold force-directed algorithm. This algorithm simulates a force-directed layout, where edges act as springs pulling nodes together, while nodes themselves repel each other. The 'force' or weight of each edge is based on k constants in Appendix A.2. For simplicity, the edge weights in this graph do not account for the reaction order or radiolysis generation terms. although the layout qualitatively aligns well with similar representations that include these features.[29]

Within this complex network, kinetic modelling using Eq. 2.6 enables tracking of reaction progression to understand how the chemistry of the solution depends on the intensity of

irradiation. This intensity is reflected in the volumetric generation rate R_i, which must be tailored to the specific experimental conditions.

2.3. Radiolysis Modelling in the context of LP-TEM

To address the need to understand the chemistry of the irradiated solution in the context of LP-TEM imaging, the development and application of models to track the concentration of radiolysis species has become a specialised subfield. This effort was initiated by Schneider et al.[23] who adapted the reaction set discussed above (refer to 2.2.5) to model the radiolytic decomposition of pristine water under continuous TEM irradiation. The model solutions were obtained by solving a system of ODEs, as shown in Equation 2.6, with the volumetric rate of beam generation R_i estimated from theoretical considerations,[82] as below:

$$R_i = \frac{\rho \psi G_i}{F} \quad (M/s) \tag{2.7}$$

In this formulation, ρ represents the mass density of the medium (g/cm^3), and F denotes the Faraday constant in Coulombs per mole (C/mol). The yields (G_i) were taken from a stochastic model,[32] that was carried out under the assumption of low LET. These values assume a time starting at 1 μs and dose-independent generation at earlier times, that is, within the chemical regime (discussed in Section 2.2.3). Here, ψ introduces the absorbed energy dose by the medium, measured in SI units of SI ($\frac{J}{kg \cdot s}$), and its relationship to experimental TEM parameters—such as the electron flux ϕ, given in $\frac{e^-}{m^2 \cdot s}$—is regulated from the density normalised stopping power, as shown in the following equation:

$$\psi = S\,\phi \quad (\mathrm{J\,/\,kg\cdot s}) \tag{2.8}$$

Note that this equation is valid for single scattering scenarios, and expansion terms would be required to account for multiple scattering events. In LP-TEM scenarios the single scattering assumption is reasonable given that the thicknesses of the liquid layer are typically comparable to the inelastic mean free path (λ_{IMFP} = 230 nm at 300 keV; see Fig. 2.3b). In the following discussions, the reference dose rate will be expressed in customary radiation units of Gray per second (Gy/s), equivalent to the SI units in Eq. 2.8.

Uniform Beam Irradiation (0D case). Using the model implementation provided by Schneider[2] to solve the ODEs in Eq. 2.6 with R_i from Eq. 2.7 enabled the calculation of concentrations for all species c_i involved in the radiolytic reactions for pure water, as listed in Appendix A.2. The concentrations of most relevant species is presented in Fig. 2.6a. Under continuous and uniform beam irradiation, an equilibrium concentration (c_{ss}) is reached within milliseconds (t_{ss}), as shown in Figure 2.6a. Solving the model for increasing dose rates within the relevant range for LP-TEM reveals an a proportionality of c_{ss} with respect to dose rate (Fig. 2.6b). Both the dependencies of c_{ss} and t_{ss} on the dose rate follow power laws. In general, doubling the dose rate results in less than a twofold increase in c_{ss}, and the time required to reach steady state scales inversely with the dose rate to approximately the power $-1/2$.[23]

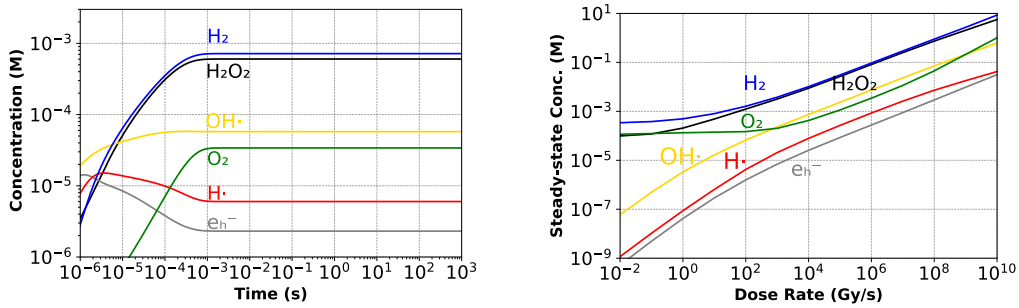

Figure 2.6: Uniform Irradiation Modelling of Radiolysis (0D). **a)** Ordinary Differential Equations solver (ODE) gives the products concentration over the change in time calculated by 73 reactions rate within a network; steady state conc. is reached at milliseconds for an absorbed dose rate associated to 300 keV beam of 1 μm and 1 nA current ,$7.5 \times 10^7 Gy/s$ (data reproduced from MATLAB code of Schneider)[23] **b)** Species from fig. a) are depicted as function of dose rate. Magnitude of steady state conc.(from nM to M) directly depend on the dose rate increase with a almost linear relationship expressed in power laws.

These power laws can hence be used to estimate steady concentrations based solely on the experimental dose rate. However, their applicability is limited to cases where the beam volume is larger than the irradiated liquid volume, thereby preventing species diffusion. For cases where diffusion occurs, the actual geometry of the liquid cell is required.

[2]https://github.com/NMSchneider/Radiolysis

Non-uniform Beam Irradiation (1D case). Understanding radiolysis within a larger reservoir, where the beam irradiates a small portion of the liquid, requires integrating these diffusion terms to accurately model the spatial and temporal evolution of reactive species and their interactions. If the coupled Equation 2.6 is expanded by the description of diffusion, it becomes:

$$\frac{\partial c_i}{\partial t} = D_i \nabla^2 c_i - \sum_j k_{ij} c_i c_j + \sum_{j,k \neq i} k_{jk} c_j c_k + \frac{\rho \psi G_i}{F} \tag{2.9}$$

In the equation second Fick's law accounts for concentration change over time due to diffusion of species i, which depends on the diffusion coefficient D_i and $\nabla^2 C_i$ is the Laplacian of the concentration, representing the second spatial derivative of concentration.

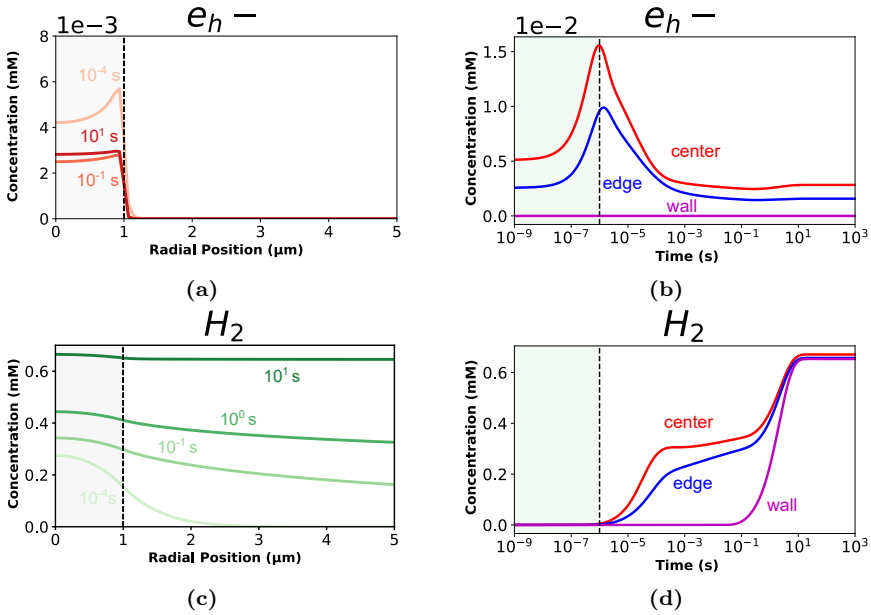

Figure 2.7: Non-uniform Irradiation Modelling of Radiolysis (1D radial). **a-d)** The spatial and temporal profiles depict the concentrations as functions of the radial position at various time **(a,c)** and viceversa **(b,d)** for highly and less reactive species, e.g. ionic as e_h^- and molecular H_2, respectively. Data are reproduced using COMSOL based on the work of Schneider,[23] with an irradiated beam area of radius 1 μm (indicated by the *grey area*) and a total model length of 50 μm. The initial calculation time was anticipated at 10^{-9} s, and time-stepping was refined up to 10^{-6} s (indicated by the *green area*). This strategy allows for a precise determination of the initial non-zero concentration of e_h^-, as shown in Fig. b at 1 μs.

Schneider and co-workers introduced a reaction-diffusion model to solve Eq. 2.9 and to predict the spatial and temporal concentration profiles of species within a circularly symmetric

1D geometry, capturing *in-plane* diffusion gradients. This model incorporates a cylindrical beam geometry, where the radiolysis generation rate of the primary species ($R_i = \frac{\rho\psi G_i}{F}$) is confined to a typical TEM beam radius of $1\,\mu m$ (grey areas in Figs. 2.7a and 2.7c). Only reaction and diffusion terms (1^{st}, 2^{nd}, and 3^{rd} terms on the right-hand side of Eq. 2.9) are applied throughout the cell width ($W = 50\,\mu m$).

Due to diffusion, the reaction kinetics of the system change, influencing species concentrations (compare the 0D data in Fig. 2.6a with the 1D *centre* curves in Figs. 2.7b and 2.7d), depending on species reactivity and their positions within the geometry. These results indicate that more reactive species, such as e_h^- (Fig. 2.7a), remain concentrated near the irradiated region, while less reactive species, like H_2, diffuse and accumulate across the cell over time, as shown in Fig. 2.7c. As a result, the system now requires a longer time to reach equilibrium, with t_{ss} determined by diffusion occurring over tens of seconds (Figs. 2.7b and 2.7d). These results further indicate that an exact geometric replication of experimental realities is required to ensure accurate solutions.

2.3.1. Radiolysis Models Extensions

The Schneider model is used as the basis for most radiolysis simulations in this specialised field of microscopy. Although advancements in modelling have opened new possibilities for studying electron-water interactions in LP-TEM, especially compared to experimental approaches, these models still require further refinement in their theoretical assumptions to become fully quantitative. This comprises chemical, geometrical, and physical aspects, as outlined in the following.

Chemical Reactions Studies Most studies in this area use the 0D model of radiolysis, often adding new reaction pathways to model the radiolysis of aqueous samples, such as metal or metal-oxide nanocrystals, polymers and other materials.[29, 83] Researchers are also developing novel radiolytic schemes for organic solvents,[84, 85] investigating the effects of local heating on chemical species,[86, 21] and studying pH modifications under electron irradiation.[87] These models provide valuable insights into the underlying kinetics of reactions, revealing novel aspects of solution chemistry changes under extreme irradiation conditions, such as in confined graphene liquid cells.[88]

Geometrical Studies. In contrast, diffusion models (in the 1D case) have facilitated the analysis of spatial effects in radiolysis, including H_2 saturation conditions that lead to gas formation in the cell [26] and dose enhancement at metal-water interfaces.[22]

Despite these advancements, current radiolysis models widely rely on 0D implementations, which represents an oversimplification of the imaging conditions specific to LP-TEM studies. One critical aspect often overlooked is the discrepancy between TEM and STEM modes. The scanning beam in STEM introduces significant changes in geometry, disrupting the circular symmetry assumed by the 1D TEM implementations. Figures 2.8a and 2.8b show the single irradiation profile of a focused STEM beam using the same 1D model, highlighting how the position of previous or subsequent irradiations requires a shift in the radial axis. This complexity points to the need for geometrical considerations and spatio-temporally dependent radiolysis production.

Although one study has attempted to predict radiolysis under multi-irradiation conditions, these efforts have primarily focused on demonstrating the accumulation of less reactive species. [89] This effect can be observed in the irradiation profile of H_2 in Fig. 2.8b, where hydrogen (species that also accumulate in the 0D case, Fig. 2.6a) across the space alters the initial chemical conditions for subsequent irradiations (grey shaded areas).

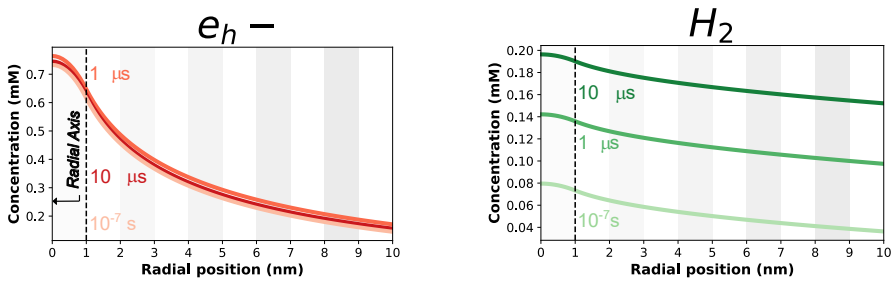

Figure 2.8: Heterogeneous STEM Irradiation Modeling of Radiolysis (1D Radial). **a, b)** Spatial concentration profiles for a single focused irradiation are generated with an absorbed dose rate corresponding to a 300 keV beam of 1 nm radius and 80 pA current, 6×10^{12} Gy/s. The axis of radial symmetry (*black arrow*) compromises the validity of the 1D model for STEM applications, where areas irradiated subsequently (*grey shaded areas*) underscore the radiation background effect from the initial simulated beam **a)**. The e_h^- species reach a quasi-steady state rapidly (t = $1\mu\,s$). **b)** The concentration of H_2 species continues to increase at typical STEM irradiation times.

Mass Transport Studies. Finally, the influence of external stimuli applied within LP-TEM holders (e.g. fluid flow, electric biasing etc.[3]), can significantly alter the mass transport of radiolytic species. To understand non-inherent physics, such as flow or drift currents induced by applied voltage, the use of multiphysics and dimensional models introduces significant changes. Some of the models implemented so far address these physical processes individually, such as charge migration in electrochemical liquid cells [90] and the flow properties in μm- or nanometre-sized channels of a setup for flow experiments.[91] But had not been coupled to radiation chemistry models before this thesis was conducted.

2.3.2. Impact of Dose Rate on Radiolytic Yields in TEM.

All the models presented so far in LP-TEM rely on G values or yields corresponding to timescales exceeding 1 µs, as already mentioned above. This knowledge which applies to nuclear reactors (i.e. γ and neutron rays) with a dose rate (ψ) ranging from 1 Gy/s to 1 kGy/s,[76] it was then uncritically extended to LP-TEM applications, which involve significantly higher dose rates, either through TEM irradiation at $1-100$ MGy/s or STEM focused beams, delivering instantaneous dose rate between 10^5-10^9 MGy/s. The extremely elevated fluxes in EM, especially when irradiation is focused on areas of a few angstroms or nanometers (STEM), overlap between spurs generated by different electrons can lead to

[3]Protochips, "Introduction to Poseidon Select In Situ TEM Liquid Cell," YouTube video, 3:22, August 11, 2017, https://www.protochips.com/solutions/in-situ-tem-solutions/in-situ-liquid-cell/

conditions similar to those seen with high LET energy transfer (Fig.2.3a).

However, this scenario has not been thoroughly explored in the LP-TEM community, except for the purely geometrical derivation (excluding diffusion and reactions) of dose rate effects in STEM and TEM, as derived by Grogan et al.[26] The authors concluded that in TEM imaging, spur overlap would not occur at any dose rates. In contrast, a stationary STEM beam was found to induce spur overlap, potentially significantly altering chemical yields (G_i). The authors discussed applying high raster velocities of the beam as a possibility to avoid spur overlap between different scans. The noted discrepancy (TEM versus STEM) arises from the electron flux being different for the operational conditions. This finding highlights the need for a revision of yields through a model that incorporates primary reactions (i.e., the chemical regime) and diffusion in spur geometries under experimentally relevant flux conditions.

2.3.3. Other Simulation and Experimental Attempts

Given the implications discussed above, there remains an urgent need for methods to experimentally quantify solution chemistry under electron irradiation, i.e. radiolysis, since the chemical species generated by the electron beam are not directly observable and information is typically limited to the resultant sample dynamics. Theoretical correlation with experiments is regarded as the most effective approach. In practice, researchers often leverage beam-induced reactions to study specific phenomena intentionally. Careful experimental planning, considering factors such as electron dose, acceleration voltage, and imaging mode (STEM or TEM),[19, 92] together with solution-specific reactivity factors like chemical additives or scavengers,[20, 93] helps qualitatively categorise the extent of radiation-induced damage.

Beyond radiolytic damage to the solvent, some studies have also investigated membrane damage, mainly considering knock-on effects.[94] These effects can induce electric charging and subsequent changes in the surface chemistry of liquid cell membranes.[12] Furthermore, secondary electron emission from both the membranes and the sample has been identified as another factor that affects the liquid environment.[22] However, these effects are generally

less relevant compared to solvent radiolysis.

A well-known aspect of radiation chemistry is that the species in solution are ionised in proportion to their relative concentrations.[95] LP-TEM experiments typically involve dilute solutions ($\leq 0.1\,\mathrm{M}$), leading to the conclusion that water [23]—and in some cases, other organic solvents [84]—plays the primary role in maintaining radiolytic reaction chains, allowing solute radiolysis to be largely ignored. This assumption generally holds, except in cases where the concentrations of solutes increase, as previously studied in graphene liquid cells (GLC).[88] In MEMS-based liquid cells, for the larger solution volumes, the assumption typically remains valid.[25]

Some experimental work on the quantification of radiolytic species in the context of LP-TEM was reported. A significant achievement was the collection of quantitative EELS spectra on the composition of thin ice layers irradiated, as these are assumed to produce similar radiolysis products as liquids.[27] Another approach used electrochemical methods to detect stable radiolytic species in in situ SEM in liquid setups.[96]. Although these experimental works tried to achieve correlation with the theoretical models, substantial challenges remain. One of the most critical challenges is to accurately replicate the experimental conditions when implementing models.

CHAPTER 3

METHODOLOGY OF A RADIOLYSIS MODEL IMPLEMENTATION.

3.1. Introduction

Various computational approaches are employed in radiolysis modeling, including Monte Carlo simulations to track early electron-specimen interactions and subsequent diffusion-kinetics.[97, 98, 99] While highly accurate for calculating initial yields, Monte Carlo simulations are less suitable for the long timescales involved in LP-TEM imaging. There are ordinary differential equations (ODEs) that are particularly useful for solving reaction kinetics. Due to their dependence on only one independent variable, they are well-suited for modelling concentration dependencies in a homogeneous environment, typically represented as zero-dimensional (0D) systems.

The Finite Element Method (FEM) is well suited for expansion into complex space- and time-dependent studies, as it is a robust numerical technique for finding numerical solutions to problems governed by partial differential equations (PDEs).[100] While FEM continues to dominate engineering applications, it is also gaining attraction in the field of nanoscience, particularly for automated experimental analysis.[101] This versatile method is applied to physical objects that represent real-world geometries in a multiscale environment, which can be divided into numerous smaller elements of defined shape and size. In continuum theory, each finite element serves as a numerical integration field with uniform properties, such as material behaviour or stress distribution.

The main feature of FEM is discretization through the creation of a mesh composed of finite elements (e.g., triangles and quadrilaterals for 2D domains, tetrahedra, and hexahedra for 3D domains). The solution on each element is assumed to be expressed by a linear combination of base functions or shape functions, with the coefficients of this combination becoming the unknowns of the algebraic problem post-discretization. This approach allows for mesh discretization, accommodating elements of varying sizes where necessary, especially in areas with significant gradients.

Although Monte Carlo methods have proven limited, FEM emerged as an optimal tool to address the complexities of LP-TEM irradiation scenarios in a holistic manner. FEM is particularly valuable for simulating intricate geometries and physical phenomena and is widely accessible through user-friendly platforms like Comsol Multiphysics,[102] which was the primary software used to develop the results in this thesis.

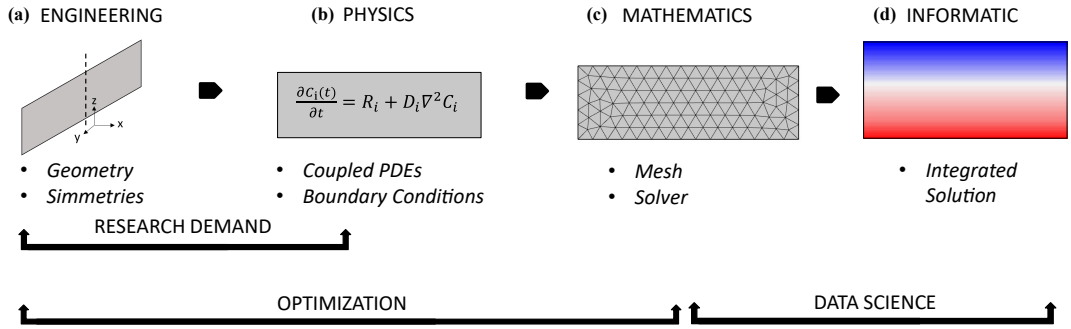

Figure 3.1: Schematic of building blocks of a workflow used in Comsol Multiphysics for developing a new model for LP-TEM.

In this chapter, a general methodology for implementing comprehensive models of radiation chemistry and mass transport is introduced. The chapter is intended to serve as a modular construction kit for the models presented in this thesis, as well as for the research community in general. It follows the general workflow of finite element modelling depicted in Fig. 3.1 by addressing each of the key building blocks. Guidance is provided on geometrical aspects (Section 3.2), physical interpretations and formulations (section 3.3), as well as aspects of the model's implementation, such as meshing and solvers (section 3.4), and principles used in a script-based environment for automation and analysis (Fig. 3.1d; Section 3.5).

3.2. Geometric Modelling

The geometry of liquid reactors for radiolysis modelling specifically refers to the liquid cell (LC). In LP-TEM, the commonly used cells are graphene liquid cells (GLCs) (Fig. 3.2a) as well as MEMS-based cells. In GLCs, two graphene layers enclose the solution in liquid pockets of random dimensions that are a few tens to hundreds of nanometres in diameter. As a result, the cell is closed and the water is highly confined. In MEMS-based cells, the liquid layer is sandwiched between silicon nitride (SiN) membranes (Fig. 3.2b), which are supported by silicon chips that provide structural support. These chips are rather large, typically spanning a few millimetres in length, compared to the submicrometre thin liquid layer. The liquid layer thickness is defined by spacers, pillars deposited on the chip. Unlike the closed geometry of GLCs, MEMS chips can feature an open and engineered structure, meaning that characteristics such as channel design, spacer height, and edge connections can vary depending on the chip type. This results in a variety of cell architectures available.

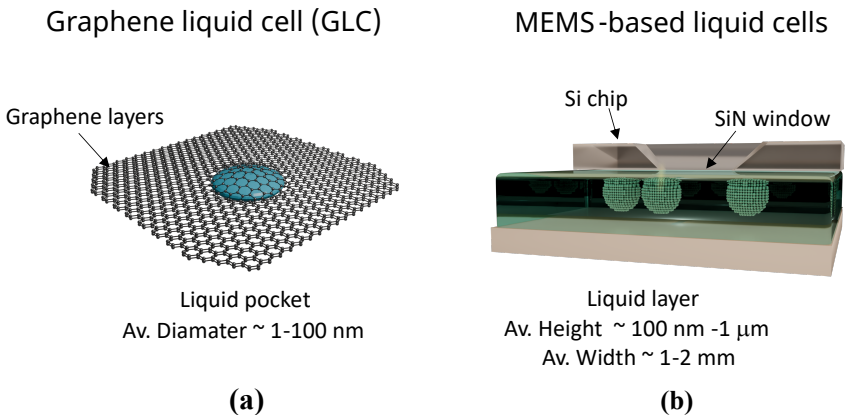

Figure 3.2: The Liquid Cell (LC) Concept. Liquid samples are enclosed between electron beam-transparent windows to protect the solution from the high vacuum environment of the TEM microscope. **(a)** Graphene Liquid Cells (GLCs) use two sheets of graphene, supported by a grid, to create multiple liquid pockets of varying and random sizes. These pockets have an average diameter that can be estimated but are not strictly controlled. **(b)** MEMS-based chips offer greater potential for LC engineering, allowing for improved experimental reproducibility through precise structural design. These chips can integrate additional features such as heating, cooling, electrical biasing, and solution exchange.

Simple geometries can be built from scratch using cuboids, planes, segments, etc., as they are predefined elements in Comsol. For more complex cases, virtual imprinting (i.e. CAD

files) could be applied. This becomes particularly important when simulating the additional functionalities of LP-TEM holders, which feature complex structural elements integrated with the MEMS-based liquid cell (fluid pathways, metallic contacts for heating, cooling, and electric bias).[90, 91]

Simplifications may be necessary to reduce the computational cost due to the extensive coupled kinetic equations. The entire geometry of an LC (a cuboid in Fig. 3.3a) can be challenging to solve when radiolysis is included, for this reason, low-dimensional geometries and symmetry aspects (derived from considerations in the physics sections 3.3.4 and 3.3.5) were considered. The 1D geometry with circular symmetry is possible since the beam is a cylindrical volume (Fig. 3.3b) and this model is assumed from diffusion considerations in liquid cells (detailed in Section 4.2.1). The 2D horizontal or vertical Cartesian planes (Fig. 3.3c) are the main geometries for conducting most of the simulations in this work in the context of convection transport of species (results of this simplification are explained in Chapter 4, section 4.3).

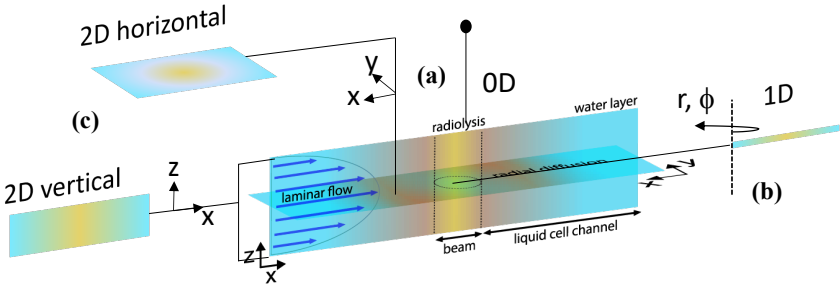

Figure 3.3: Conceptual scheme of geometric modelling for LP-TEM radiolysis, beam volumes/area in yellow and liquid water domain in blue for a **(a)** 3D Liquid cell (NC) geometry sub-divided in cut geometries (transparent planes) **(b)** 1D cylindrical coordinates and radial symmetry for open/closed channels **(c)** 2D Cartesian planes for cross-sectional description (horizontal and vertical).

Regarding irradiation scenarios, the commonly used shape was cylindrical to replicate parallel beam illumination in TEM (yellow shades in Fig. 3.3). Although this approach can be more challenging when studying the moving beam in scanning TEM (discussed in Chapter 5), the beam domain was replicated using array-structured operations. This means that

a geometry of multiple beam domains (i.e., irradiated scanning area) is included in the model, and spatio-temporal boundary conditions activate them sequentially across the solution time. This approach necessitates the use of at least 2D geometries to reproduce the displacement of the beam along the 2D horizontal plane. Additionally, other *artificial* subdivisions of the model geometry may be necessary to adapt mesh operations for a complete realistic description, as demonstrated for the "spur" model presented in Chapter 6. Geometry, when applied solely to solve chemical kinetics, does not require further geometrical implementation, as reaction rate expressions do not include spatial terms (compare with Section 3.3.1).

3.3. Physics Modelling

3.3.1. Chemical Reactions

The equation 3.1 describes the temporal evolution of the concentration c_i of the species i as sum of the consumption and production rates of all reactions between all involved radiolytic species:

$$\frac{dc_i}{dt} = -\sum_{j,k\neq i} k_{jk} c_j c_k + \sum_j k_{ij} c_i c_j \tag{3.1}$$

where k_{ij} is the consumption rate constant between species i and j, and k_{jk} is the production rate constant between species j and k. A convenient reaction set to model radiation chemistry was introduced comprising 73 reactions tabulated in A.2 among 15 radiolytic products and water.[30]

Suggestion: In reaction kinetics you may concentrate on the reaction set for water of Elliot, [30] which is known and well accepted yet contains many reactions - calculation cost. Topological kinetic analysis [103] may allow to reduce reaction set/calculation cost by exclusion of less relevant reactions. Any modifications of reaction set either reduction or expansion should be validated on 0D simulations before their expansion in complex model geometries, as demonstrated in Section 6.2.

Initial Concentrations To represent the conditions of pure water (neutral pH):

$$c_{0,i} = 0 \quad \text{for all } i \quad \text{except} \quad c_{0,\mathrm{H^+}} = c_{0,\mathrm{OH^-}} = 10^{-7}\,\mathrm{M}, \quad c_{0,\mathrm{H_2O}} = 55.56\,\mathrm{M}$$

Additionally, for any dissolved acids in the system, its dissociation must be taken into account. For a strong acid like HCl, which dissociates fully, it can be assumed:

$$c_{0,\mathrm{H^+}} = c_{0,\mathrm{Cl^-}} = c_{0,\mathrm{HCl}} = \text{acid concentration} \quad \text{(assuming complete dissociation)}.$$

For weak acids, where partial dissociation occurs, the dissociation constant K_a must be considered to calculate the equilibrium concentrations of $\mathrm{H^+}$, $\mathrm{A^-}$, and the non-dissociated acid HA:

$$c_{0,\mathrm{HA}} = \text{initial acid concentration}, \quad c_{0,\mathrm{H^+}} \text{ and } c_{0,\mathrm{A^-}} \text{ determined by } K_a.$$

Suggestion: A reaction set should begin with well-defined initial species concentrations for both the solvent and the sample, such as pH value, dissolved gases, or diluted reactants.[31]

Order of the Reaction. Units of the rate constant k vary depending on the overall order of the reaction. For a first-order reaction, k has units of $\mathrm{s^{-1}}$, while for a second-order reaction, k has units of $\mathrm{M^{-1}s^{-1}}$, etc. The unit of k ensures that the rate has units of concentration per time, typically M/s. Implementing reaction rate expressions in computational codes is intricate, particularly when multiple reactions are involved. It is essential to verify that the units of the rate constant k correspond to the overall order n of the reaction to prevent errors. In the mathematical model [30] where water acts as a solvent ($c_{\mathrm{H2O}} \gg c_i$), the methods for implementing reaction rates are twofold: 1) omitting water as an educt in production terms and using the constant expression by multiplying it by the water concentration, thus assuming $(n-1)$-order reaction. 2) considering water as an educt and using the formula for k with respect to units of n - order reaction. Both options are compared in Table A.2. Note that consumption terms of the form:

$$\frac{dc_i}{dt} = -k_{ij} \cdot c_i \cdot c_j \tag{3.2}$$

are quasi-first-order with respect to c_i (where c_j represents the concentration of another reactant). In the set of radiolysis water (see the Appendix A.1), only the radiolytic generation of the primary species follows zero-order kinetics (see below), whereas only four consump-

tion reactions (#24, #34, #52, and #58 in table A.2) are of the second order, making most reactions quasi-first-order regarding the consumed species, as described by the equation 3.2.

3.3.2. Radiolytic Generation

The chemical network for radiolysis is influenced by a set of generation terms R_i, which depend strongly on the energy deposited by the electron beam and various constants. R_i is the radiolytic production of the primary species ($e_h{}^-$, $H^\bullet$, H_2, $OH^\bullet$, H_2O_2, $HO_2{}^\bullet$, H^+, OH^-).

$$R_i = \frac{\rho \, \psi \, G_i}{F} \tag{3.3}$$

Here, G_i is the G-value of species i, based on experiments or calculations (reviewed in Section 2.2.4). ρ is the mass density of the medium (g/cm^3), and F represents the Faraday constant (C/mol). ψ is the dose rate absorbed by the beam, and is derived in detail in the next subsection. Consequently, Equation 3.1 introduces an additional term as follows:

$$\frac{dc_i}{dt} = R_i - \sum_{j,k \neq i} k_{jk} c_j c_k + \sum_j k_{ij} c_i c_j \tag{3.4}$$

It is important to note that while this term is presented in the context of electron microscopy, by adjusting the relevant quantities, the entire implementation can be adapted for other techniques involving ionising radiation and chemical reaction generation, such as biomedical applications or X-ray measurements. In this thesis, these values are applied to model radiolysis in pristine water. [23] Furthermore, determining the absorbed dose ψ in the model requires accounting for changes in the average energy loss, commonly referred to as stopping power. The application of this concept is also discussed in the following subsection.

Absorbed dose. The amount of energy transferred to the medium by inelastic scattering of electrons in water is quantified in terms of ionising radiation dose, with *Gray* (1 Gy = 1 J/kg) being the SI unit. The absorbed dose rate in TEM is derived from the stopping power of electrons in water:[104, 24]

$$S = \frac{dE}{dx} = \rho S \tag{3.5}$$

often referred to as the density-normalised stopping power ($S = \rho S$) with its customary units (MeV/cm^2·g). From this energy loss, one can calculate the dose released by a single electron within the average distance travelled d until stop, per unit of mass, as derived by Schneider [82].

$$dose_{e^-} = \frac{\frac{dE}{dx} d}{\rho V_I} = \frac{S d}{V_I} \quad (\text{eV/kg}) \tag{3.6}$$

Note that in the Equation 3.6, the stopping power from Equation 3.5 is substituted. The irradiated volume, V_I, is assumed to have a cylindrical beam shape with a circular area A_{beam} (m^2) and a height comparable to the thickness of the liquid layer, h (m). The total dose rate can be expressed by multiplying the single electron dose rate by the total number of electrons per second, J, resulting in

$$\psi = \frac{S\ d}{A_{beam}\, h}\ J \quad (\text{J} \,/\, \text{kg} \cdot \text{s}) \tag{3.7}$$

Converting this total dose rate into quantities used in microscopy involves assuming the definition of J in terms of flux:

$$J = \phi\, A_{beam} \quad (\text{electron} \,/\, \text{s}) \tag{3.8}$$

By substituting Eq. 3.8 into Eq. 3.7 it is possible to access the simple conversion from the dose rate to the electron flux density, a quantity read at the microscope, in units equivalent to Eq. 3.7:

$$\psi = \frac{S\, \phi\, d}{h} \quad (\text{J} \,/\, \text{kg} \cdot \text{s}) \tag{3.9}$$

since the relationship between electron flux density (ϕ) and the beam current, I (A):

$$\phi = \frac{I}{A_{beam}\, e} \quad (\text{electron} \,/\, \text{m}^2 \cdot \text{s}) \tag{3.10}$$

with e the electron elementary charge (C). The beam current can be included in Eq. 3.9:

$$\psi = \frac{S\, I\, d}{A_{beam}\, e\, h} \quad (\text{J} \,/\, \text{kg} \cdot \text{s}) \tag{3.11}$$

In cases where the liquid layer thickness is comparable to the inelastic mean free path of the electron in water, i.e. a few hundred nanometres ($\lambda_{\mathrm{IMFP}} = 267$ nm at 300 kV),[61] the electron can be assumed to undergo *one scattering* and it's distance, d, travelled - on average - to be approximately equal to the liquid layer thickness, h. The first-order approximation of d can be applied if the height h is significantly less than the distance an electron travels before coming to rest or range, [105] which, at electron microscopy voltages, is approximately 400 μm,[61] while the liquid sample typically reaches maximum heights of a few μm.

$$d = h\left(1 + \frac{h}{\lambda_{IMFP}}\right) \quad \text{(m)} \tag{3.12}$$

In thicker liquid layers, multiple scattering occurs and leads to an increase in energy deposited by a single electron, as the electron travels distances that are significantly longer than λ_{IMFP}. By substituting Eq. 3.12 into the absorbed dose rate for equation 3.11 the first order estimate of dose rate gives:

$$\psi = \frac{S\,I}{A_{beam}\,e}\left(1 + \frac{h}{\lambda_{IMFP}}\right) \quad \text{(J / kg ·s)} \tag{3.13}$$

All the models presented in this thesis assume $h \sim d$, i.e. single scattering of electrons, allowing the expansion introduced in Eq. 3.13 to be omitted. This simplification is generally accepted in most cases of LP-TEM.[29]

3.3.3. Convection-Diffusion-Reactions Coupling.

The previously introduced chemical reaction equations describe a spatially homogeneous concentration distribution, which can be simulated in a 0D model. However, chemistry alone does not fully account for the behavior of species in heterogeneously irradiated scenarios, which requires models with dimensions higher than 0D. In these scenarios, different transport phenomena may become relevant, namely diffusion and convection.

First, diffusion of species relative to bulk motion must be solved, requiring the inclusion of Fick's second law.

Second, when there is convection , an associated flux, known as advective flux, arises. This

leads to the convection-diffusion equation from the continuity principles.[106] This description implies that spatial dependent terms are calculated and leads to the equation governing the concentration fields $c_i(x, y, z, t)$ in three dimensions for radiolytic species i is given by: [28]

$$\frac{\partial c_i}{\partial t} = R_i - \sum_{j,k \neq i} k_{jk} c_j c_k + \sum_j k_{ij} c_i c_j + D_i \nabla^2 c_i + \mathbf{v} \cdot (\nabla c_i) \tag{3.14}$$

The first, second, and third terms on the right-hand side of Eq. 3.14 describe chemical reactions and generation by the electron beam. The fourth term represents diffusion, where D_i is the diffusion coefficient of species i and $\nabla^2 c_i$ is the Laplacian operator, which describes the spatial distribution of species i in all directions. The final term represents convection, where $\mathbf{v}$ is the velocity of the liquid flow, and ∇c_i represents the concentration gradient of the species i.

This equation represents the state-of-the-art in LP-TEM. Couple transport physics with beam generation and the radiolysis network. In the following paragraphs, the equation is decoupled and explained for each of the transport mechanisms, addressing symmetries and boundary solutions with reference to thin liquid cell geometries. The correct implementation of the convection term, in particular, associated with the radiolysis boundary problem in LP-TEM has been significantly advanced in this work (see Chapter 4).

3.3.4. Diffusion Mass Transport

Brownian Motion of Particles. Einstein's theory on Brownian motion [107] provided a fundamental understanding of the motion of solutes in a fluid. Einstein derived that the mean square displacement (MSD) in three dimensions for a particle undergoing Brownian motion is related to the diffusion coefficient, which quantifies how fast particles are diffusing through the fluid. Since the diffusion is isotropic, the MSD in three dimensions is:

$$\langle r^2 \rangle = 6 D_i t \tag{3.15}$$

The diffusion coefficient D_i is derived from the macroscopic properties of the particles and the medium. According to Einstein and Stokes, D_i is given by the relation:

$$D_i = \frac{k_B T}{6\pi\eta r}, \tag{3.16}$$

where k_B is the Boltzmann constant, T is the absolute temperature, η is the viscosity of the medium, and r is the radius of the diffusing particles. By measuring these physical quantities, the diffusion coefficient can be experimentally determined, providing insights into the dynamics of particle movement in various environments. The diffusion coefficient of radiolytic species in water is $\sim$ 1-10 nm^2/s.[23]

Bulk Diffusion. Bulk diffusion refers to the movement of solutes through a medium due to concentration gradients. It is described by Fick's laws. Fick's first law expresses the flux $\mathbf{J}_i$ resulting from a concentration gradient as follows:

$$\mathbf{J}_i = -D_i \nabla c_i \tag{3.17}$$

This law provides the foundation for understanding how species diffuse from regions of high concentration to low concentration. Complementing this, Fick's second law, derived from the first law and the principle of mass conservation, describes the time evolution of the concentration:

$$\frac{\partial c_i}{\partial t} = D_i \nabla^2 c_i \tag{3.18}$$

Symmetries. It is always important to visualise the solution of an equation within the constraints of the system under study, to develop symmetry operations and reduce the cost of a computation. The solution of Fick's 2^{nd} law for diffusion of chemical species (third right-hand term of Eq. 3.14) for an initial concentration located at the origin ($(x, y) = 0$ at $t = 0$) is given by a Gaussian distribution:

$$c(x, y, t) = \frac{1}{\sqrt{4\pi D_i t}} \exp\left(-\frac{x^2 + y^2}{4 D_i t}\right) \tag{3.19}$$

In Fig. 3.4a, the function is depicted in two dimensions, and can be associated to the case of a non uniformly irradiated liquid cell, with the third dimension being hindered by the homogeneous beam. This feature can be observed in the 2D solution translated in the 3^{rd} dimension (XZ-plane) as shown in Fig. 3.4b. This follows from the translational symmetry of the system. Figures 3.4b and c illustrate the diffusion zone after homogeneous beam generation in the vertical 2D geometry of a liquid cell for TEM (Fig. 3.4b), as well as the radial profile across the horizontal 2D geometry (Fig. 3.4c). In the XZ view, two closed boundaries are imposed by the electron-transparent membranes, while in the XY plane, the boundary conditions are chosen based on the geometries of the system. Section 4.5.1 provides a detailed explanation of how these conditions apply to typical LP-TEM setups.

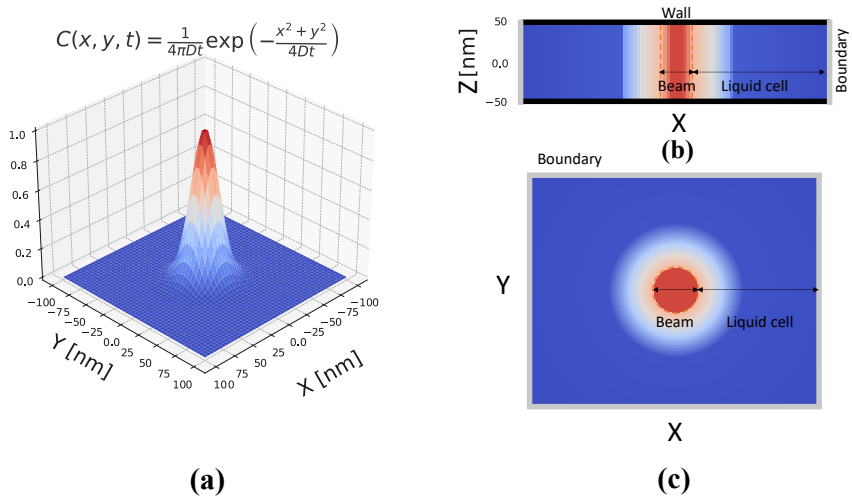

Figure 3.4: Diffusion modelling for symmetry visualization: **(a)** Concentration distribution of Fick's 2nd law for diffusion is shown in the xy-plane with the characteristic length of the TEM beam irradiation. **(b)** Liquid cell cross-section in the xz-plane, representing homogeneous concentration along the z-axis due to boundary conditions. **(c)** Liquid cell cross-section in the xy-plane, illustrating radial concentration gradients.

Symmetries are a valuable resource for potentially accelerating calculations without sacrificing precision. In both models (Fig. 3.4b and c), radial symmetry is observed and is applicable by a change of coordinates in a cylindrical system (r, θ, z).

Boundary Conditions. For the boundary conditions, the following can be applied in the contour of the model (edges in Fig. 3.4 b, c):

1. **Impermeable Boundary (wall)**:

$$-\mathbf{n} \cdot (-D_i \nabla c_i) = 0 \tag{3.20}$$

This implies no flux through the boundary, allowing for free exchange of species.

2. **Open Boundary**:

$$c_i = c_{0,i} \tag{3.21}$$

This condition fixes the concentration at the boundary to initial values, reflecting continuous influx.

3.3.5. Fluid Dynamics

Navier Stokes Equations for Incompressible Fluids. The *Computational Fluid Dynamics* interface in Comsol allows for modelling the general Navier-Stokes equation, implemented under both stationary ($\frac{\partial v}{\partial t} = 0$) and time-dependent conditions:

$$\rho \frac{\partial v}{\partial t} + \rho(\nabla \mathbf{v})\mathbf{v} = \nabla \left[-p\mathbf{I} + \mu(\nabla \mathbf{v} + (\nabla \mathbf{v})^T)\right] + \mathbf{F} \tag{3.22}$$

assuming an incompressible and unidirectional fluid

$$\rho \nabla \cdot \mathbf{v} = 0 \tag{3.23}$$

where μ is the dynamic viscosity, $\mathbf{v}$ is the velocity vector, ρ is the constant solvent density, and $\mathbf{I}$ is the identity tensor. All body forces applied $\mathbf{F}$, such as gravity, are set to 0.

The term $\nabla \left[-p\mathbf{I} + \mu(\nabla \mathbf{v} + (\nabla \mathbf{v})^T)\right]$ represents the total stress in the fluid, which includes both pressure and viscous stresses. Here, $-p\mathbf{I}$ represents the isotropic pressure and $\mu(\nabla \mathbf{v} + (\nabla \mathbf{v})^T)$ represents the viscous stress tensor. Finally, ∇ is the differential operator with respect to spatial coordinates, and the Cauchy stress tensor, $\mathbf{P} = \left[-p\mathbf{I} + \mu(\nabla \mathbf{v} + (\nabla \mathbf{v})^T)\right]$, describes the stress due to both pressure and viscosity acting on the fluid. The Navier-Stokes equation must be solved to obtain the velocity field (vector) in Eq. 3.14.

Flow Regime Estimation. The nature of the flow, whether turbulent or laminar, can be determined by the characteristic Reynolds number. The Reynolds number Re for flow in a rectangular channel can be calculated using the formula:[108]

$$Re = \frac{\rho \cdot v \cdot D_H}{\mu} \tag{3.24}$$

where, ρ, μ, v are the fluid density, the dynamic viscosity, and the mean velocity of the fluid respectively. D_H describes a characteristic length of the flow channel.[91] A Reynolds number below approximately 2100 signifies laminar flow. In typical microfluidic applications, including LP-TEM cells, the Reynolds number is well below 1,[91] indicating laminar flow conditions. The resulting flow can be expressed by simplifying the Navier-Stokes equations for steady, unidirectional flow, neglecting inertial and gravitational forces.

A Newtonian fluid flowing between two infinitely long parallel plates, as in the geometry in Fig. 3.5b, the fluid naturally moves from areas of higher pressure to areas of lower pressure to equalise the pressure difference, as described below:[109]

$$\frac{dp}{dx} = \mu \frac{d^2 v}{dz^2} \tag{3.25}$$

where p is the pressure, μ is the dynamic viscosity and v is the velocity. The physical interpretation for this governing equation emphasises the balance between the net pressure forces and the net viscous forces on hypothetical control volume inside the liquid. Since the pressure gradient, i.e. left hand term, is assumed uniform, the concavity (i.e., the second derivative with respect to z) of the velocity distribution is uniform.

By applying the *no-slip* boundary conditions at the walls to Eq. 3.25, which are: **(a)** $v(z) = 0$ at $z = -h/2$ and **(b)** $v(z) = 0$ at $z = h/2$ (refer to the geometry in Fig. 3.5 b), and integrating with respect to z, the velocity profile assumes a parabolic form, characteristic of Poiseuille flow [109]:

$$v(z) = -\frac{1}{2\mu} \frac{dp}{dx} \left(h^2 - z^2\right) \tag{3.26}$$

For the limiting case of a rectangular duct with width ≫ height , which is a good approximation for most LP-TEM reactors, the velocity profile can be described by the following relationship [110]:

$$v(z) = 6\frac{Q}{h^3}\left[\left(\frac{h}{2}\right)^2 - z^2\right] = \frac{3}{2}\overline{v}\left[1 - \left(\frac{2z}{h}\right)^2\right] \tag{3.27}$$

In Eq. 3.27, where Q represents the volumetric flow rate. The mean velocity, $\overline{v}$, is related to the flow rate by $\overline{v} = \frac{Q}{A}$, with A being the cross-section of the channel. Equation 3.27 describes the maximum flow velocity, $v_{\max}$, which occurs at the center of the channel and is equal to $\frac{3}{2}$ of the mean velocity, $\overline{v}$. This is further illustrated by CFD simulations, as shown in the velocity magnitude maps in Figure 3.5a.

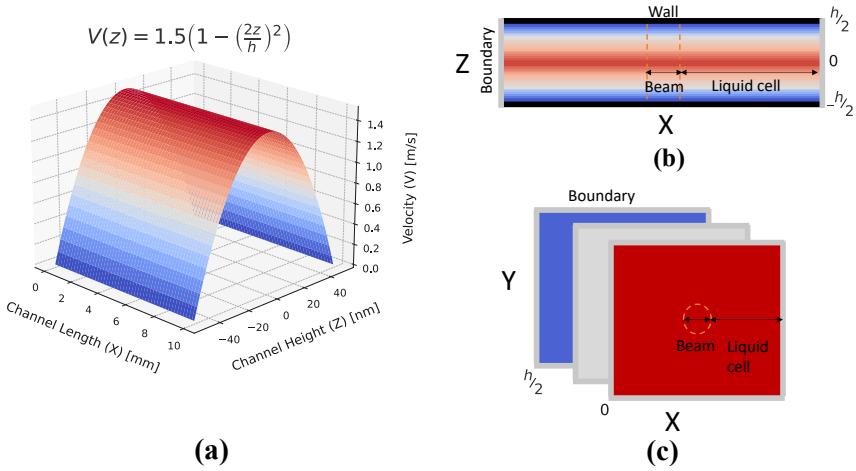

Figure 3.5: Convection modelling for narrow channels: **(a)** 2D calculated laminar flow velocity fields with no slip boundaries and high aspect ratio $w \gg h$. The velocity magnitude of the full developed flow profile ($\bar{v} = 1\,(m/s)$ at the inlet) shown across the 2D map, indicates the maximum velocity reached at the centre $h = 0$ and correspondent to $v_{\frac{h}{2}} = \frac{3}{2}\bar{v} = 1.5\,(m/s)$. **(b)** Liquid cell cross-section in the xz-plane, representing laminar flow along the z-axis. **(c)** Liquid cell cross-section in the xy-plane, illustrating constant velocity at different heights. *Note:* These cross-sections are not to scale and are provided solely to represent the velocity field in LP-TEM channels.

In Fig. 3.5, the solution of laminar flow is applied for the case of a liquid cell, illustrating the parabolic nature along the z-axis in the 2D vertical geometry (Fig. 3.5b) and the constant velocity field in the 2D horizontal geometry (Fig. 3.5c). The laminar flow profile shown in Fig. 3.5b would disrupt the radial symmetry of the diffusion profile (compare

to Symmetries paragraph in 3.3.4), thereby requiring a full-dimensional 3D model when convection and diffusion mass transport are solved together using Eq. 3.14.

Boundary Conditions. The boundary and initial conditions for laminar flow (represented in Fig.3.5 b and c) are outlined below:

1. **Inlet Flow Velocities:** The flow velocity at the inlet (left edge in Figure 3.5) is set to be uniform and unidirectional and equal to the mean flow velocity v.

$$\mathbf{v}_{\text{inlet}} = v \tag{3.28}$$

2. **No-Slip at Walls:**

$$\mathbf{v}_{\text{wall}} = 0 \tag{3.29}$$

3. **Outlet Pressure Condition:** The outlet (right edge in Figure 3.5) was defined to specify the normal stress, the tangential stress was set to zero. If the reference pressure p_{ref} is set to zero, the boundary pressure p_0 is considered the absolute pressure. If not, p_0 is treated as the relative pressure at the boundary.

$$\left[-p\mathbf{I} + \mu(\nabla\mathbf{v} + (\nabla\mathbf{v})^T)\right]\hat{\mathbf{n}} = -\hat{p}_0\hat{\mathbf{n}} \quad \text{with} \quad \hat{p}_0 \leq p_0 \tag{3.30}$$

In the calculations performed under the assumption that water is an incompressible fluid and the channel walls are hard and solid, it is convenient to set the reference pressure to zero (p_{out}). As a result, the pressure at the inlet is calculated based on the equation:

$$\Delta p = p_{out} - p_{in} = RAv \tag{3.31}$$

where v is the mean velocity as defined in the solution 3.27, A is the cross-sectional area, and R is the channel resistance, which depends strictly on the geometrical factors of the channel.[108]

3.4. Mathematics

3.4.1. Meshing

The process by which a geometric model is discretised is called *meshing*. An optimal *mesh* requires a balance between the accuracy of the solution and the computational cost. Achieving this balance often involves compromising between these factors. In general, the quality of the solution and the computational efficiency depend on the number of mesh elements generated during the meshing process.

Geometry-based Guidelines. When generating mesh elements, the primary goal is to ensure that the mesh allows the solution to converge correctly. The geometry of the model should be carefully considered, ensuring that the shape of the elements is appropriate for the meshed domain or geometry. Sub-compartments can be created to facilitate the operation. If the mesh quality is too low, it can affect the regularity of the mesh element shapes, potentially leading to inverted elements and causing convergence failure.

To avoid this, several decisions were made prior to optimisation analysis. First, as shown in Fig. 3.6 for a TEM irradiation model (a 2D horizontal cut or top view geometry, Fig. 3.4c), the irradiated area contains triangular elements that best fit within the circular beam shape (red-contoured domain in Fig. 3.6). This helps the algorithm generate a coherent mesh that effectively fills the region.[111] Other element shapes may be more suited in other models, e.g. rectangular elements for 2D vertical cuts. Second, the chosen element size inside the beam domain defines the optimised mesh in adjacent regions by ensuring a smooth transition to larger elements.

The quality parameters are then statistically evaluated throughout the mesh optimisation process, focussing on factors sensitive to the angle sizes and anisotropy of the discrete elements.[4] The quality of the mesh element is a dimensionless value between 0 and 1, where 1 represents a perfectly regular element according to the chosen quality measure, and 0 represents a degenerate element. In Fig. 3.6, the growth rate, which is a measure sensitive to the anisotropy of adjacent elements, is extracted from Comsol and shown in the proximity

[4] https://doc.comsol.com

of the beam (red contours in Fig. 3.6).

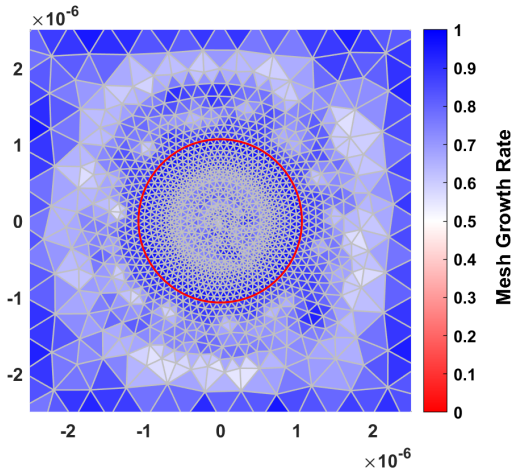

Figure 3.6: 2D mesh plot showing the mesh growth rate for a TEM irradiation model, beam area is depicted inside the red circular geometry domain.

An average mesh growth rate between 0.8 and 1 is considered optimal for convergence. The elements of the lowest quality, around 0.5 (white shades in Fig. 3.6), can be improved by modifying the element sizes in regions outside the beam, further enhancing the overall quality of the mesh. However, this process follows physics-based guidelines for the meshing problem rather than geometry considerations. It involves balancing computational efficiency and solution precision, typically governed by the specific physics of the model.

Physics-based Guidelines. A physics-improved mesh focusses on increasing the number of elements in regions where the gradients of the calculated quantities are expected to be stronger. Performing physical convergence studies by increasing the number of elements helps determine how refinement affects the accuracy of the physical solution, thereby establishing the optimal mesh resolution. In all TEM radiolysis models including space, as shown in Fig. 3.7a, the convergence study focusses on the transition from the irradiated high-concentration domain (black circle) to the non-irradiated domain, which starts with zero initial concentration. This transition is critical because it marks the beginning of concentration gradients.

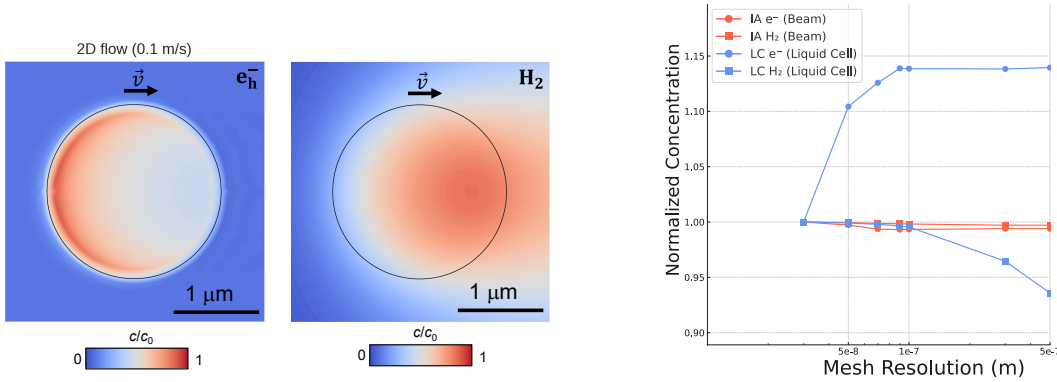

(a) **(b)**

Figure 3.7: Physics-based refinement of the mesh **a** 2D concentration maps indicates highlight gradients shape for two radiolytic species e_h^- and H_2 .**b** Averaged normalised concentrations at different mesh resolutions for the surface of the beam area (IA) and the liquid channel (LC).

The calculated solution for a convection-diffusion-reaction model (Eq. 3.14) for representative radiolytic species, namely e_h^- and H_2, generated under flow (0.1 m/s) within a TEM beam of 1 μm radius, is compared at different mesh resolutions to perform a convergence study. This model is chosen as an example because it exhibits the strongest gradients, as the interplay of various transport processes generates gradients both in the irradiated area (IA) and across the liquid cell (LC) (Fig. 3.7a). The convergence study investigates the optimal mesh size for both domains separately. The normalised concentrations averaged on the surface in the irradiated area and the liquid cell found convergence at mesh sizes of 5×10^{-8} m, as shown in Fig. 3.7b. An exception is the electron concentration in the LC, which is nearly non-existent because of reactions, so a deviation of around 10% was considered acceptable. The optimal mesh size can vary with changes in beam dimensions as the dose rate varies (see Eq. 3.13), thereby altering the established gradients.

Similarly to mesh refinement based on concentration gradients, other physical phenomena induce other gradients that require consideration during the meshing. An example is the parabolic velocity profile in the case of laminar flow. Here, the optimal mesh is refined near the walls, where no-slip boundary conditions bring the velocity to zero, creating the sharpest gradient (compare Fig. 3.5b).

Numeric Solvers. Comsol Multiphysics provides a robust solver infrastructure for finite element (FE) models, using advanced algorithms to numerically solve discretised equations. When solving coupled models, systems of non-linear equations often arise, requiring specific approaches to achieve a solution. Two primary methods used are: the segregated approach and the fully coupled approach.

The segregated approach decouples the physics and solves the equations sequentially in individual steps, requiring less memory. In contrast, fully-coupled solvers handle all interconnected equations simultaneously, resulting in a more integrated solution process. For both methods the solution is approached by iteration, but fully coupled solvers often converge more robustly and with fewer iterations compared to the segregated approach. Fully coupled methods are commonly employed, with the automatic Newton method being the preferred choice for adjusting step sizes.[102]

Regardless of whether a fully coupled or segregated approach is used, each iteration requires solving a linearised system of equations. In most cases, direct solvers such as the Multifrontal Massively Parallel Sparse (MUMPS) or Parallel Direct Solver (PARDISO) were utilised. Direct solvers are highly robust and can handle a wide range of problems; however, they require more memory and computational time, both of which increase significantly with larger problem sizes. In contrast, iterative solvers are more efficient in terms of memory and computation, with their resource demands scaling more gradually as the model size grows. The solver configuration used is specified for each model in the results section.

In certain cases, multiphysics problems were divided into two sequential studies. A notable example is the superposition of convective and diffusive mass transport with radiolysis reactions. Using a constant velocity profile, the flow field was first computed in a stationary step, followed by a time-dependent solution of the concentration distribution. This two-step strategy significantly reduced computation time, although it was applied cautiously to ensure that the simplified boundary conditions introduced in the stationary step did not compromise the overall accuracy of the model.

3.5. Informatics

3.5.1. Scientific Programming

Since this thesis is based on computational studies, a significant amount of data analysis and simulation work was carried out. The set of reactions for radiolysis can range from 73 reactions for water alone to hundreds when expanded to account for different chemistry.[29] MATLAB was used to automate model implementation using Comsol LiveLink for Matlab,[112] enabling communication between the Matlab scripting environment and Comsol. Two codes developed using this methodology are available on GitHub. The first code allows automated generation of reaction kinetics models [5]. The second script runs simulations for STEM solutions. The code is still not public in the Github repository as the manuscript is in preparation, and its working principles are detailed in Chapter 5.

The automated workflow is accessible for other researchers interested in conducting their own simulations, a code-based model implementation approach was developed in collaboration with researchers from the Hiern Institute in Erlangen (*De Salvo, Merkens et al., manuscript under review at iScience*). The workflow operates as follows: the three source tables from a hypothetical database are provided as in Github (Fig. 3.8 b). These files are transferred for a reaction network validated in 0D (Fig. 3.8 c) to a geometrically and physically expanded model (Fig. 3.8 d). For 0D validation, AuRaCh [29] is used for the capability to test the reaction network for mass and charge balance.

[5] https://github.com/GDSalvo/GDSalvo

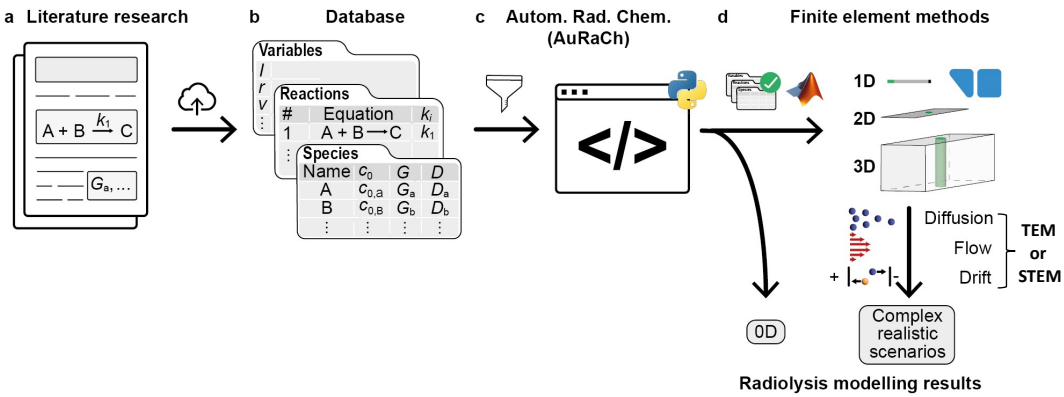

Figure 3.8: Illustration of the workflow for comprehensive LP-TEM radiolysis modelling workflow. **a, b)** Key parameters for chemical reactions (reaction constant k_i, G value G_i, diffusion coefficient D_i) are taken from the literature (a) and uploaded to a global database (b). The database is further enriched with experiment-specific data, including initial concentrations (c_0), beam parameters (current I and radius r), and external stimuli (flow velocity v, electric bias V).**c, d)** A reaction set is assembled from the database and validated using the Python-based AuRaCh tool (c), which also offers basic 0D reaction kinetic modeling **(d)**. The validated reaction set is then transferred to a COMSOL environment, enabling simulations of realistic irradiation scenarios that account for diffusion, convection, and drift ionic currents.

In practice, a reaction engineering model that can contain up to hundreds of coupled equations (equivalent to a 0D reaction kinetics model in the Comsol terminology) is created using three AuRaCh validated tables. The workflow, reproduced in Fig. 3.8, has great potential if deployed through a web-based database platform. Such a platform would allow researchers and students to easily access and interact with the workflow, providing a fast, versatile, and comprehensive model for conducting insightful and straightforward radiolysis analysis in LP-TEM.

Python, an open-source programming environment widely used in data science, was used for data analysis, its libraries such as NumPy, pandas, and matplotlib were used to process and visualise large datasets efficiently.[113]

3.5.2. Data Analysis

To facilitate understanding of the studies presented in this thesis, it is necessary to introduce key mathematical relationships related to kinetics and mass transport equations. These concepts will simplify the comprehension of a coupled model, which involves multiple terms

contributing to a unique complex solution. The concept of reaction lifetimes provides an estimate of the time at which species are fully consumed, as well as the convection-diffusion travel times indicating how far the species will move in a certain direction, but only when the travel time is shorter than the lifetime. These terms will reappear in the results presented in Sections 4.5.2 and 4.5.4.

Lifetime of Reactants. The lifetime τ of a decaying or consumed atomic/molecular species is a crucial concept in chemistry. This quantity reflects the time expected for the species' concentration to decrease to a fraction $1/x$, typically a half-life, i.e., 1/2:

$$c(\tau) = \frac{c_0}{x} \tag{3.32}$$

To determine τ, understanding how the decay rate varies with the reaction order is essential. For an n-th order reaction, the rate equation is:

$$\frac{dc}{dt} = -kc^n \tag{3.33}$$

where k is the rate constant. Integration of these rate laws yields the half-life for each reaction order, with τ inversely proportional to k and differentiated by coefficients a specific to the reaction order: $\frac{c_0}{2}$ for 0-th order, $\ln(2)$ for 1-st order, and $\frac{1}{c_0}$ for 2-nd order:

$$\tau = \frac{a}{k} \tag{3.34}$$

It is noteworthy that the characteristic time τ for first-order reactions is unique in that it does not depend on concentration, thus directly characterizing the process itself (e.g., radioactive decay). To unify the concept of τ across all reaction orders, a similar metric, referred to by IUPAC as "decay time",[114] can be defined for species undergoing zero, first and second order reactions, with constant coefficients omitted.[115]

Zero-order reactions:

$$\frac{dc}{dt} = -k \quad \Rightarrow \quad \tau = \frac{c}{k} \tag{3.35}$$

First-order reactions:

$$\frac{dc}{dt} = -k \cdot c \quad \Rightarrow \quad \tau = \frac{1}{k} \tag{3.36}$$

Second-order reactions:

$$\frac{dc}{dt} = -k \cdot c^2 \quad \Rightarrow \quad \tau = \frac{1}{kc} \tag{3.37}$$

It is noted that zero-order decay is relatively rare and included here for completeness, for zero and second-order reactions, τ depends on the current concentration, defined only as a time function. When the reaction rate $r = -\frac{dc}{dt}$ is determined from time-dependent data, then τ is given by:

$$\tau = \frac{c}{r} \tag{3.38}$$

This general definition allows τ to represent the instantaneous estimate of when the species will be completely consumed, assuming no concurrent production. For complex reaction networks, as found in LP-TEM, r is the sum of all consumption reactions including the orders 0, 1^{st} and 2^{nd}. Eq. 3.38 is strictly true for zero-order reactions; for higher orders, the decrease in concentration is asymptotic.

Characteristic Timescales of Mass Transport. The characteristic time of diffusion and convection are closely related concepts but may not always be identical, depending on the system and context. In scaling studies involving convection and diffusion, these terms are used to compare the relative importance of different transport mechanisms.

Fig. 3.9 illustrates two scenarios of species transport that occur in a TEM liquid flow cell irradiated by a localised electron beam (red area). In the first scenario, the chemical species produced by radiolysis gradually diffuse from the red area, while in the second, they are washed away by the stream with a parabolic flow velocity profile (as discussed in 3.3.4 and 3.3.5). It is important to note that, in practice, these two mechanisms coexist.

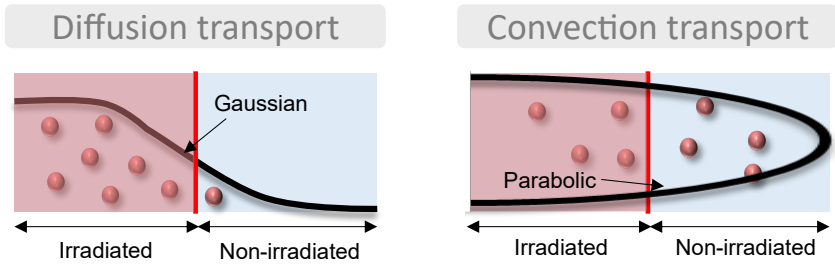

Figure 3.9: Representations of diffusion and convection transport physics transporting the species within the spatial distance of a liquid cell of electron microscopy.

Scaling Analysis. These two transport modes operate on different time and length scales, making it essential to visualise their relative contributions within the geometry of the liquid cell, which typically experiences distance channels L ranging from 1 μm to 1 mm. It will be useful for further discussion in Chapter 4 to compare the relative efficiency of both mechanisms by evaluating a specific time constant—the time required for a solute to propagate over a characteristic distance.

1. **Convective transport travel time**: The time for a species to travel a distance L under convective flow is given by:

$$t_{\text{conv}} = \frac{L}{v}$$

Where t_{conv} is the travel time due to flow, L is the distance travelled and v is the flow velocity.

2. **Diffusive transport travel time**: The time for diffusion over a distance L is given by the following relation for the mean square displacement (see Eq. 3.15):

$$t_{\text{diff}} = \frac{L^2}{2D}$$

Where t_{diff} is the diffusion travel time, and D is the diffusion coefficient.

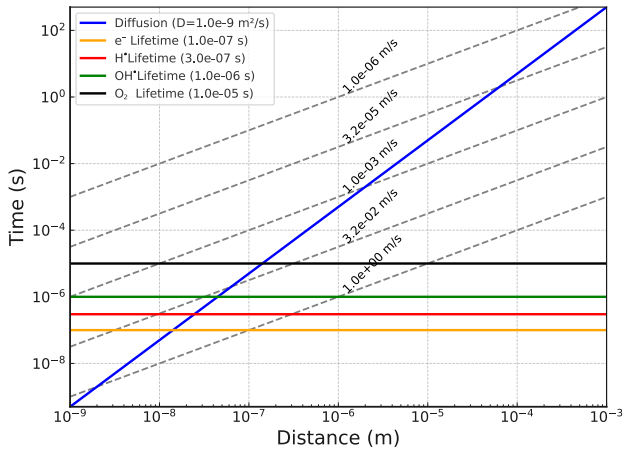

Figure 3.10: The graph illustrates the relationship between diffusion/convection transport and the lifetime of species (τ). The x-axis represents the distance travelled by a species, while the y-axis shows characteristic times: diffusion and convection time constants, as well as lifetimes. The latter are represented by constant coloured lines for four representative radiolysis products, based on the reference model of Schneider—i.e., a 1 μm beam and a 50 μm channel irradiated at approximately 10^7 Gy/s.

The velocities chosen for the analysis are based on finite element (FE) calculations in liquid flow cells. These velocities were found to not exceed 10^{-4} m / s in common holders of LP-TEM.[91, 116] However, true nanochannels were estimated to reach velocities of up to 1 m/s, which is assumed here as the upper limit of the range of velocities.[117] The diffusion coefficient of radiolytic species can be assumed $D \simeq 1 \times 10^{-9}\,\mathrm{m^2/s}$ (see Table B.1 in the Appendix for exact values). As shown in the graph (Fig. 3.10), the diagonal blue line represents the distance and travel time assumed for the diffusion of solutes in water. The grey dotted lines, on the other hand, show the same for different velocities achieved in the liquid cells. The absolute value in the plot defines whether a transport mechanism is faster than the other. The transition between dominant transport regimes is indicated by the intersection of the diffusion line with the lines that represent flow velocities. For example, at a flow velocity (v) of $10^{-3}\,\mathrm{m/s}$, diffusion dominates over flow-driven transport up to a distance of approximately 1 μm, which corresponds to the typical beam size in TEM.

Another interesting observation provided by this plot is the comparison of species' lifetimes τ (represented by the constant coloured lines in Fig. 3.10) with the characteristic transport

times. Using the size of the beam as the characteristic dimension, one can evaluate whether a radiolytic species is produced and consumed entirely within the area of the beam ($\tau < t$) or if it has time to migrate outside the beam ($\tau > t$) depending on the dominant transport mechanism. The analysis will reappear and is discussed in more detail in Chapter 4 to evaluate the migration of radiolytic species away from the irradiated region.

CHAPTER 4

A FRAMEWORK FOR ANALYSING DIFFUSION AND FLOW DYNAMICS IN LIQUID CELL GEOMETRIES

4.1. Introduction

The field of LP-TEM has gained substantial potential due to advances in microscopy setups that enable the simultaneous application of various physical conditions during measurements, such as temperature gradients, voltage bias, and fluid flow and solute diffusion. These intricate, multi-scale interactions present significant challenges for modelling. Current models often neglect critical aspects such as geometry and transport mechanisms, leading to inaccurate results. Consequently, there is a growing interest in more realistic and comprehensive models that more accurately reflect the conditions encountered in LP-TEM setups. This chapter aims to address this research gap by presenting strategies that are easy to reproduce within a versatile framework of expanded models.

Challenges of Modelling. A comprehensive model should address the (electro)-chemical reaction kinetics of the sample of interest together with the radiolysis products. It must accurately account for spatio-temporal (continuous or scanning) electron beam irradiation and incorporate all relevant mass transport mechanisms, including diffusive and convective fluxes, as well as drift currents from applied or generated voltages. Furthermore, the model should function within realistic LP-TEM reactor geometries and consider interface phenomena across liquid, solid, and gas phases. Although comprehensive coupling of these aspects into a single unified framework remains an ongoing challenge, the significant advances made in recent years mark an important step forward.[23, 28, 29] The most widely adopted approach in this field involves the incorporation of a targeted set of differential equations. The state-of-the-art kinetics modelling in LP-TEM is largely based on Schneider's 0D reaction kinetics and 1D reaction diffusion solutions,[23] applied to water radiolysis reactions from the Elliot set,[30] along with extensions for additional sample reactions.[29, 84, 83, 118] These models are zero-dimensional implementations, primarily suitable for simulating uniformly irradiated radiolysis scenarios, that is, when small amounts of water are fully irradiated in a

closed volume. This approach is particularly relevant for graphene liquid cells (GLCs),[15] as illustrated in the modelling roadmap (Fig. 4.1a).

Advancing LP-TEM Through Simulations. Recently, researchers have made various adjustments to the design of MEMS-based liquid cells (Fig. 4.1), targeting various aspects such as control of liquid thickness, [119, 94] transport properties,[120] membrane for low scattering [121] or direct mixing of chemicals. [17] When developing models for these liquid cells (LC) that feature customised nano channels (NC) of varying length and width (Fig. 4.1c),[120, 119] it is necessary to move beyond the current state of diffusion simulations.

Many existing models that incorporate diffusion properties tend to overlook the connections between liquid cells (LCs) and the liquid holder used for micro fluidics in TEM. This setup includes NCs typically surrounded by bypass reservoirs integrated into the holder. These larger liquid volumes create pathways for species to diffuse away from the NCs of interest during imaging. As a result, the effects of open-channel conditions and the width of diffusion and convection pathways have largely been neglected until now.

Flow scenarios. LP-TEM experiments can involve a variety of setups, each with its own unique characteristics, such as reagent inflow, electrochemical bias, or temperature control through heating. This diversity makes it essential to carefully consider how changes in reactivity occur due to external disturbances in the radiolysis network. These disturbances are often induced by the way molecules move through the experimental liquid reactor. One critical factor to consider is the way in which substances are transported within the liquid. Fast-moving liquid flow might affect the complex network of chemical reactions differently from slow diffusion.

In many *in-situ* experiments, liquid flow is used to replenish chemicals, keeping reactions going over extended imaging sessions. Recent advances in LP-TEM have introduced liquid flow cells (LFCs) designed to continuously refresh reaction media and reduce radiolytic effects during imaging.[122, 123] While various nano fluidic platforms with controlled flow characteristics have been developed to achieve high sample refreshing rates,[122, 116] there is still a lack of experimental and theoretical validation to support this approach.

However, recent work by this research group has taken important steps in this area by studying how liquids behave as they flow through these systems.[91, 120] This series of studies paves the way for new insights into understanding radiolysis under flow conditions and presents potential solutions for managing these effects during imaging (see Fig. 4.1d).

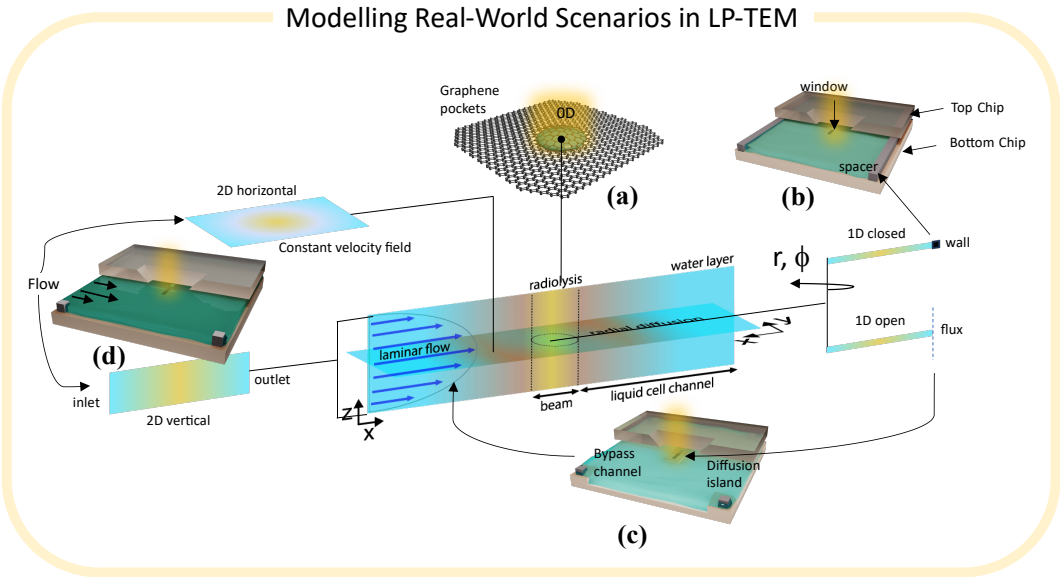

Figure 4.1: LP-TEM modelling. The central image shows a sectioned 3D model of a water layer, addressing radiolysis, diffusion, and flow physical domains. Connectors lead to **(a)** a 0D reaction model for the GLC scenario, **(b)** a 1D reaction-diffusion model for closed MEMS liquid cells, **(c)** a 1D reaction-diffusion model for customised nano-diffusion and bypass-flow channels, and **(d)** 2D vertical and horizontal reaction-diffusion-convection models for flow setups and liquid cells.

The models developed and validated in this chapter aim to advance the field by introducing two main innovations for radiolysis in LP-TEM: appropriate geometrical and boundary descriptions (e.g. fluxes and flow velocity) and the incorporation of flow physics.[28] These approaches integrate insights from FEM studies to enhance the understanding of the principles governing the transport of radiolytic species. In addition, these insights will guide the design of targeted experimental setups and establish the necessary conditions to control the chemical environment.

This chapter includes results already published or submitted in peer-reviewed journals:

- Merkens, S.*; De Salvo, G.*; Chuvilin, A. The effect of flow on radiolysis in liquid

phase TEM flow cells. *Nano Express* **2023**, *3* , 045006.

* Equally contributing authors. [6]

- De Salvo, G.; Merkens, S.; Korner, A.; Fritsch, B.; Hutzler, A; Malgaretti, P; Chuvilin, A. A workflow for modeling radiolysis in chemically, physically, and geometrically complex scenarios. *Manuscript under review at iScience.*

4.2. Non-Uniform Irradiation Modelling

Understanding how the radiolytic chemical recombination of species evolves into a steady-state concentration is crucial when diffusion is involved. The concentrations of species vary significantly due to the fluxes established at the *edge* of the beam irradiation in the liquid, a scenario commonly referred to as non-uniform irradiation. In this case, only a portion of the long, thin diffusive channel is irradiated, leading to high concentrations of radiolytic species in this region. Over time, species diffuse from the irradiated zone, gradually filling the non-irradiated parts of the channel during beam exposure.

Previous modelling studies that attempted to understand species diffusion across the channel focused on a closed liquid boundary.[23, 89, 93] This was a common assumption, as thin LCs are highly extended and it was believed that the boundaries should not affect the radiolysis dynamics.

Towards Open Boundary Conditions. The dynamics of species changes when liquid channels are connected to other functional reservoirs (e.g. bypass channels). These reservoirs, which are orders of magnitude larger than the LC, might influence radiolysis, and this will be explored in the context of novel boundary conditions applied in this work.

The development of diffusion models begins with the recognition that certain assumptions, such as treating the boundary as open or varying the diffusion path, may lead to important variations in the concentrations of species calculated within the beam area. The mathematical description of these boundaries generally falls into two categories: (1) closed boundaries where species cannot pass through, and (2) open boundaries, which allow species to diffuse

[6] This work is also discussed in Stefan Merkens' PhD thesis, *"Orchestrated Mass Transport for Quantitative LP-TEM"*, October 2023, presented as a compendium of articles and in full compliance with the rules of the University of the Basque Country.

into other channels or reservoirs. For example, an open boundary can be assumed when there is a significant change in scale, such as when a diffusive nano channel, the site of beam irradiation, expands into a micro channel "bypass" volume. In this case, species crossing the boundary are considered to no longer participate in the confined chemical system. This configuration is commonly referred to as the "bathtub" design.[7,8] With diffusion travel distances standardized at millimetres for silicon chip structures. The nanochannel may vary in novel designs, as developed by the research group,[120] where synergy between experimental and simulation efforts has led to the improvement of geometries with large bypasses integrated into the chip structure. These innovations reduce the distance travelled by diffusion across the nano channels, as illustrated in scheme 4.1c, allowing species to exit the imaging zone more quickly.

In contrast, spacers (Fig. 4.1b) or membrane patterns placed inside cells can act as barriers, leading to the accumulation of species and potentially reversing the direction of diffusion fluxes. Previously, the boundary was placed at a sufficient travel distance to avoid influencing the solutions, but this is changing in extremely confined geometries, such as micro wells structures [17, 94] or multiple nano channels systems with patterned SiN membranes.[119]

When convective transport is also considered, the flow regime in a thin nano channel corresponds to a laminar regime (see Section 3.3.5). In addition to the open and closed boundary conditions for mass transport, additional boundary conditions must be discussed, which will be covered later in Section 4.3.

[7]Protochips, "Introduction to Poseidon Select In Situ TEM Liquid Cell," YouTube video, 3:22, August 11, 2017, https://www.protochips.com/solutions/in-situ-tem-solutions/in-situ-liquid-cell/

[8]DENS solutions, "Ocean LPEM system - 'bathtub' design," YouTube video, 0:35, August 10, 2020, https://www.youtube.com/watch?v=LZKoEQ3GPXM&t

4.2.1. The Reaction-Diffusion Model

Geometrical Description. The description of a reaction-diffusion radiolysis model relies on the assumption that the concentration gradients, established from the beam outward, vary radially (2D) rather than isotropically in all dimensions (refer to Section 3.3.4). This is because the beam maintains a homogeneous energy/generation along the vertical direction (z-axis), assuming that the membranes (grey layers in Fig. 4.2a) are chemically inert.

A realistic geometry of a multi-scale liquid channel for both open and closed scenarios is shown in Fig. 4.2a, illustrating a coordinate shift at the nano channel site to exploit radial diffusion symmetry, originating from a stationary cylindrical beam at the origin (red volume in Fig. 4.2a), assumed for stationary TEM irradiation.

This approach enables the creation of a 1D finite element geometry (hence the name "1D model"), where the solution is calculated by shifting from Cartesian coordinates (x, y, z) to planar cylindrical coordinates r and θ, neglecting the z-axis for homogeneity, to define concentrations at $Q(r, \theta)$ within the nano channel (see Figs. 4.2a and 4.2b). Refer to Section 3.3.4 for details on the physical model implementation in such geometries.

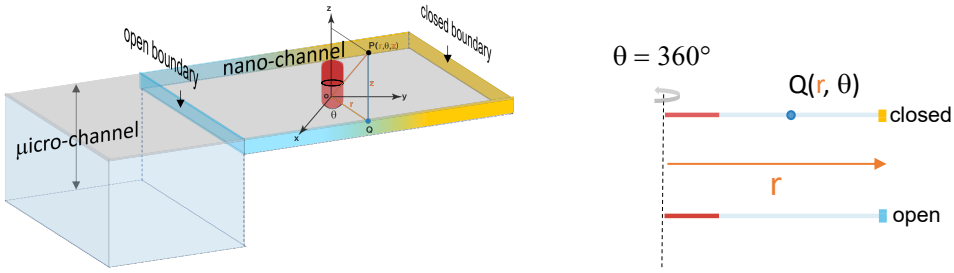

(a) **(b)**

Figure 4.2: Illustration of a 1D radiolysis reaction-diffusion model. **a)** shows a 3D section of a liquid cell with and without a bypass channel. The boundaries of the nano-channel are labelled to distinguish between the applied mathematical conditions (open or closed). The central volume (in red) represents the irradiated area, establishing a circular symmetry due to homogeneous generation along the z-axis. **b)** demonstrates that the same problem can be solved using a 1D geometry by exploiting radial symmetry along the r-axis, with a full circular symmetry ($\theta = 360°$) for calculating concentrations at $Q(r, \theta)$.

Model Validation. When implementing a space-dependent set of equations, it is essential to validate any extensions by comparing them with a reference model. In the following validation study, the model implemented by Schneider et al. is used to verify the correct implementation of the radiation chemistry.

1D models with radial symmetry (see Fig. 4.2b) are assessed under uniform irradiation, which means the entire width of the model is irradiated (beam generation term in Eq. 3.3, $R_i \neq 0$; only true for primary species). In such a scenario, diffusive fluxes are expected to drop to zero, since no spatial concentration gradients arise. Validation is carried out by overlaying the results of the 1D uniformly irradiated model with those of the 0D reference model [23] (see the legend in Fig. 4.3a) and a perfect match of the curves indicates successful model validation. This approach serves as the standard workflow throughout this thesis to evaluate the accuracy of kinetics equations when expanding chemical model into space-dependent implementations.

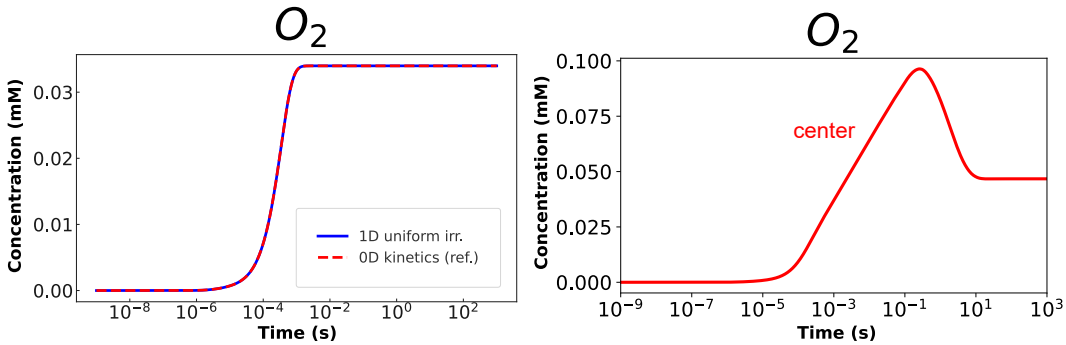

Figure 4.3: Validation procedure for diffusion: In **a**) the O_2 concentration under uniform irradiation in 1D models (COMSOL) (blue line) is compared to the 0D reaction kinetics model by Schneider (MATLAB) [23] (red dotted lines). Note the strong agreement between both ODE solvers. In **b**) the O_2 concentration at the center of a circular beam geometry (TEM) is evaluated under non-uniform irradiation conditions, with the generation term restricted to the beam area.

In a consecutive step, the geometric expansion was validated. Therefore, Schneider's previous implementation for non-uniform irradiation was reproduced, without access to the original code. Temporal changes in the concentrations of species, such as highly diffusive O_2, were visually compared and showed excellent agreement (compare Fig. 4.3b, to Fig. 3f of the reference [23]). Note the change in steady-state concentration due to interactions with the boundary in Fig. 4.3b, as compared to the case where species are generated uniformly (Fig. 4.3a).

4.3. The Reaction-Diffusion-Convection Models

Many LP-TEM setups allow fluid flow to be applied in the liquid cell.[91] From a modelling perspective, this requires the dimensional expansion of the geometry and coupling of the physics of reaction and diffusion with an additional convective term.

Model Description. As previously discussed, the beam is assumed to generate radiolytic species homogeneously in a cylinder. Thus, diffusive fluxes of radial symmetry evolve along the plane (x,y axis). On top of that, flow occurs unidirectionally, inside the diffusion plane but perpendicular to the beam direction. As a consequence, it disrupts the radial diffusion symmetry, which requires a complete 3D implementation. As shown in Figure 4.4, the nano channel of a liquid flow cell (LFC) surrounds the imaging volume, with *inlet* and *outlet* boundaries that allow unidirectional flow velocities. Laminar flow is the characteristic feature of nano channels in LP-TEM, which typically have a high aspect ratio, i.e., 50-500 nm in height and up to millimetres in widths. The *no-slip* flow conditions at the membranes (grey planes in Fig. 4.4) result in a parabolic velocity profile that varies along the z-direction, with v_{max} in the plane (x, y) = 0, where the electron beam (red volume in Fig. 4.4) irradiates the imaging area. The beam uniformly and continuously generates radiolysis in the centre of the liquid flow cell.

It is important to ensure the inlet and outlet are at an appropriate distance from the electron beam ($\pm\frac{w}{2}$) to avoid artefacts in concentration values caused by boundary conditions. Typically, millimetre-scale distances, as found in commercial flow setups, are used. The transport mechanisms and boundary equations implemented in these geometries are discussed in detail in the *Fluid Dynamics* section (Section 3.3.5).

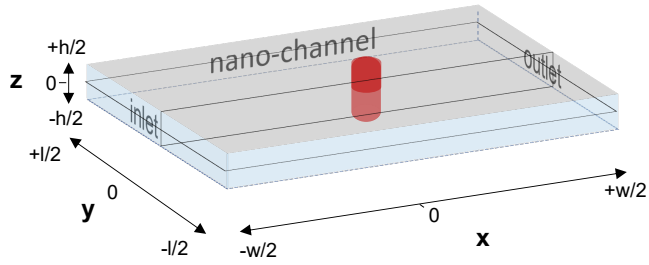

Figure 4.4: This schematic illustrates the geometry of a 3D reaction-convection-diffusion model. Reaction and diffusion are implemented similarly to the open conditions in diffusion models, while the new boundaries for convection include: laminar flow with no-slip conditions ($\overline{v} = 0$) at the membranes assumed rigid and chemically inert (gray plane), a specified mean flow velocity at the inlet, and reference pressure with fluxes enabled at the outlet.

Model Simplifications. Employing geometrical simplification significantly reduces the computational cost associated with fully resolving the complexities of a three-dimensional model. By simplifying the system to two-dimensional planar geometries, the number of variables and equations that need to be solved is substantially reduced, particularly in the context of the numerous reaction equations involved in radiolysis. Specifically, the *horizontal* (xy plane in Fig. 4.4) and *vertical* (xz plane in Fig. 4.4) planar geometries serve as effective approximations of the 3D system. These planes, indicated as black solid cut planes in Fig. 4.4, allow for focused analysis of the transport phenomena along specific axes of interest.

From the horizontal perspective, the flow maintained a steady, streamlined motion throughout the model, with a homogeneous velocity magnitude across all domains. In contrast, the vertical perspective captured the parabolic nature of the laminar flow, as previously explained in Section 3.3.5.

A quantitative assessment of the average concentration in flow models ($\overline{v} = 10^{-2}\,\mathrm{m/s}$, a reasonable parameter for LP-TEM) within the beam area was achieved through a direct comparison between 3D models and 2D simplified planar geometries. All three models lead to equivalent results, as demonstrated in Fig. 4.5a and b. Both 2D simplifications provide a valuable methodology for solving the problem.

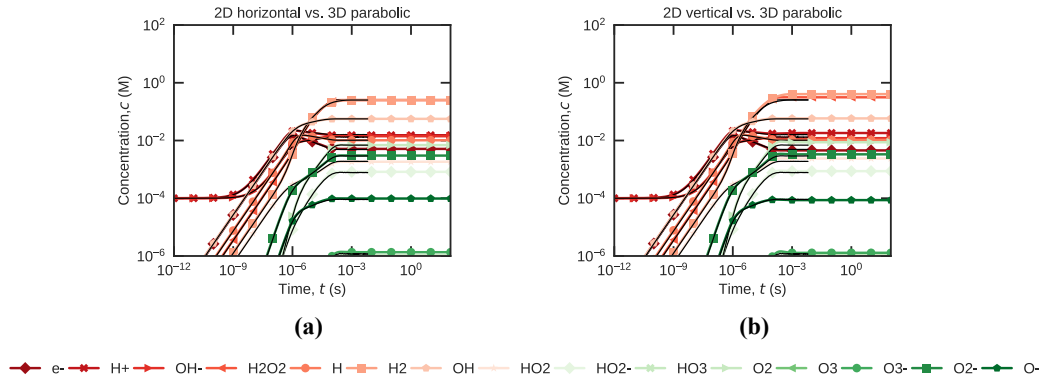

Figure 4.5: Comparison of the 3D full description of a reaction-convective-diffusion model (black lines) with the approximated geometries of 2D horizontal (left) and vertical (right) planar geometries. Primaries are depicted in shades of red, while secondaries are shown in shades of green. Note, the data is shown for a shorter time span to allow for reasonable computation of the 3D model.

The findings on radiolytic concentrations under the influence of flow are discussed in greater detail in the results section (see Section 4.5.4), where the data are contextualised in relation to the vertical model.

4.4. The Model Framework for LP-TEM Geometries

To simplify the problem of solving radiation reaction kinetics in geometrically complex scenarios and/or under the effect of additional mass transport mechanisms, it is crucial to streamline the modelling. For the finite element (FE) methodology, the most straightforward approach involves exploiting symmetries pertinent to the physical and geometrical problems of LP-TEM to simplify the model geometry. The resulting geometries, in all cases apart from GLCs which address the 0D case, represent high aspect ratio channels, that is, $AR = \frac{\simeq 10^{-5}\, m}{\sim 10^{-7}\, m} = 100$, with a cylindrical beam shape that emulates the homogeneous beam generation of radiolysis typical in TEM.

Figure 4.6 summarises a series of models that simplify the full 3D description (Figure 4.6f) of a liquid cell, allowing the analysis of the effect of *radial diffusion* and *vertical flow* on the concentration profiles of radiolytic species. These models, labelled with their respective dimensions and addressed physics, provide a framework of reliable and feasible geometries with a significantly reduced computational cost compared to a full 3D implementation.

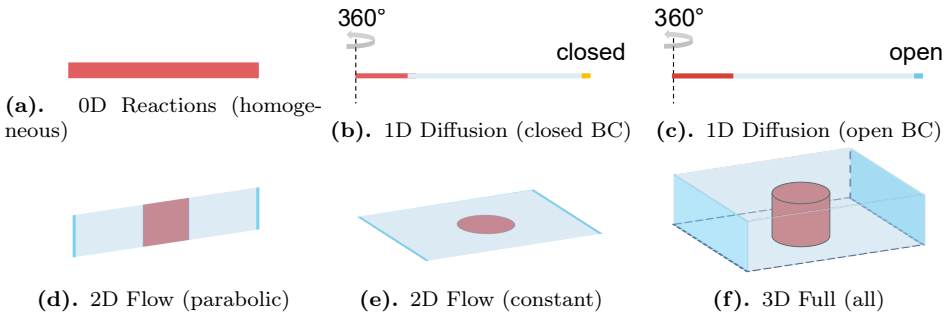

(a). 0D Reactions (homogeneous) **(b).** 1D Diffusion (closed BC) **(c).** 1D Diffusion (open BC)

(d). 2D Flow (parabolic) **(e).** 2D Flow (constant) **(f).** 3D Full (all)

Figure 4.6: The models used to replicate all radiolysis and transport scenarios are based on a validated and versatile framework. These models provide comprehensive simulations that account for both radiolytic product generation (beam area/volume in red) and transport mechanisms, including diffusion, convection, and reaction dynamics across all the geometry (red and light blue areas).

The validation of this framework was carried out across all dimensions, from 0D to 1D for diffusion (see Section 4.2.1) and from 2D to 3D for flow (see Section 4.3). Specifically, when calculating the diffusion models, the comparison with Schneider's first model [23] was sufficient.

Significant discrepancies arise when comparing average concentrations inside the irradiated area (IA) between these models, as shown in Figure 4.7.

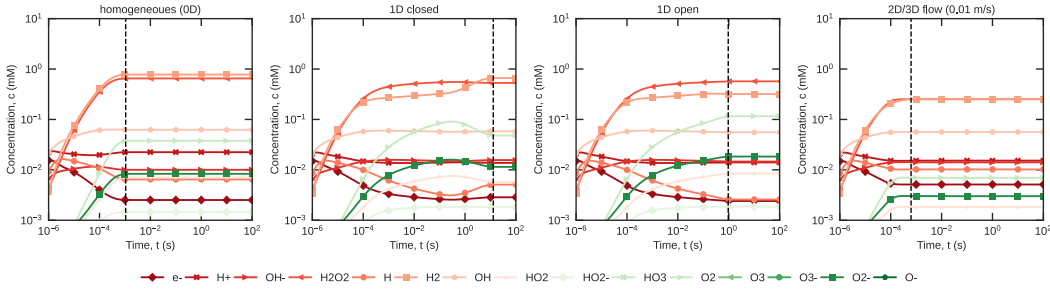

Figure 4.7: Average concentration over time in the IA for all the models presented in the framework. The temporal curves of 16 radiolytic species across time. The time when steady concentrations are reached is marked with a black dotted line.

Examining the temporal evolution shown in Figure 4.7, the species reach steady states at different times. Homogeneous irradiation stabilises in milliseconds, as previously predicted. [23] Closed cells partially stabilise around 0.1 s, depending on confinement, before entering a steady state due to the saturation of concentrations within the closed system, which is surprisingly similar across all LC configurations (discussed later in Section 4.5.1). In contrast, open systems maintain their steady state once stabilised. The time to reach steady state is closely related to the diffusion distances travelled from the irradiated area (see novel predictions in Section 4.5.1). Other 2D and 3D equivalent flow models reach steady state as quickly as, or even faster than, the homogeneous case. Benchmark predictions on flow effects [28] are summarised in Section 4.5.4.

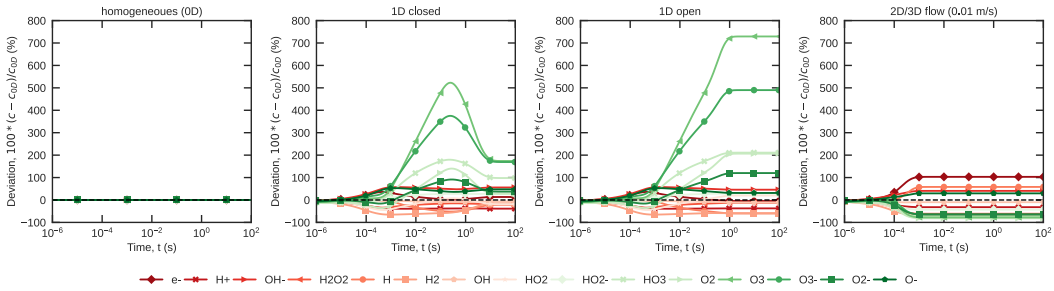

Figure 4.8: Concentration percentage deviations for all the models presented in this framework, with the 0D model as the reference. Note that secondary species, shown in green, appear to be the most affected by the model assumptions.

A comparison of all spatially dependent models against 0D reaction kinetic models highlights the importance of accurately solving the correct LP-TEM scenario. Figure 4.8 shows the deviations in species concentrations over time relative to the 0D case. Significant divergences occur, particularly for secondary products, which are less reactive and are more prone to diffuse. The most pronounced deviation is observed for O_2, with concentrations approximately 7-8 times higher when diffusion is considered, compared to the 0D model.

The here reported preview of the results, highlights the errors that may arise from using inadequate physics and boundary conditions considered. In the following sections, the discussion will focus on understanding why these particular discrepancies occur. A deeper analysis of spatial and temporal predictions will be performed linking the findings to experimental

contexts. This will not only address the quantitative differences, but also demonstrate the predictive potential of the models.

4.5. Radiolysis & Transport Predictions

The framework detailed in previous sections emphasizes the importance of selecting the appropriate model for specific scenarios. In the upcoming sections, spatial and temporal analyses of concentrations from diffusion and flow models will provide new insights into transient and steady states of radiolysis, as well as the local distribution of species across different experimental setups. The numerical analysis will also uncover previously unexplored effects of intrinsic (diffusion) and extrinsic (flow) transport due to edges and boundary on the radiolytic network. These findings offer valuable guidance for other researchers seeking to make accurate radiolysis predictions for their LP-TEM experiments.

4.5.1. Exploring Comparisons in Closed vs. Open Cells

Following the analysis of diffusion processes governing LC setups, data are examined using the 1D radial model in both configurations, open and closed boundaries (for geometrical description, refer to 4.2.1). To understand the extent of these changes, Figure 4.9 illustrates the steady-state spatial distributions of both stable and highly reactive species. Throughout this section, the local radial position will be denoted as r, with $r = 0$ representing the beam centre. The total width of the nano channel, where the boundary is applied, is referred to as w. The term "edge" is used to describe the sharp interface between the irradiated area (IA) and the surrounding liquid (located at r = 1 µm).

Figure 4.10 shows the temporal concentration profiles in the centre of the irradiated area (c_{IA}). The steady-state time observed for the radiolysis reaction products, compared to the homogeneous case 0D $\sim$ ms, increases. This is due to the relatively slow motion of species and is directly related to a diffusion time constant. For instance, for a nano channel width of $w = 50$ μm, the diffusion time constant $t_{diff,i}$ is on the order of seconds, as described by the mean square displacement in Equation 3.15. This time essentially represents the travel time for diffusive species to reach the boundary. Changing the boundary condition from closed to open has a significant impact on both spatial and temporal solutions.

The behaviour of four representative species is highlighted: e_h^- and $H^\bullet$ (Figures 4.9a,b and 4.10a,b) were chosen to represent highly reactive atomic intermediates, confined primarily within the irradiated area. Meanwhile, O_2 and H_2 (Figures 4.9c,d and 4.10c,d) represent stable, diffusive molecules that extend to the boundaries.

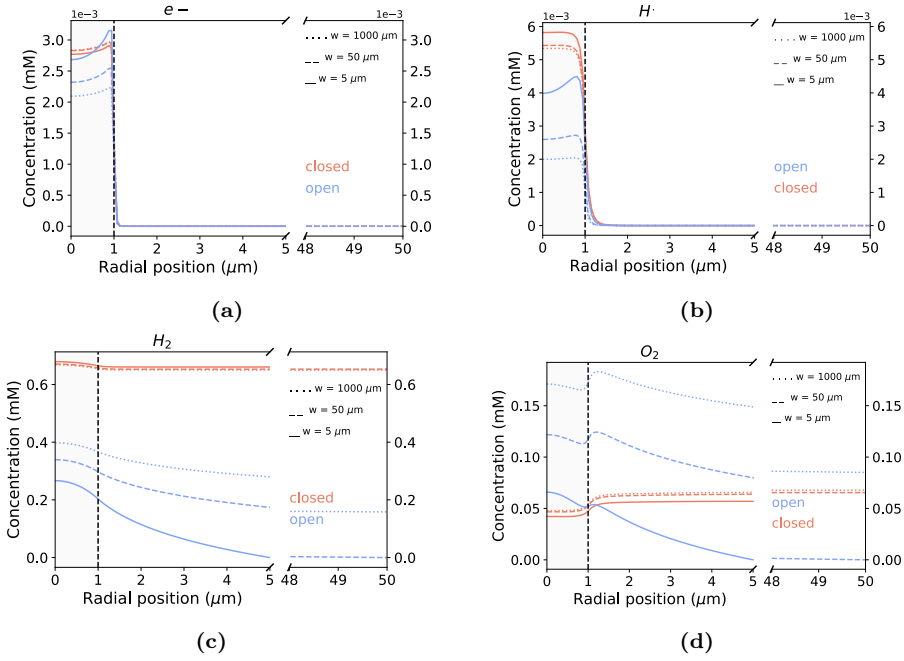

Figure 4.9: Spatial concentration profiles along nano channel widths of $w = 5\,\mu$m, $50\,\mu$m, and $1000\,\mu$m are shown for both permeable (open) and impermeable (closed) wall boundary conditions. The water is irradiated at $\psi = 7.5 \times 10^7$ Gy/s, consistent with the reference model for comparison [20]. The irradiation area is marked by the grey vertical span ($w = 1\,\mu$m).

The distinction between impermeable (closed) and permeable (open) boundary conditions is clearly depicted: the former are represented by *orange curves*, while the latter are shown with *light blue curves*. The profiles are presented for NCs of varying widths: $w = 5\,\mu$m, $50\,\mu$m, and $1000\,\mu$m. These widths were chosen to compare different experimental setups, including reservoirs with dimensions ranging from $5\,\mu$m to $20\,\mu$m, such as micro-wells [94, 17], technologically advanced MEMS chips with diffusion-enhanced properties with NCs ranging between $50\,\mu$m and $200\,\mu$m [120], and common setups featuring millimeter-sized NCs. The following general conclusions can be drawn:

- Reactive species exist only inside the IA, such as e_h^- and $H^\bullet$. Stable species react and

diffuse across the entire non-irradiated nano channel, such as H_2 and O_2.

- The time to reach the boundary for stable species increases with the width of the nano channel, scaling quadratically according to the mean square displacement law (Eq. 3.15). At that time, the open and closed model predictions start diverging toward different steady-state concentrations.

- Reactive species cannot diffuse and reach the boundary; however, they likely "feel" its effect through interactions with stable species (compare $H^{\bullet}$ in Fig. 4.9b and Fig. 4.10b).

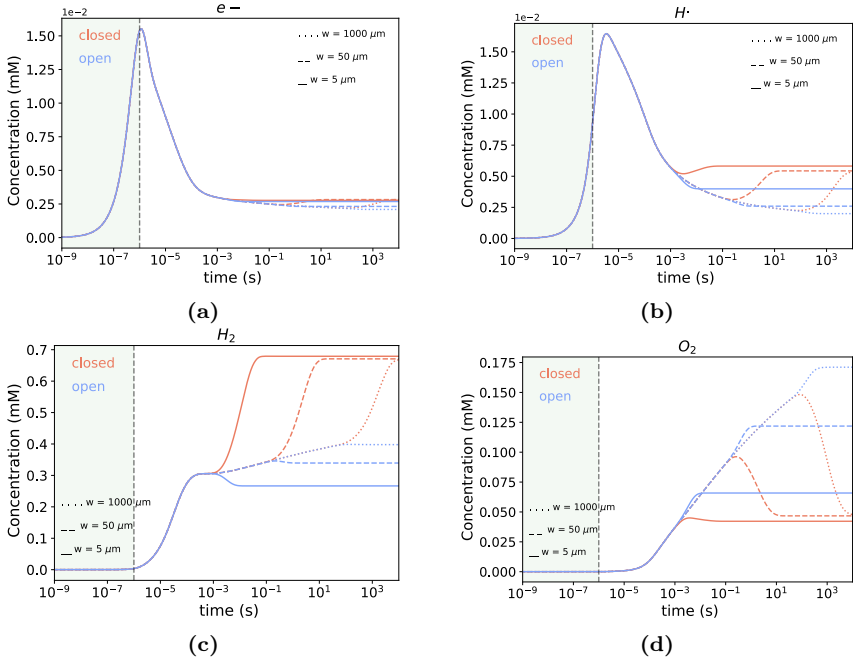

Figure 4.10: Temporal concentration evolution at the centre of the irradiated area, using the same NC widths, boundary conditions (BC), and irradiation dose (Ψ) as in Fig. 4.9. The initial time steps of the calculations were set to 10^{-12} seconds, allowing for refined concentration calculations of rapidly consumed species, such as e_h^- and $H^{\bullet}$ (curves within light green span), until reaching the onset of the homogeneous regime, indicated by the black dotted vertical line, to which the G-values apply.

4.5.2. Spatial Reaction Network Separation

Reactive Intermediates. The concentration of highly reactive species (that is, those with short lifetimes) such as hydrated electrons and H radicals should not be significantly

influenced by diffusion, as they have little time to diffuse away from the irradiated area where they are generated. Thus, one might expect minimal or no dependence of their concentrations on the boundary conditions of the model. However, Figures 4.9a and 4.9b clearly demonstrate the opposite. Furthermore, Figures 4.10a and 4.10b show that deviations begin to occur around 10^{-3} s, when the concentrations of long-lived species start to diverge (Fig. 4.10c and 4.10d).

This behaviour highlights the complexity of radiolysis phenomena, where a set of interconnected reactions takes place. Spatial separation of this reaction network can lead to non-trivial concentration changes. This observation underscores the need to account not only for the reactions involved but also for the mass transport processes that occur in real systems.

Let us now explore in more detail how diffusion perturbs the reaction set.

Stable Products. By performing a focused analysis of individual components within the coupled reaction diffusion equation - specifically diffusive flux $\mathbf{J_{i,r}}$ and the reaction rates $R_{\mathrm{reac},i}$—new insights into the behaviour of diffusive species can be discovered. Isolating the contribution of each term enables a meticulous understanding of how the local concentration gradient and reaction dynamics influence the overall evolution of the system. Figure 4.11 illustrates this approach for stable products. The coloured maps - orange (closed) and blue (open) - track the species from the moment they appear at the boundary until steady-state conditions are reached, with an NC width of $w = 50$ μm.

H_2 is a primary species with a beam generation rate of $R_{beam,\mathrm{H_2}} \simeq 1.3 \times 10^5\,\mathrm{mM/s}$. The sum of its reaction rates, excluding beam generation, shows the predominant consumption ($R_{cons,i} > R_{prod,i}$), as seen in the negative reaction rate plotted in Fig. 4.11h. The diffusive flux $\mathbf{J_i, r}$ is always positive, indicating outward diffusion at any point r and at any time (as shown in Fig. 4.11d). The overall rate (beam and reactions) remains positive along the NC, resulting in a build-up of H_2 until saturation is reached (see concentrations in Fig. 4.3a). The steady-state concentration of H_2 is lower under open conditions. This is because the increased outward diffusion (see Fig. 4.11e compared to Fig. 4.11d) more than compensates

for the reduced chemical consumption (Fig. 4.11i compared to Fig. 4.11h).

O_2 exhibits more complex behaviour. Figure 4.11, column 3, shows spatial maps of O_2 in a closed cell. In this setup, O_2 accumulates near the wall, but then rapidly decreases across the IA as the steady state approaches. The corresponding radial flux $\mathbf{J_{i,r}}$ indicates that, at this stage, the flux is directed inward toward the edge, driven by back-diffusion of O_2 from the wall (see the light-red curve in Fig. 4.11f). This inward flux, combined with high reactivity near the edge (Fig. 4.11l), leads to a steady-state concentration drop throughout the cell.

In the open scenario, the behaviour changes. Here, O_2 maintains a more consistent outward flux over time (see Fig. 4.11g), except near the edge, where similar edge effects appear. Interestingly, in the open channel, this outward flux helps to balance the overall decrease of O_2. The edge effects seem to have a strong impact on O_2 concentrations, but explaining them fully requires a segmented analysis of the reactions affecting O_2 specifically at the edge, which will be carried out in the next paragraph.

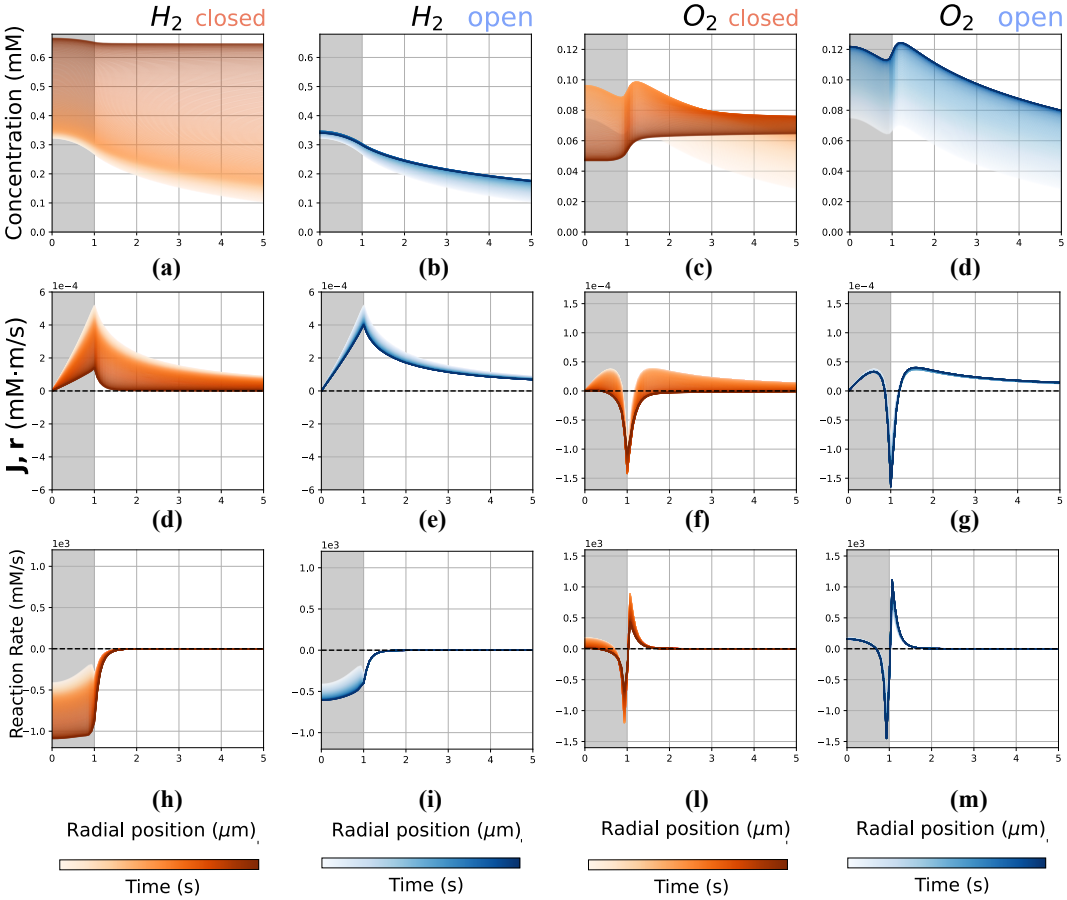

Figure 4.11: Spatial profiles from the centre (c_{IA}) to $r = 5\,\mu$m for a total channel width of $w = 50\,\mu$m, and temporal profiles showing the evolution from the time species reach the channel wall to steady-state, as indicated by the time colour bar.

Oxygen Reactivity at the Edge. The last observation highlights that the edge region has a unique reactivity for oxygen. Concretely, there is an abrupt switch in the reaction rate: oxygen undergoes intense consumption right before the edge, but this quickly switches to production just beyond it (around $r = 1\,\mu$m) in both open and closed cases (see Figures 4.11 l and m). In other words, diffusion effects create zones within the cell where different reactions dominate. These reactions are reflected seamlessly in the concentration profile of O_2 (see Figures 4.11c and d). Note that O_2 is not directly produced by the e^- beam.

Oxygen consumption occurs mainly through reactions #23 and #37 with e_h^- and $H^\bullet$,

respectively, and production through reaction #42 and #43 from $OH^{\bullet}$, $HO_2{}^{\bullet}$, and $O_2{}^{-}$:

$$23 : e_h{}^{-} + O_2 \rightarrow O_2{}^{-}$$

$$37 : H + O_2 \rightarrow HO_2{}^{\bullet}$$

$$42 : OH^{\bullet} + HO_2{}^{\bullet} \rightarrow H_2O + O_2$$

$$43 : OH^{\bullet} + O_2{}^{-} \rightarrow OH^{-} + O_2$$

Find all the chemical equations in Appendix A.2.

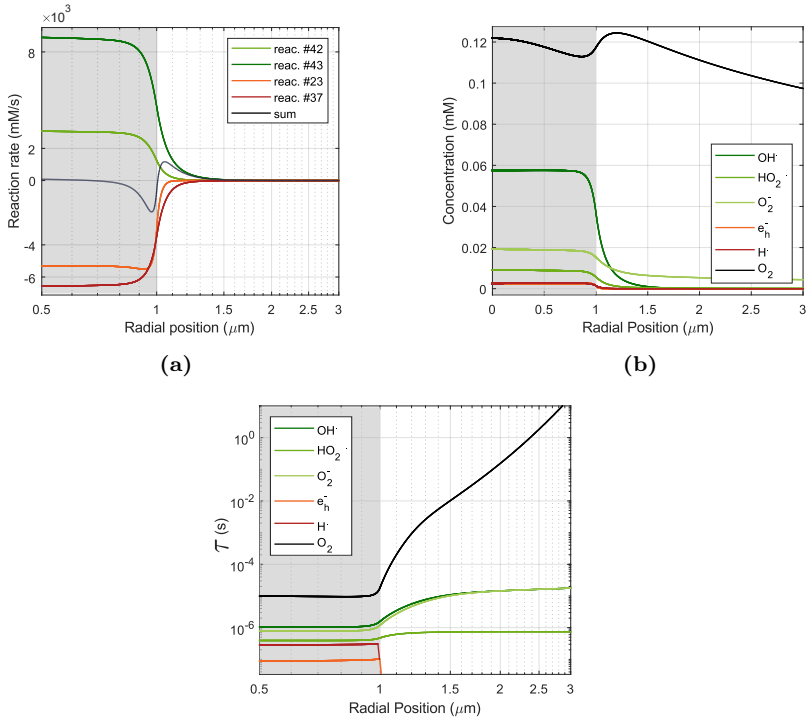

Figure 4.12: Oxygen reactivity segmented analysis focused on the edge of the irradiated area (*gray background*). **a)** shows prominent production reaction rates (*green shaded lines*) and consumption reactions (*red shaded lines*) for oxygen, with their sum represented by the *black line*. Comparisons of the **b)** spatial concentration profiles and the **c)** species lifetime involved in the subset of oxygen reactions along the radial axis of NC are also illustrated. The colour scheme for the curves is consistent with that in a).

To show that this subset is the main responsible for edge effects, Figure 4.12a shows the reaction rates along the radial profile and their sum in steady state under open diffusion conditions. Examining the sum of these rates for O_2 reactions reveals a sinusoidal pattern

centred at the edge ($r = 1\,\mu$m, black curve), which is also observed in O_2 edge concentrations. Therefore, the reactions highlighted in *red* (for consumption) and *green* (for production) are the primary cause of this effect.

Within the IA, these reactions are balanced, resulting in a net zero reaction rate for O_2. However, as we approach the edge, this balance is disrupted, leading to a marked over-consumption of O_2. This over-consumption is driven by reactions #23 and #37, which involve $e_h{}^-$ and $H^\bullet$ (highlighted in red in Fig. 4.12a). Beyond the edge, the influence of beam generation stops, creating an environment in which more diffusive species, such as $OH^\bullet$, $HO_2{}^\bullet$, and $O_2{}^-$, drive reactions #42 and #43, favouring the production of O_2. This switch occurs because diffusive species that promote O_2 production reach the outside of the IA than the radicals that consume O_2, creating a distinct separation in the reaction network between the irradiated and non-irradiated regions (see concentration profiles in Fig. 4.12b).

This phenomenon can be better visualised by also analysing the *lifetimes* τ of the species, which provide an estimation of when a species is completely consumed (see Section 3.5.2). Lifetimes along the radial position are illustrated in Figure 4.12c. Species involved in production ($OH^\bullet$, $HO_2{}^\bullet$, and $O_2{}^-$) have a lifetime of the order of microseconds within the irradiated region, which increases further beyond the edge. Species responsible for the consumption, such as $e_h{}^-$ and $H^\bullet$, experience lifetimes that are orders of magnitude shorter, so they do not exist outside the IA. Finally, O_2 is the species that exhibits a continuous increase in its lifetime as it moves farther away from the edge. This is because of the decreasing probability that it will be consumed.

The "reaction network separation" is an important phenomenon resulting from the interplay between mass transport and reactivity in heterogeneously irradiated scenarios. It will now be considered as a novel concept when non-linear behaviour in species concentration is observed (e.g., the oxygen profile at the edge) due to spatial perturbations in the network (including effects like diffusion, convection or drift electrochemical currents).

4.5.3. Practical Implications for Experiments

The spatial separation of species, as discussed earlier, causes changes in the reaction network and is closely related to the diffusion of these species. When certain long-lived and diffusive species (i.e., molecular stable species) have an enhanced chemical affinity and act as *scavengers* for short-lived species (i.e., atomic reactive species), factors such as liquid cell widths, boundary conditions, and irradiation edges affect the reaction network particularly. By engineering the liquid cell, additional control can be gained over the radiolysis reaction network.

Effect of Nano-Channel Width. This capacity of control is demonstrated by the steady-state concentrations (c_{ss}) reached at different nano-channel (NC) widths, as shown in Figure 4.13. The graphs show c_{ss} of e_h^- and $H^\bullet$ for which O_2 acts as scavenger (reactions #23 and #37; Appendix A.2. In open cells, the effects of these reactions are amplified when the concentration of O_2 varies. This is evident from the reduced concentrations of e_h^- and $H^\bullet$ (shown in *light blue*) in Figures 4.13a and 4.13b, compared to the increase observed for O_2 in Figure 4.13c. However, this increased scavenging potential also raises the tendency to form a *gaseous* phase inside the cell, making tunable widths useful for specific experimental purposes.[120] On the other hand, the effects of the NC width on the reactions mentioned above are less pronounced in closed setups. Radicals become more prevalent because the concentration of O_2 remains low, as demonstrated by the *orange* lines in Figure 4.13.

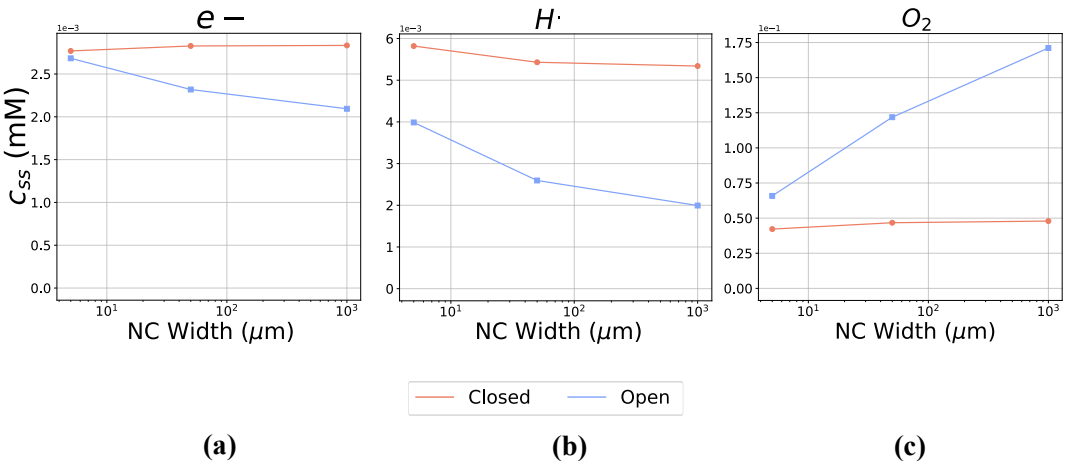

Figure 4.13: Steady-state concentrations of radiolysis species at the centre (c_{ss}) of the beam are shown for various liquid cell configurations and across different NC widths (data extracted from Fig. 4.9). Reactive-scavenger pairs are represented in **a)** e_h^-, **b)** $H^\bullet$, and **c)** O_2, respectively. The legends at the bottom indicate the colour scheme for the different boundary conditions.

Advancements in Setup Optimisation. As shown by the steady results in Figure 4.13, it is difficult to improve the radiolysis-related properties in closed cell settings. This is because the reactive pairs of scavengers do not respond much to changes in the width of the setup (see the *orange* data points in Fig. 4.13). In contrast, open setups show a noticeable difference in this behaviour.

Using this understanding, we developed the *diffusion cell* [28]. This innovative design features diffusion islands with NC widths of approximately 50 μm, surrounded by bypass channels integrated directly onto the Si frame (see Fig. 4.1c for the real design). This new geometry exhibits improved radiolysis properties due to the higher rate of removal of accumulated species at the open boundary of the NC (see Fig. 4.2b for the model representation). In summary, liquid cells with reduced lateral extension (NC width) offer two key advantages: they reduce *reactive species* through scavenging (see concentrations of e_h^- and $H^\bullet$ in Fig. 4.13) and reach steady-state conditions faster. Using shorter open channels, the design significantly reduces the diffusion travel time of species and thus facilitates their removal from the IA (compare the temporal curves for open setups in Fig. 4.9c and Fig. 4.9d). This stabilisation minimises the effects of the beam and prevents further increases in the concentration of reactive species. With this dual benefit, the importance of reducing the

dimensions of nano channels has become clear, highlighting their crucial role in controlling radiolysis.

Effect of Dose Rate. The dose rate was previously reported as a crucial parameter affecting steady-state concentration.[23] However, the modelling approaches were limited to 0D scenarios. The models introduced above allow one to evaluate the effect of the dose rate in non-uniform irradiated models under different boundary conditions. When examining species concentrations across different setups (Fig. 4.13), are observed distinct steady-states. In closed systems, diffusion outflow of species is contained, which can potentially lead to the same steady-state concentrations because mass is conserved. In contrast, open systems have a dynamic and variable reaction network, with c_{ss} influenced by the continuous exchange of matter. The hypothesis is that this variability can also depend on the dose rate and setup combination, i.e. the amount of matter injected into the system in a certain volume.

To test this hypothesis, dose sweep calculations were performed by increasing the dose (ψ) parameter, for 1D open and 1D closed models. To explore the effects of varying dose, the beam current was adjusted from 0.1 nA to an extreme value of 100 nA under continuous TEM irradiation. This allowed a dose rate that covers a range from $\sim$ 10^7 Gy/s to $\sim$ 10^{10} Gy/s, which corresponds to electron fluxes ranging from 200 $\frac{e^-}{nm^2 \cdot s}$ to 2×10^5 $\frac{e^-}{nm^2 \cdot s}$.

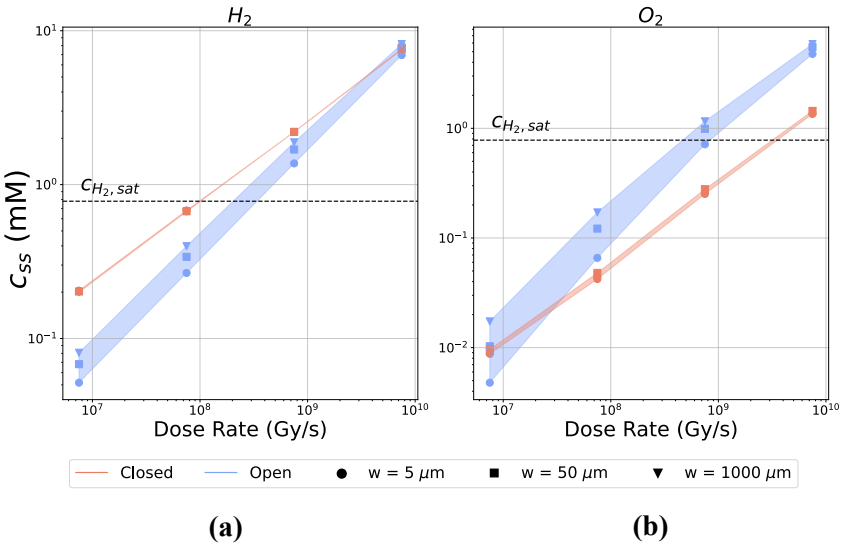

Figure 4.14: a Steady-state concentrations of **a)** H_2 and **b)** O_2 under increasing beam dose rates are shown. The marker style distinguishes between different types of liquid cell widths: common open NC (1 mm, triangle), the *diffusion cell* with NC width of 50 μm, square), and 'ideal' micro-sized NC (5 μm, circle). A background colour indicates the steady states for closed setups in *orange* and for open setups in *blue*, highlighting the differences between NC widths.

In Figures 4.14a and b, steady-state concentrations in the IA for H_2 and O_2 are depicted, showing the expected increase in concentration with respect to dose rate. This trend aligns well with the reaction kinetics, as detailed in the reference calculations by Schneider et al.[23]

The hypothesis is confirmed: In closed setups, varying the widths has no significant impact, as the system consistently returns to the same steady state, reflected by the uniformity of the orange markers and background in Fig. 4.14a. However, in open systems, a striking difference appears due to variations in diffusion travel time, illustrated by the blue span between the data markers for H_2 and O_2 on a log scale, in Fig. 4.14b. In particular, as the dose rate increases (Figure 4.14a), the difference for H_2 between the closed and open configurations decreases. This is because H_2 is strongly dependent on beam generation, and at high dose rates, diffusion cannot effectively remove this species. In contrast, O_2 being secondarily produced exhibit a pronounced divergence between closed and open setups, driven by its scavenging reactivity in the IA that is influenced by boundary conditions (Figure 4.14b).

Controlling the Gas Production. So far, much attention has been paid to the effect of diffusing products in the context of scavenging, while less attention has been paid to the accumulation of H_2 due to its diffusion properties, as it is a less reactive molecule. One of the most recent challenges that has been discussed in LP-TEM is to control bubble gas formation, prevalently generated from molecular hydrogen during experiments,[26] or, in some cases, to control its growth (e.g., induced bubble growth in electrochemical experiments). To establish principles for addressing this issue, a deep look at simulations is necessary for predictions.

The first suggestion is to work with a low dose to avoid hydrogen formation [19] and prevent bubbles, which were observed to form when concentrations greatly exceed the saturation concentration ($c_{H_2,sat}$ = 0.78 mM at a pressure of p = 100 kPa).[26] The beam dose rate is the crucial parameter in determining the amount of species generated within a certain volume, thus likely influencing whether bubbles would appear (see dose dependence of H_2 in Fig. 4.14). The liquid cell configuration impacts the timing of effects, such as bubble generation, and when they start to be observed, whether in a closed or open configuration (refer to concentration temporal curves in Fig. 4.9c and 4.9d).

One of the most comprehensive analyses of bubble formation in LP-TEM[26] has explicitly shown that bubble formation occurs in TEM mode in a closed cell [124] in tens of seconds under beam conditions equivalent to a moderate dose in TEM ($\sim 10^8$ Gy/s). In practice, systems above this dose rate and with closed diffusion properties will repeatedly produce gas bubbles, as shown by the threshold $c_{H_2,sat}$ in Figure 4.14. However, this can be avoided with an open setup that, at the same dose, shows less H_2 (Fig. 4.14). The phenomenon of gas phase production can also be mitigated at higher doses by using open systems. As highlighted by the results shown in Fig. 4.14 for open systems, the steady-state concentration varies for different NC widths even at the same dose rate. Lower H_2 concentrations are achieved by decreasing the NC size. Other species that can convert to the gas phase, such as O_2, are produced in larger quantities under open conditions. O_2 most likely contributes to bubble enlargement; however, this depends on whether the saturation of hydrogen concentration is reached. O_2 alone is less likely to produce bubbles due to its lower steady-state concentrations and higher solubility compared to H_2.

4.5.4. Effect of Flow on Species Concentrations

As described in 4.3, a convective transport was successfully implemented in the models. Flow has been considered in many publications [122, 123] as a potential means of overcoming the consequences of radiolysis on the processes under observation, as well as a tool for mixing reagents in LP-TEM nanoreactors.[122, 116] Thus, the coupling of convective transport to chemical reactions and diffusive transport in one model was highly requested to deepen the understanding. This section summarises the results that were published in Nano Express.[28] Radiolysis scenarios without flow (i.e. those governed purely by diffusion, as discussed in the previous paragraphs) are compared to cases with a moderate or high unidirectional velocity field, revealing its impact on the overall transport dynamics.

Figures 4.15a and 4.15b present the steady-state concentration field, from the 2D vertical modelling (refer to 4.3 *Model Validation* for the sufficiency of 2D simulations in this flow context), for the same four species analysed in 1D radial geometries (compare to Section 4.5.1): molecular H_2 and O_2, and the more reactive products $H^\bullet$ and hydrated electrons ($e_h{}^-$). The hydrogen concentration (Figure 4.15a) decreases significantly with increasing flow velocity, indicating efficient removal from the irradiated area (IA) at moderate flow velocities ($\overline{v} \geq 10^{-3}\, m/s$). Similarly, molecular oxygen (Figure 4.15a) drops to nearly zero concentration even at lower flow velocities.

In contrast, atomic H and hydrated electrons ($e_h{}^-$) (Figure 4.15b) show substantial increases in concentration within the IA at moderate flow velocities ($10^{-5} - 10^{-2}\ m/s$), only beginning to rinse effectively above approximately $0.25\, m/s$.

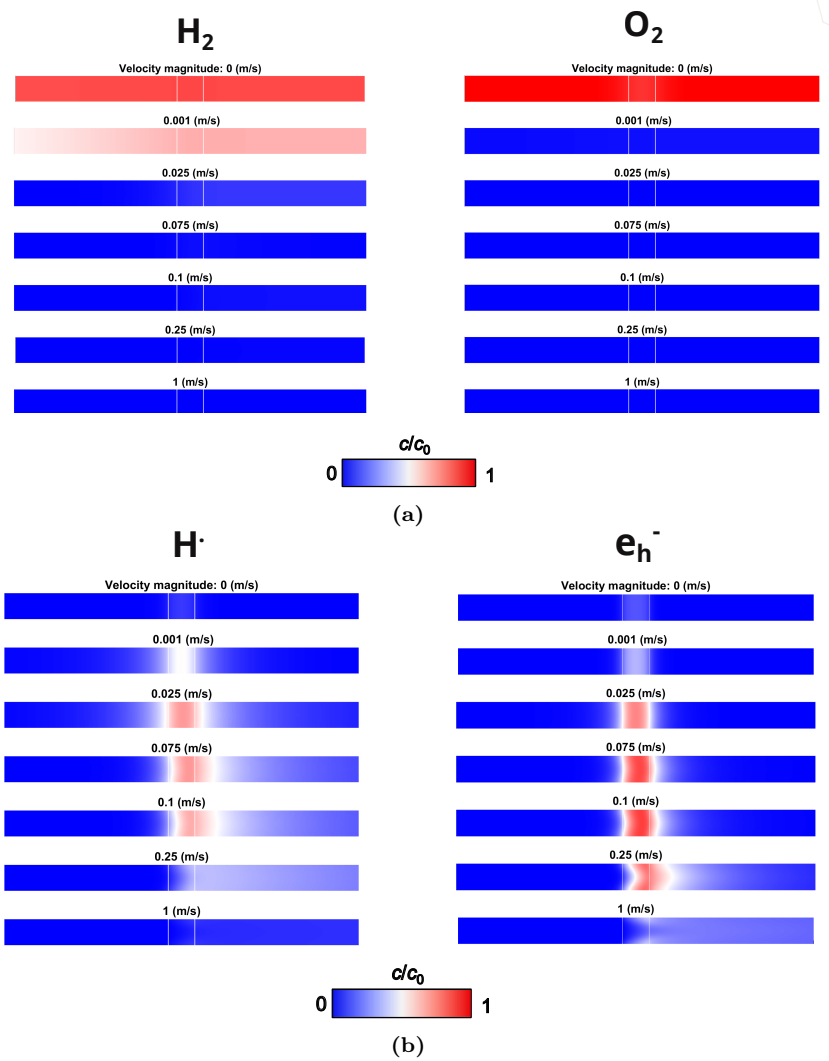

Figure 4.15: Stationary 2D concentration fields of selected radiolytic species at representative flow velocities: **a)** molecular H_2 and O_2, and **b)** radical $e_h{}^-$ and atomic $H^\bullet$. The total width of the snapshots is 2 μm, and the irradiated area (IA), depicted as a white contoured box in the center, is 150 nm in width.

Figures 4.16a and 4.16b represent the mean concentrations ($\bar{c}_{ss}$) for the entire set of species within the irradiation area (IA) for flow velocities up to 1 m/s. Figure 4.16a presents the raw averaged concentrations, while 4.16b shows the normalised concentrations relative to their values at zero flow ($\bar{c}_{ss}/\bar{c}_{ss,(v=0)}$). Primary species are colour-coded in shades of red, and secondary species are depicted in shades of green. A significant increase in concentration is observed for three species: atomic hydrogen (H), hydrated electrons ($e_h{}^-$), protons (H^+) (see

Fig. 4.16b). Among these, atomic H and hydrated electrons show concentration changes that begin at flow velocities of 10^{-5} m/s. All species showing significant concentration increases are primary species with non-zero G-values (*red shades*), while secondaries undergo a monotonic decrease (*green shades*).

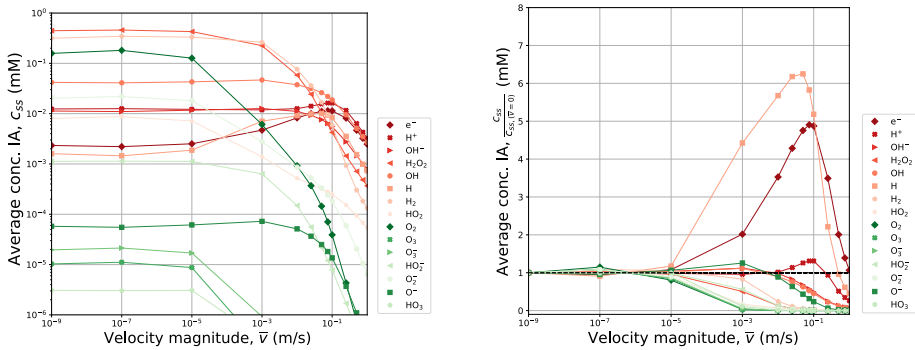

(a) **(b)**

Figure 4.16: Average concentrations of radiolytic species in the IA as a function of flow velocity. Data points shown at $10^{-9}\,m/s$ on a log-scale corresponds to actual zero-flow simulations **a)** shows the temporal evolution of species at steady-state concentrations, c_{ss}, and **b)** presents the concentrations normalised to zero-flow conditions, $c_{ss}/c_{ss,v=0}$.

Reactivity at Moderate Flow Velocities ($10^{-5} - 10^{-2}\ m/s$). Chemical reactions, which in the absence of flow would occur at the same location within the irradiated region (i.e., in the IA), are dispersed along the channel when flow is applied. However, flow dominates over the species, depending on their reactivity within the IA. The species more affected by displacement from the IA are stable molecular products, which are long-lived species. The concentration of H_2O_2 and O_2 drops dramatically at flow velocities as low as 10^{-5} m/s (see Figure 4.16a), and these species are flushed away to the outlet of the liquid flow cell, preventing their *scavenging* efficiency. This leads to a substantial suppression of reactions #36, #37, #20, and #23 (see Appendix A.1 for the reactions formulas), which were found responsible for the resulting increased concentrations of $H^{\bullet}$ and $e_h{}^-$ in the IA under moderate flow conditions.

Under conditions of moderate flow rates, the steady state of the reaction network changes significantly compared to scenarios with zero flow. Thus, the concept introduced in Section 4.5.2, referred to as "spatial reaction network separation", becomes even more prominent.

In this context, flow plays a critical role: molecular stable species are efficiently carried away by flow and eventually react downstream, while reactive intermediates remain in the IA, where they are overproduced due to the absence of their scavengers.

Reactivity at High Flow Velocities ($\overline{v} \geq 10^{-1}\ m/s$). As flow velocities increase, the hypothesis of completely refreshing the solution by flushing away radiolytic species takes centre stage. All concentrations were shown to begin to decrease inside the IA at flow velocities greater than 10^{-1} m/s (Figure 4.16a). This scenario suggests species are travelling while the solution flows along the channel, and eventually react further downstream from the IA.

For better understanding, it is essential to examine how long species remain inside the IA in relationship to flow. This can be achieved by comparing the lifetime (τ) of the species with the travel time (Δt) of the liquid through the IA, both concepts were introduced in Section 4.5.2. The lateral axis of the channel ($\Delta x = w_{\mathrm{IA}}$) is related to the travel time by the relationship $\Delta t = \frac{W_{\mathrm{IA}}}{\overline{v}}$. While τ is obtained from concentrations averaged over the IA divided by the sum of the consumption reaction rates, everything is in steady state. If $\tau_i > \Delta t$, the species has sufficient time to be rinsed from the IA and participate in the downstream reaction network. In contrast, if $\tau_i < \Delta t$, the species will react within the IA.

Figure 4.17 illustrates the lifetimes (τ_i) derived for all species compared to the travel time of the solution (Δt) through the IA. For all species, the lifetime begins to exceed the travel time from flow velocities bigger than 0.1 m/s (see the cross point of *black dotted diagonal line* in Figure 4.17).

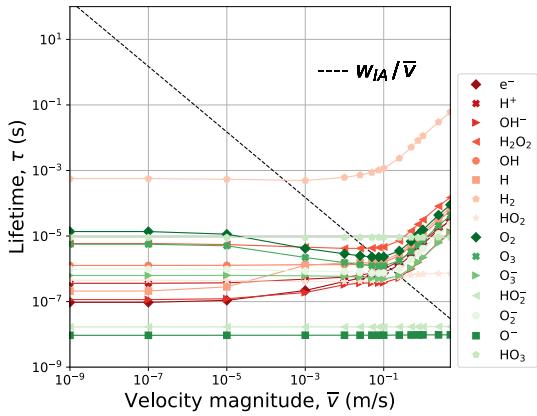

Figure 4.17: Comparison of the average lifetime, τ, with the travel time of the flow through the IA.

This analysis confirms that at the highest flow velocities ($\overline{v} \geq 10^{-1}$ m/s), the reaction network is rather "suppressed" or displaced outside the IA. While inside, the solvent is efficiently replenished, removing all radiolysis products and maintaining a pristine environment. Figure 4.17 highlights the species that have longer lifetimes and, therefore, are more easily rinsed out of the IA. This provides information on which species are preferentially removed by the flow and no longer participate in the reaction network, such as H_2O_2, O_2, O_3, and H_2. In the next paragraph, a study on the scavenging selectivity will be performed to better understand the potential of using flow for scavenging.

Scavenging Selectivity with Aerated Water. Simulations were carried out to investigate scavenging by flowing aerated water with dissolved O_2 at a steady-state concentration of 0.18 mM, established from the initial simulation at zero flow. Figure 4.18 illustrates the steady-state concentrations of O_2, $H^\bullet$ and ${e_h}^-$ under the same flow conditions (refer to Figures 4.15a and 4.15b for comparison, with the same colour range). The presence of O_2 in the water leads to an almost complete suppression of the increase in $H^\bullet$ concentration and ${e_h}^-$ either. Furthermore, a noticeable decrease in O_2 concentration is observed downstream as water passes through the IA, indicating O_2 consumption exclusively within the IA. Even at a high rate of scavenging (1 m/s), the activity seems equally effective as at zero flow (diffusion case).

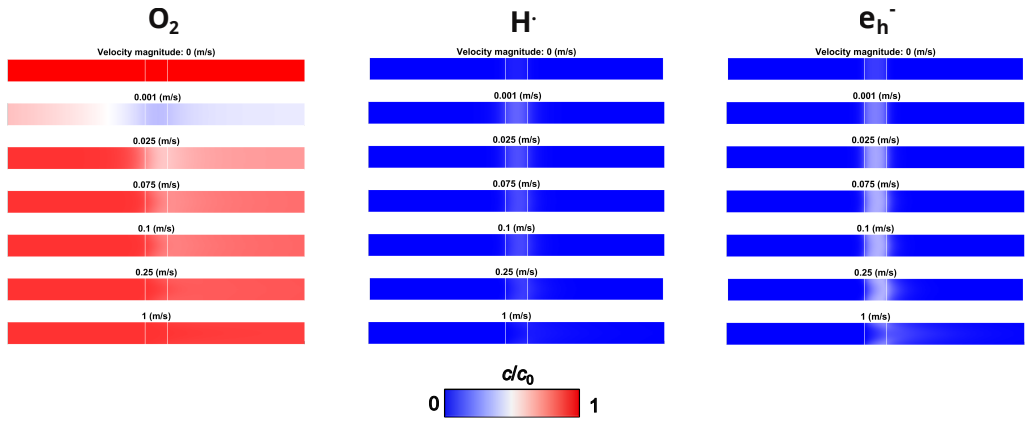

Figure 4.18: Stationary 2D concentration fields of O_2, e_h^- and $H^\bullet$ at representative velocities of the flow of aereated water with 0.18 mM of dissolved O_2. The total width of the snapshots is 2 μm, and the irradiated area (IA), depicted as a white contoured box in the center, is 150 nm in width.

It is important to note that scavenging is a selective process and thus cannot be applied in a more general manner. As a consequence, the reduction in $H^\bullet$ and e_h^- concentrations due to the flow of O_2 - saturated water is counterbalanced by an increase in the concentrations of H^+, HO_2, and O_2^-. These findings were detailed in the manuscript with respect to the entire radiolysis set of species.[28]

Practice of Flow Effects in LP-TEM Experiments. From the simulations combining flow and radiolysis, a complex but insightful behaviour of reactive species was observed. These simulations reveal that implementing flow in experiments is complex and not as straightforward as it may seem. However, the results offer helpful guidelines for conducting quantitative flow experiments. As illustrated by the concentrations in Figure 4.16a and the lifetimes to zero concentration of species in Figure 4.17, the concept of "sweeping away" radiolytic species apparently works at mean velocities higher than 0.1 m/s. However, no existing setup could achieve such high velocities, as revealed by CFD simulations and experiments reported earlier.[91, 125]

If high flow velocities cannot be reached for various reasons, such as membrane rupture, bulging, or designs that promote diffusion,[91] lower velocities ($10^{-5} - 10^{-2}$ m/s) are possible and have been verified.[116, 126] Also, in experiments, the sample is commonly attached at the solid-liquid interface (SiN membranes or electrodes), where the smallest velocities due

to laminar flow are observed. [126] As a result, radicals tend to increase at these lower velocities (see Fig. 4.16a) due to spatial disturbances in the network, making scavenging the most effective strategy to mitigate their reactivity.

With regard to the potential of flow to supply scavengers, the situation is different. Previous simulations on diffusion showed that the self-scavenging properties of species such as O_2, which depend crucially on the width of the nano channel (see data in Fig. 4.13), vanish when flow is applied, as O_2 is flushed away. Inflowing aqueous solutions O_2 have been shown to prevent the accumulation of some species. For example, O_2 saturated at 1 bar ($1.22\ mM$) leads to an approximate 5-fold decrease in e_h^- and $H^\bullet$ concentrations, while it can systematically increase other reactants. Thus, under these conditions, flow is not a universal solution. However, the effects of more targeted reagents or solvents can be tested and quantified using 2D flow simulations, with reaction kinetic models already implemented for radiolysis mitigation.[84]

CHAPTER 5

PREDICTIVE SCANNING TEM MODELLING

5.1. Introduction

In Chapter 4, the exploration of radiolysis models under continuous TEM provided valuable insight into the behaviour of radiolytic species generated by a stationary and uniform irradiation condition. The analysis takes a complex turn when considering the dynamic irradiation of a scanning mode of imaging (STEM).

Remarks on STEM Illumination. A comparison of beam illuminations is illustrated in Figs. 5.1a and b. The electron beam covers a wide area on the micrometre scale for TEM. For STEM, it represents the nanometre-sized scanning probe.[127] The time scale for a STEM frame is determined by the dwell time, which represents the time the electron beam spends in a position. The resolution of the image is governed by the magnification, which dictates the spacing between probe positions (defined from centre to centre) and defines the pixel size (square area surrounding the beam). The dwell time directly influences the imaging speed, magnification controls the level of detail captured in the frame, establishing a balance between temporal and spatial resolution.[127]

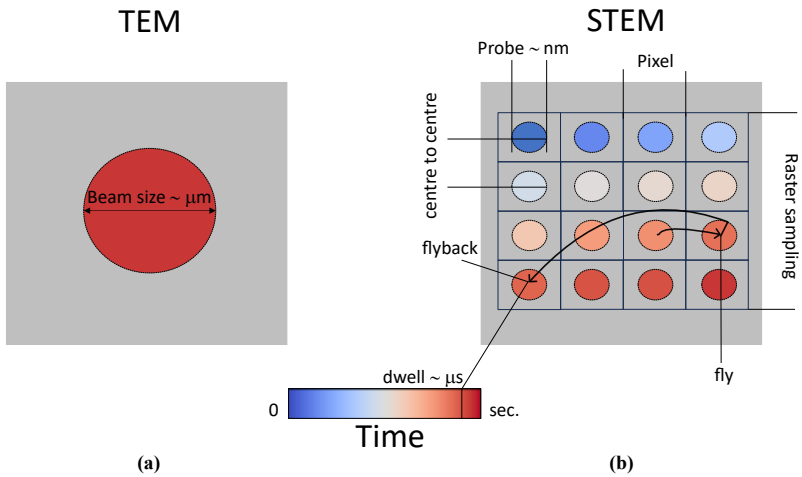

Figure 5.1: Representation of an image acquisition under sampling conditions of **(a)** TEM and **(b)** STEM mode, pointing out the different space and time of irradiation.

The fundamental resolution element is the pixel, a square region whose size is determined by the number of scan points distributed over the image frame. Typically, STEM images consist of arrays that comprise thousands of pixels per axis. The size of the pixels is inversely proportional to the number of pixels that cover the scanned area, directly influencing the resolution of the final dataset. For high-resolution STEM imaging, magnifications can reach 10^7, allowing the resolution of atomic-scale features.[128]

Scanning processes are traditionally performed using a raster sampling scheme, in which the beam sequentially scans each pixel by rapidly moving from position to position along a line, followed by a "flyback" motion to return to the starting position of the next line.[129] This spatial pattern results in varying scan speeds—fast within a line and slow between lines—leading to non-uniform damage throughout the sample.[130] Such effects can be directly observed in STEM, influencing radiation chemistry while imaging under different operational conditions.[93]

Difference in Dose Deposition. One of the big challenges in quantifying damage in STEM is the scaling of the electron flux, which is inversely and quadratically correlated with the size of the beam. For common magnifications, the STEM probe is approximately 1000 times smaller in diameter than the TEM probe. This scaling enhances the local electron dose absorbed by the sample, making it potentially higher by several orders of magnitude compared to TEM. In practical terms, while TEM typically operates with beam currents in the nanoampere range, resulting in electron fluxes around 10^3 e^- nm^{-2} s^{-1}, STEM employs picoampere currents that can achieve doses as high as 10^8 e^- nm^{-2} s^{-1} (see Eq. 3.10). Many studies involving scanning mode assume that the electron dose is uniformly distributed across the total area of an image frame, averaged in micrometres squared.[131] However, this assumption becomes questionable when the beam is focused down to nanometre-scale sizes, with hundreds of keV electrons involved. In such cases, the primary deposition events are distributed along the electron track (as discussed in Theory 2.2.3). The average dose values in STEM are often lower than those in TEM, despite the higher localised dose intensity in STEM. However, the correlation between their damage remains eclectic as a result of operational distinctions (see above), making direct comparisons of radiolysis results challenging.

Although the correlation is still considered a mystery, it is relatively straightforward to determine local radiolytic concentrations from a single downsized pulse and compare them to a broader TEM scenario. The challenges arise when trying to quantify the effects of beam displacement, which introduces computational obstacles.

Challenges in modelling. The non-uniform irradiation of the STEM beam, as it moves from one spot to another, can cause spatial disturbances in the reaction network. This was outlined in the previous chapter as an effect of mass transport, and the explanation is provided here. During fast beam scan, the characteristic diffusion times (τ_D) are shorter than the time it takes for the beam to travel between positions (τ_{flight}).[93] This pattern of irradiation creates interactions between beam positions, which requires models to quantify these effects. Despite their significance, simulations that specifically focus on radiolysis under such conditions are rare. Only one explicit modelling attempt was reported, and experimental validation is still missing. Lee and colleagues demonstrated reduced concentrations in subsampling scenarios,[89] where the spacing between beam positions is significantly larger than in raster scanning due to artificial reconstruction.[132]

The computational challenge arises from the difficulty of simulating all pixels within a single frame. Each frame may comprise a matrix with thousands by thousands of probe positions, exponentially increasing the computational cost. This involves accounting for the spatio-temporal activation of the radiolysis generation equation (R_i term in Section 3.3.2), the corresponding boundary conditions based on beam positions within the frame (x, y) and finite element refinement at each position (x, y) where the concentration gradient is established, making the process highly demanding.

Towards a Subroutine to Model STEM. This chapter introduces a subroutine for accessing this implementation, beginning with the analysis of radiolysis on both the spatial and temporal scales of STEM, testing the influence of dwell time and magnification. The workflow then progresses to exploring the effects of scan lengths when beam positions overlap, developing a scanning solution for comparison with experimental datasets.

The potential of the subroutine was verified in relation to the effects observed in STEM imag-

ing of colloidal nanochemistry;[133] apparently, the local chemistry induced by the beam at the liquid sample interface is influenced by the direction of the beam. Previous experiments have shown that silica nanoparticles elongated in parallel with the beam direction.[131] Other studies observed the aggregation of nanoparticles in patterns similar to scanning illumination.[134] Using the versatility of creating geometries with Comsol, radiolysis estimated under different *beam-liquid-sample* positions provided evidence of how concentrations differ across the surface of the particle. The data sets support the hypotheses regarding the underlying mechanisms of the anisotropic beam shaping of the nanoparticles.[135]

This chapter includes results that are to be submitted to peer-reviewed journals.

- De Salvo, G.; Merkens, S.; Chuvilin, A; Predictive Scanning Radiolysis Modelling for Transmission Electron Microscopy. *Manuscript in preparation.*

5.2. Building the STEM Radiolysis Model

STEM observations have elucidated that beam parameters, such as current, dwell time, and magnification, are critical to determining the volume of interaction for radiolysis. These parameters collectively define an effective electron dose, D, which represents the flux of incident electrons that traverse the sample area. This concept has been key in the identification of a dose threshold for the nucleation of metal precursors in aqueous solutions, as demonstrated by Woehl et al.[136] Furthermore, longer dwell times have been shown to facilitate secondary reactions by prolonging the exposure of the solution to electron irradiation, thus improving the probability of secondary interactions.[137] Similarly, magnification adjustments modulate the spatial distribution of species, directly accelerating or decelerating nucleation and growth rates of irradiated colloidal solutions.[93] Although these changes in the rates did not universally correlate with the dose rate, they exhibited clear correlations under conditions of constant electron dose, suggesting that the mechanisms are influenced by dwell time and magnification. Herein, a parameter study is issued to uncover their impact in radiolysis under STEM conditions. The model used for the study was 1D reaction-diffusion (see Chapter 4) with a change in beam dimensions and electron flux/dose rate.

Effect of Dwell Time. The dwell time can significantly alter the radiolytic effects during a single pulse, as stationary conditions are not reached within the microseconds of dwell. Figures 5.2a and b show temporal concentrations during and after a pulse, maintaining a constant dose on a 25 nm^2 pixel surface. The concentrations generated in a pixel with dwell times of 1 μs (Fig. 5.2a) and 20 μs (Fig. 5.2b) predominantly consist of primary species (indicated in red with non-zero G values), while secondary products, illustrated in green (O_2^-), are at near-zero concentrations. Specifically, species such as O_2, HO_2^-, $HO_3^\bullet$, O_3^-, and O^- appear at negligible concentrations. All values reach a stationary profile before the end of the pulse, and decay over times ranging from 10 to 100 μs for dwell times of 1 μs and 20 μs, respectively, once the irradiation finishes. This normalised stationary concentration is presented in Figure 5.2c for comparison between the different data sets. The generation of primary species remains similar across varying dwell times (illustrated by the red bars in Fig. 5.2). Although secondary species are insignificant for a short pulse, their concentration can increase drastically with longer dwell times (20 μs, illustrated by the dark green bar in Fig. 5.2c), as secondary reactions are favoured by prolonged irradiation.

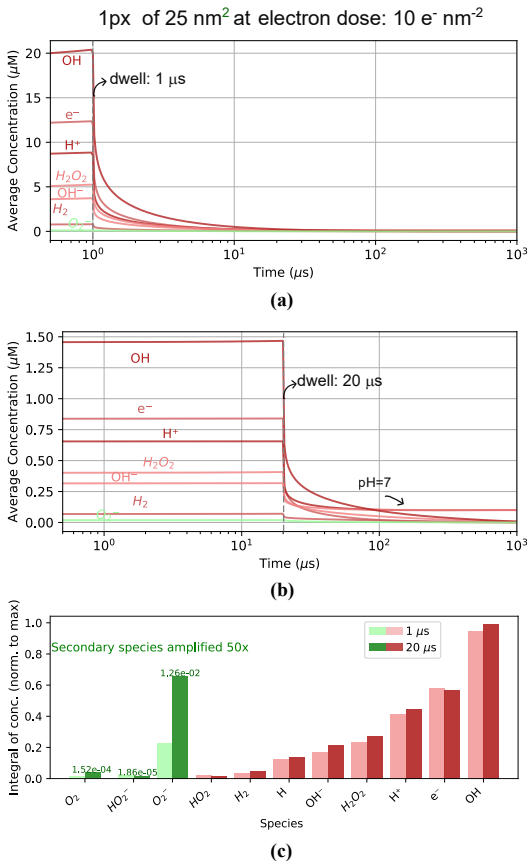

Figure 5.2: Surface average concentration per 1 pixel ($25\ nm^2$) with an electron dose fixed at $10\ e^-\ nm^{-2}$ for a continuous pulse duration of: **a)** $1\mu s$ (dose rate: $5.5 \times 10^6\ e^-\ \mathrm{nm}^{-2}\ \mathrm{s}^{-1}$), **b)** $20\mu s$ (dose rate: $2.7 \times 10^5\ e^-\ \mathrm{nm}^{-2}\ \mathrm{s}^{-1}$). **c)** Constant values species are reported in bar plot for comparison of different dwell times regime.

Effect of Magnification. The STEM probe traverses between pixels at a velocity v_p over a distance l_{pixel}. The characteristic time for the probe to jump from one pixel to another, known as t_{flight}, is calculated as $t_{\text{flight}} = \frac{l_{pixel}}{v_p}$. Despite the dependence of t_{flight}, experiments suggest that this time remains constant across imaging setups due to the direct proportionality of l_{pixel} and v_p.[93] Consequently, a consistent flight time is expected regardless of variations in the probe distance. The effects of different distances, specifically $l_{pixel} = 5\,\text{nm}$ and $l_{pixel} = 100\,\text{nm}$, were assessed by simulating two probes, each operating at a 1 μs dwell time with a 0.1 μs flight time, time step of each line reported in Fig. 5.3.

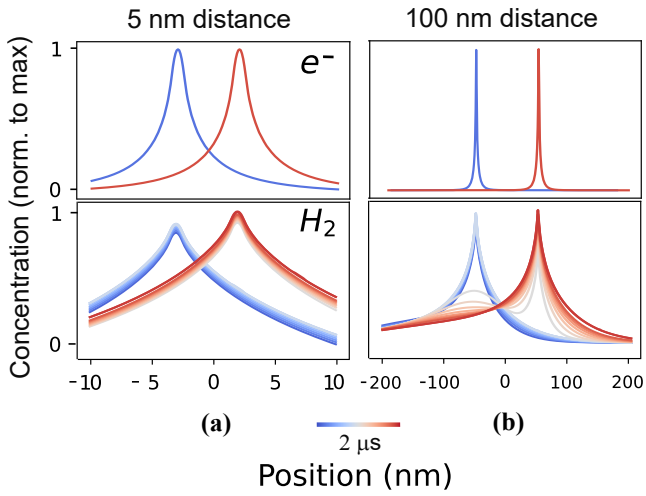

Figure 5.3: Spatial and temporal profiles of e_h^- and H_2 in STEM, illustrating: **(a)** Probes distance at 5 nm. **(b)** Probes distance at 100 nm.

The spatial profiles of two species, e_h^- and H_2, exhibit distinctly different diffusion zones for their different lifetimes: confined to a few tens of nanometres for e_h^- and extended up to hundreds of nanometres for H_2. The diffusion coefficient for both species is $D = 4.5 \times 10^{-9}$ m^2/s. The characteristic diffusion times (τ_D) at distances ranging from 5 to 100 nm are calculated using the formula $\tau_D = \frac{l_{pixel}^2}{D}$, resulting in $\tau_D \approx 5 \times 10^{-9}$ s for $l_{pixel} = 5$ nm and $\tau_D \approx 2 \times 10^{-6}$ s for $l_{pixel} = 100$ nm. When $l_{pixel} = 5$ nm, the diffusion of species is faster than the movement of the beam ($\tau_D \ll \tau_{flight}$), resulting in a significant concentration of species around an adjacent pixel. However, at $l_{pixel} = 100$ nm, where $\tau_D \gg \tau_{flight}$, the probability of overlapping concentrations decreases drastically. This is evidenced by a visible accumulation of hydrogen at a distance of 5 nm, marked by an increase in the second peak of Fig. 5.3a. As the probe distances expand to 100 nm, this accumulation becomes less evident. This trend aligns well with the predictions of H_2 for scanning in well-separated positions by Lee et al. [89] In parallel, more reactive species, such as electrons, show no interaction between pixels at distances of 5 nm or 100 nm, as evidenced by the stable spatial and temporal profiles presented in Fig.5.3a and b.

The above study pointed to the possible overlap and accumulation of the H_2 product at short distances between the scanning probes. Now that this is clear, it can be simulated

what the distribution of species looks like for an extended scan line (up to 250 pixels) by keeping dwell of irradiation (1 μs) and probe distance equal to $l_{pixel} = 5\,\text{nm}$.

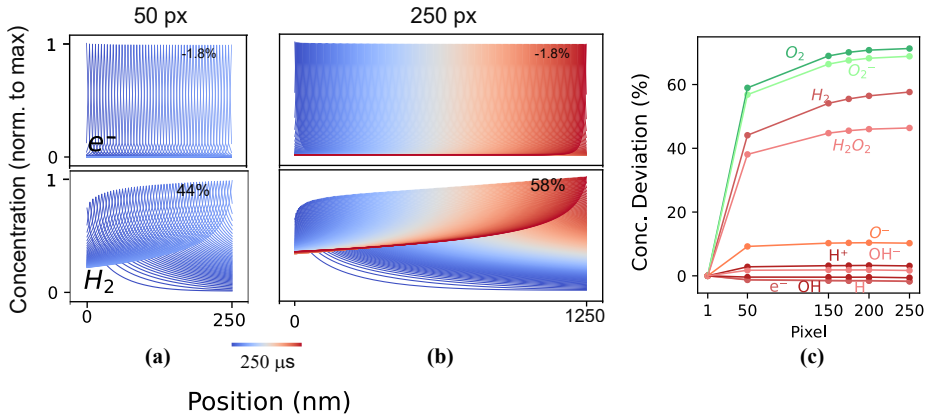

Figure 5.4: Spatial and temporal profiles of $e_h{}^-$ and H_2 in STEM, illustrating: **(a)** concentration profiles after irradiation across 50 consecutive pixels; **(b)** concentration profiles after irradiation across 250 consecutive pixels; **(c)** percentage deviations in concentration from the initial irradiation measured at 50, 150, 200, and 250 pixel positions.

Only the "fast" direction of the scan will be considered where the time delay between the pixels $t_{flight} = 10^{-7}$s is slower than the time it takes for the species to reach from one position to the other (that is, τ_D was estimated to be $\sim 10^{-9}$s at a 5 nm distance. Hence neglecting the contributes in the slow scan direction, which involves moving to the next line, here the interaction time between pixels (t_{line}) is much longer, about $\sim 10^3 \mu s$, which is long for species decaying in the time order of microseconds (see above picture of 1 μs pulse 5.2a).

A simulation was performed on a 250 px scan line, as depicted in Figs.5.4a and b. In particular, H_2 showed a significant increase in concentration, especially within the first 50 pixels, with a 44% increase as shown in Fig.5.4a. In contrast, the electrons showed a nearly constant concentration profile with a slight decrease of 1.8% from the initial irradiation. Fig. 5.4c illustrates the percentage deviations in concentration at the positions of the pixels, centred at the irradiation sites. This data shows that stable diffusive products, such as oxygen, accumulate significantly - up to 70%, with most of the increase occurring after the first 50 irradiations from the beginning, or more precisely, from the edge of an image in STEM. However, radical and ionic species are only slightly affected by the overlap of

irradiations, and thus conditions are maintained akin to a single scan at each point.

5.2.1. NanoRad-STEM: A Subroutine for Radiolysis Modeling

The study of the effects of dwell time under single irradiation conditions was straightforward to replicate using the geometries of a static beam (refer to the descriptions of the 1D model in 4.2.1). However, applying these principles to STEM introduces tricks, requiring methods capable of addressing either the displacement of geometrical boundaries (the beam) or maintaining a fixed geometry while activating domains by use of dynamic boundary conditions. Both approaches rely on advanced mesh operations. In the first, the beam zone, characterised by a higher density of finite elements, follows the STEM scanning scheme through a prescribed boundary displacement, a process known as mesh distortion. The mesh distortion approach proves inefficient for wide beam movements, as mathematical convergence becomes problematic when the distorted elements become highly irregular. An alternative approach simplifies this challenge by managing the simulation by dividing the total scan frame into smaller, independent geometry/mesh, avoiding the complexity of a single solution.

By adapting the scan concept across geometrical, physical, and chemical scenarios, the NanoRad-STEM subroutine (NANOscale RADiation in STEM) has been developed. To provide an overview of the implementation process, the steps are outlined in Figure 5.5.

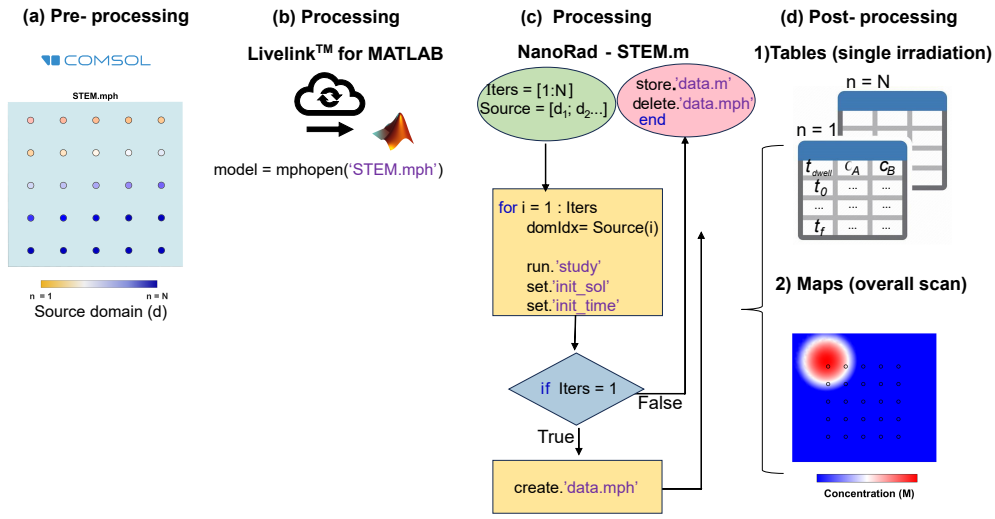

Figure 5.5: Schematic of the NanoRad-STEM subroutine illustrating the workflow developed through four distinct steps.

The pre-processing phase is essential for defining the geometry of the irradiation path with precision and adaptability. The COMSOL CAD module facilitates the design of various scan paths, including conventional raster schemes (beam domains arranged in $n \times n$ arrays, as shown in Fig. 5.5a), sparse beams for subsampling,[132] or alternative pathways such as spiral patterns.[130] For efficient geometric expansion, the Rad 4D workflow (described in Section 3.5) enables the rapid implementation of reaction-diffusion models, with diffusion being a fundamental feature for non-uniform STEM scenario. Additional physics, such as flow dynamics or electrostatic ion drift, can be incorporated as needed for more complex applications, including electrochemical simulations.

Once the geometric model is established, the processing phase begins. During this phase, a MATLAB interface is connected to COMSOL, taking control of the model created in the previous step (Figure 5.5b)[9]. The second part of the processing involves the displacement of the spatial and temporal beam generation term of radiolysis to mimic a scanning process. Figure 5.5 c illustrates the flow chart of the MATLAB script, where the iterations are initialised and linked to the model based on the number of pixels (Iters=N) and the sequence

[9]LiveLink™ for MATLAB® User's Guide. (2009) (https://doc.comsol.com). This document provides instructions for the MATLAB scripting environment interfaced with COMSOL.

of activated geometric domains (Source=d_n). A main loop runs the model in separate but concatenated simulations, computing the study for the time-dependent solution of coupled ODEs implemented before. The final concentrations of the current irradiation (n) are used as new initial concentrations (set. 'init-sol') for the subsequent scan (n+1) until the total number of scans (N) is completed, applying the same process for time (set.'init-time'). In this way, the result of one simulation can be stored and passed as initial values for the next, allowing a more robust and scalable approach, capable of simulating thousands of pixels.

The final component of the main loop is the post-processing function, which, during the initial iteration, facilitates the generation of data sets containing relevant parameters specified by the user (create.data.mph). Data from each irradiation is stored in the MATLAB workspace (store.data.mph) and can be represented as tables (for precise locations) or spatially resolved surface maps, as illustrated in Fig. 5.5d. These extracted datasets are then readily available for further analysis and processing within any scientific programming environment.

5.3. Anisotropic Dissolution in Silica Nanoparticles

In this section, we apply the workflow developed to compare observations of an intriguing phenomenon unique to STEM imaging.[131, 135, 134] In the dynamic collection of images the beam is non-uniformly irradiating the sample, and fast scanning would possibly be the first cause to produce anisotropic pathways. The shape change of the nanoparticles in solution is intrinsically related to the radiation chemistry, which drives the assembly of the nanoclusters.[133] For this reason, such studies have been chosen as a reference system to test STEM models and explore hypotheses similar to those proposed by the authors of the original experiment.

5.3.1. Experimental observations, hypothesis, chemistry

Commencing with the pioneering investigations by Zecevic et al.[131] as illustrated in Fig. 5.6a, the noteworthy STEM series show the rise of the anisotropic shape of the SiO_2 nanoparticles due to imaging. The proposed hypothesis suggested a mechanism by which dissolution and redeposition occur, triggered by radiolysis that varies with the scanned area of the par-

ticle. The authors posited that the dissolved species selectively redeposited at sites with a higher exposed surface of the scan, resulting in the elongation of the particle axis aligned parallel to the scan beam, as indicated by the blue arrows in Fig. 5.6b. However, the decreasing volume of the particles, clearly visible in the time-lapse images, contradicts this interpretation and discards redeposition as a plausible explanation (see Fig. 5.6a).

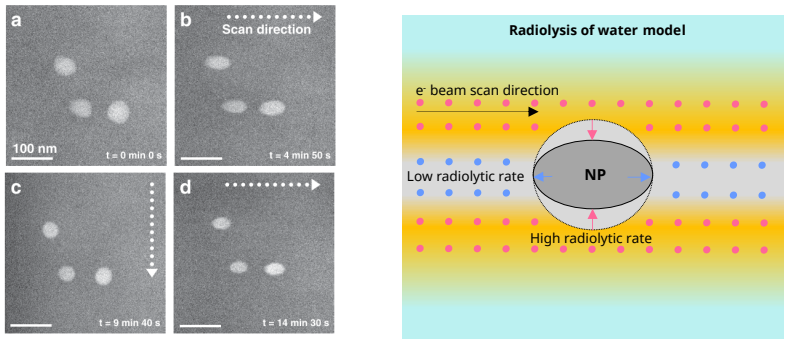

(a) **(b)**

Figure 5.6: Illustration of **a)** Beam induced etching of silica nanoparticles caused by STEM irradiation. The sequence of images shows the loss in volume of NPs and the associated scanning directionality, based on Zecevic et al.'s experiment (Copyright 2017 Advanced Science News). **b)** Proposed radiolysis model, illustrating the preferential dissolution pathways of a nanoparticle immersed in liquid water. The *red points* represent areas with a presumed high radiolytic rate, while the *blue points* mark regions with a low radiolytic rate.

A refined hypothesis by Meijerink et al. [135] attributes particle elongation exclusively to dissolution. This process predominantly occurs in regions where the beam-liquid-particle interface is more extensive. The greater the length of the interface, the more extensive the interaction between the beam and the particle, leading to an increased dissolution of atoms in the solution (highlighted as *light grey* areas in Fig. 5.6b). In contrast, areas where the beam intersects the interface perpendicularly or moves away from it witness less dissolution due to the reduced length of interaction, as depicted in the *dark grey* areas of Fig. 5.6b.

Chemistry of Silica Dissolution in Water. The instability of silica in water is a well-studied phenomenon that hinders the effectiveness of the crystalline phase in all applications in aqueous environments. [138] At the liquid-solid interface of silica, reactions with water

molecules lead to the production of $Si(OH)_4$, the orthosilicic acid species:

$$SiO_2 + 2\,H_2O \rightleftharpoons Si(OH)_4 \tag{5.1}$$

This reaction continues until equilibrium is reached at saturation concentration of silica. The majority of orthosilicic acid forms dissolves directly into the water, while the rest forms the silicate ion through the following surface reaction:

$$Si(OH)_4 + OH^- \rightleftharpoons (HO)_3SiO^- + H_2O \tag{5.2}$$

Although the equilibrium concentration of $Si(OH)_4$ in the aqueous phase (Reaction 5.1) is not affected by pH [139], an increase in OH^- concentration - and consequently pH - changes reaction 5.2 towards the formation of silicate ions. This additional by-product, together with the acid form, increases the overall solubility of colloidal silica in water. Thus, under radiolytic conditions, the elevated concentration of OH^- ions is proposed as the key driver for the dissolution of silica nanoparticles. Given this scenario, it was deemed sufficient to model the complex problem posed by STEM using only the reaction set for the radiolysis of pure water.

5.3.2. Model Description

The model delineates the differential mathematical expressions used to calculate the concentration fields $c_i(x, y, t)$ of radiolytic species i in space (x, y) and time t, under neutral pH conditions (pH 7), stabilising the kinetics as described by the reaction equations in the methods (Section 3.3). These species, consisting of 8 primary and 7 secondary, together with H_2O, participate in an established network of 73 reactions, as detailed in Table A.2. The generation of primary species within the irradiated area is quantified using G values [32] and the dose rate parameters are adjusted for the STEM-focused probe, according to experimental details.[131, 135] The spatial and temporal diffusive flux, an inherent consequence of concentration gradients created by non-uniform irradiation from a scanning probe, is mathematically described by the fourth term in the coupled reaction-diffusion equation 3.14.

Model Geometry. These equations were applied within a geometry for STEM activation, as described in Section 5.2. The geometry consisted of a 2D orthogonal plane aligned with the beam axis to represent the liquid nanochannel, as shown in Figure 5.7. The vertical thickness of the channel was excluded assuming uniformity of the absorbed dose, which negates concentration gradients and fluxes in this direction.

The central feature of the model includes a cross section of a spherical particle, highlighted in grey within Figure 5.7. This was considered to be "cut" from the water domain (i.e. no physics was active). This gave rise to additional boundaries, which are defined below.

To simulate the interaction of the STEM beam with the particle, a raster sampling scheme was implemented using a $n \times n$ array of circular domains, each spaced 5 nm apart. This raster is colour-coded (see Fig. 5.7) to indicate the beam motion relative to the liquid-particle interface: pink on the left for scanning towards the interface, white in the centre for parallel movement, and blue on the right as the beam moves away from the interface.

Reference points on the surface of the particles were used to track concentrations over time. These points define specific zones for detailed observation of changes: P_{left} and P_{right} as black squares positioned along the x-axis, and P_{centre} as red circles along the y-axis. These markers aid in monitoring changes in particle shape (e.g. radiolytic concentrations) as a result of the beam interaction. The y-axis markers are simplified to a single case taking into account the symmetry in the problem.

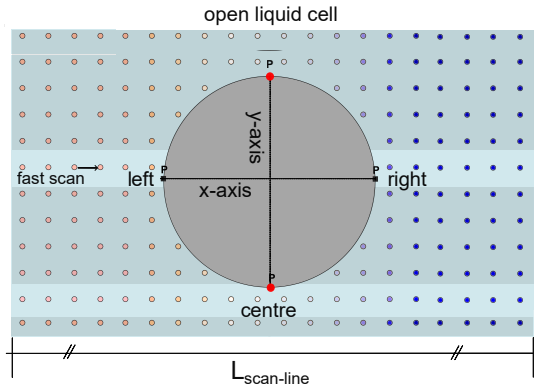

Figure 5.7: Schematic of a 2D water layer model simulating scanning beam (coloured domains) around the liquid-particle interface (grey domain). In the STEM model setup, the beam scheme surrounding the particle dictates the dimensions and is constrained by the fast scan-line length (100 pixels of 5 nm spacing for a total length of 0.5 μm), denoted as $L_{scan-line}$). The particle has a radius of 20 nm, and the beam area a diameter of 1 nm, fitting the experimental conditions.

The Boundary Conditions. The boundary conditions of the model were defined as open, aligning with the liquid cell configurations used in the reference experiments.[131] The nanoparticle surface, depicted as a grey circle in Figure 5.7, was modelled as chemically inert and impermeable, effectively closing it to prevent surface reactions and phase transitions.

The Study. Semi-quantitative analysis was limited to the scan lines, which appear bright in Figure 5.7, and are relevant to the specific study cases, such as marker points P in Section 5.3.2. Lines in dark shades are not activated as the surface transition does not concern this study. Recalling earlier calculations of the scan line lengths in Section 5.2, the model used 100 scans along a line ($L_{scan-line}$). This established the dimensions of the image frame surrounding the particle. Throughout these distances, the concentration of species, specifically OH^-, was determined to be independent of the dimensions of the frame, as analysed in Figure 5.4.

A time-dependent solution was executed in NanoRad-STEM, with local boundary conditions (e.g. radiolysis generation) dynamically updated across domains delineated by the scan lines in light shades. Each scan line was performed with a dwell time of 1 μs for a total time of 100 μs. Following completion of each scan, the script automatically saved the results and reset the boundary conditions in preparation for the next scan point.

5.3.3. Results and Discussion

In the study presented, the analysis was based exclusively on the simulated concentration of hydroxyl ions ($c_{\mathrm{OH^-}}$) given their importance in silica dissolution. The primary objective was to monitor these concentrations at designated reference points along the x-axis and the y-axis (see Fig. 5.7), comparing the changes with the experimental data.

The Study Cases. Each case study involves data from scan lines spanning a length of 0.5 μm (distance edge to edge of the STEM frame), indicated as $L_{scan-line}$, over a period of 100 μs scan, although the calculation was carried out over a longer period until conditions were restored to initial concentration values (pristine H_2O at pH=7). Figure 5.8a depicts a concentration map ($c_{\mathrm{OH^-}}(x, y)$), which captures a snapshot of the highest concentration. The data presented below show the temporal profiles of the hydroxyl ions on the left side of the particle (P_{left}). This profile displays an initial increase in the concentration of ions as the beam approaches the particle, followed by a sharp decrease as the beam passes across it. This decrease occurs because no radiolytic generation is occurring. Thus, radiation chemistry, together with diffusion, causes the decay of (reactive) radiolytic species. As the beam continues to the opposite side, the concentration of ions can still reach P_{left} by diffusing back around the particle.

For the same scan line, as illustrated in Fig. 5.8b, the concentrations were analysed at P_{right} (aligned parallel to the central x axis in Fig. 5.7). The OH^- production starts slowly and changes as the beam scans the particle. After passing this point, the concentration peaks when the beam is closest to the interface and then decreases as the beam moves away.

The third case study, shown in Fig. 5.8c, involves the second simulated scan line that runs perpendicular to the y-axis of the particle in Fig. 5.7. The evolution of concentration measured at P_{centre} shows a symmetric pattern of radiolysis, indicating changes in concentration that do not exhibit the drop observed while crossing the particle, as noted in previous calculations (compare the concentrations between the dotted lines NP in Figs. 5.8a, b, and c).

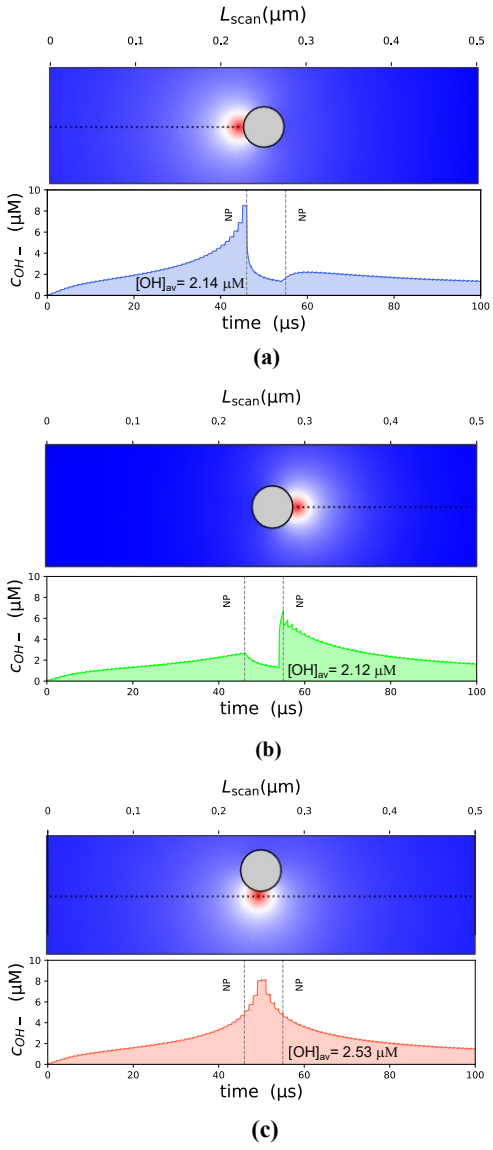

Figure 5.8: The simulation datasets presents concentration field maps ($c_{\mathrm{OH}^-}(x, y)$) at highest concentration of the temporal evolution which is extracted from points at the particle interface: **a)** P_{left}, **b)** P_{centre}, and **c)** P_{right}, over 100 pixels irradiation. The pixel centres were spaced at $d_{\mathrm{pixel}} = 5$ nm. Simulations were performed at an electron flux rate of $7.9 \times 10^6\,\mathrm{e}^-/\mathrm{nm}^2 \cdot \mathrm{s}$, calculated within a beam radius of $r_{\mathrm{IA}} = 0.5$ nm, using an electron energy of 300 keV and a low beam current of 1 pA.

In summary, the different scan line simulations illustrate the importance of correct geometric implementation of radiolysis models, revealing a shadowing effect of the nanoparticle on the concentration of radiolytic species.

Subsequently, the results of each scenario are integrated from scan time zero to concentration decay to zero after 100 μs, which is not shown on the graphs. The resulting values are then normalised by the total time, providing a measure of the average concentration over the duration of the irradiation effects, denoted as $[OH^-]_{av}$. These values are denoted in Figs. 5.8a, b, and c. The average concentrations of hydroxide ions are: 2.14 μM at one end of the x-axis (Fig. 5.8a) and a slightly lower concentration of 2.12 μM at the opposite end (Fig. 5.8b). Along the y-axis (Fig. 5.8c), a higher simulated concentration of 2.53 μ M is observed, approximately 20% greater than those along the x-axis.

Our calculations are designed to correlate observed experimental changes in particle dimensions with variations in simulated hydroxide ion concentrations. Specifically, lower concentrations along the x-axis (Figs. 5.8 a and b) are associated with minimal material dissolution and potential redeposition, as indicated by Meijerink et al.[135] The STEM images reported a modest average increase from the original length (from 10-20% in $\Delta L_x/L_{x,0}$).[135] At the same time, higher concentrations along the y axis (Fig. 5.8 c) correlate with greater material degradation, as evidenced by a decrease of more than 30% in $\Delta L_y/L_{y,0}$ also observed by Zecevic.[131] This pronounced shrinkage, primarily along the y axis, suggests that dissolution, by scanning perpendicular to the particle axis, dominates particle dissolution. Although limited redeposition occurs in the parallel axis to the scanning process, it can only be fully explained by incorporating surface chemistry into the model, yet experiments suggest that redeposition is unlikely to counteract the dissolution of silica.

5.3.4. Conclusions

Our modelling subroutine has shown great promise in setting up simulations that explore typical scanning (liquid) irradiation conditions, an area that has previously received limited attention. The study highlights the ability of this tool to predict radiolysis outcomes in STEM, especially observed in the anisotropic dissolution of SiO_2 particles, a rare example of multidimensional simulations associated with laboratory data in LP-(S)TEM studies.

Despite these achievements, there is still room for improvement. As for quantification, it becomes clear that some foundational assumptions need to be re-evaluated, particularly G

values. These values may need adjustment due to the high energy and density typical for STEM probes, a topic detailed in Chapter 2.

In the upcoming chapter, we explore these adjustments for the first time in the context of electron microscopy, introducing new insights that could prompt a rethinking of our current STEM models.

CHAPTER 6

RADIOLYSIS MODELLING AT HIGH DENSITY AND ENERGY ELECTRON FLUXES

6.1. Introduction

Numerical methods demonstrate superior versatility with respect to radiolysis quantification experiments in the context of *in situ* electron microscopy. Experimental efforts in this area have been conducted with the specific limitations inherent in the electron microscopy setup.[27] On the theoretical simulation front, no studies have yet been published that verify radiolysis yields evolution under high-density and energy electron fluxes. LP-TEM simulations have so far used G values calculated [32] for the time frame 1 μs after electron impact. Refer to Fig. 2.1.

Various theoretical models, ranging from deterministic [67, 62, 69] to stochastic,[32, 68] are used to derive G values, capturing the dynamics of radiolysis in the chemical regime. In these models, the spatial configuration of the reactive species plays a crucial role. At the picosecond scale, species are considered to be generated within a nanometric region, reflecting the localised burst of energy deposited. As the time scale extends to microseconds, the model transitions to consider species within homogeneous volumes, which represent the diffusion and interaction of species. Substantial work has been carried out to model the behaviour of the observable species in this time regime (e.g., hydrated electrons and $OH^{\bullet}$ radicals recombination from picosecond pulse radiolysis). The inherent assumption is that every electron generated region (spherical spur at 200-300 keV) evolves separately, which is true for low densities of electrons but may be wrong for high rates in LP-TEM.[73]

In this chapter, the transfer of this knowledge (continuous and deterministic description of a spur) to a finite element model is discussed to describe reaction-diffusion kinetics for the initial 10^{-6} s. This model is compared to existing models that allow different spatial distributions of radicals fitting experiments such as hydrated electrons ($e_h{}^-$) [62] and hydroxyl radicals ($OH^{\bullet}$),[67] verify its validity, and use it to compute more complex scenarios corre-

sponding to high electron fluxes. It is shown here that the commonly accepted G values used in the Schneider model [23] may need to be corrected to account for high current densities, such as those found in STEM mode.

This chapter includes results that are to be submitted to peer-reviewed journals.

- De Salvo, G.; Merkens, S.; Chuvilin, A; Finite Element Prediction of Microsecond Radiolysis Yields for High Dose Rate Applications; *Manuscript in preparation.*

6.2. Short Time Radiolysis Kinetics

Prior to solving the equations for diffusion, it was essential to understand the reaction set used for the short-time kinetics of primary species (refer to the paragraph *Primary Reactions* in Section 2.2.3). The reaction set was first compiled from Schwarz, incorporating reactions involving radiolysis species with only rate constants that exceed $10^8\ M^{-1}\,s^{-1}$,[67] and thus are valid for the analysis of short-term kinetics (approximately $1\,\mu s$). The Schwarz reaction set contains ten reaction rate equations between seven primary radiolytic species, including $e_h{}^-$, $H^\bullet$, $OH^\bullet$, H^+, H_2; H_2O_2 and OH^- (compare Table B.3).

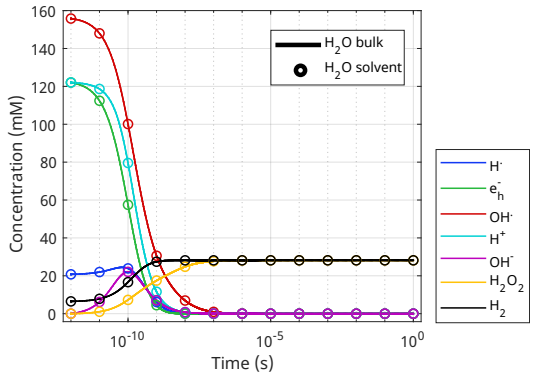

Figure 6.1: In the homogeneous spur modelling of radiolysis, the initial concentrations of the products are monitored over time through 10 interconnected reaction rates (see table B.3). Steady state is achieved at 10^{-7} s. According to species concentrations corresponding to g^0 values listed in Table B.1 and to a spur radius of $r = 2.121$ (Trumbore set). The analysis confirms that using water as either solvent and bulk species generate a validated set.

The study of the rate of primary reactions, or the speed at which they occur, is crucial to de-

termining whether species recombine within the assumed temporal range. For this analysis, a zero-dimensional (0D) solution was employed. The initial concentrations of species were established from the initial g values or g^0 (yield at 10^{-12}s), and the spur volumes for determining the concentrations c^0 are listed in Table B.1. The initial conditions are excluding the continuous beam generation term as for the previous models presented, reflecting pulsed generation in spur. The chemical interconversion of species was calculated using the kinetics of consumption and production reactions, and the differential forms of their rates were evaluated with water species considered both as solvent and as a bulk reacting species (refer to 3.3.1) for the reaction rate equations in different solvent treatment). Figure 6.1 compares the temporal evolution of both water treatments. The intermediate reactive species decay to a concentration of zero at approximately 10^{-7} s, fully converting into molecular hydrogen and hydrogen peroxide, thereby establishing a steady state of these species. However, it should be noted that the set does not address certain primary species with minimal production, such as $HO_2^{\bullet}$ and $O^{\bullet}$, which are not considered crucial in the reactions studied.

Reaction Set Validation. The following discussions on homogeneous kinetics serve to validate the consistency of this set of reactions. It is important to realise that all new zero-dimensional (0D) solutions assumed for dimensional expansion must adhere to conservative principles.

The solution was verified with respect to both mass and charge conservation. Fig. 6.2a shows the overall concentration of hydrogen and oxygen atoms throughout the calculation (with water as the assumed bulk species), which proves mass conservation. Fig. 6.2b compares the concentration of positive and negative species, demonstrating charge conservation.

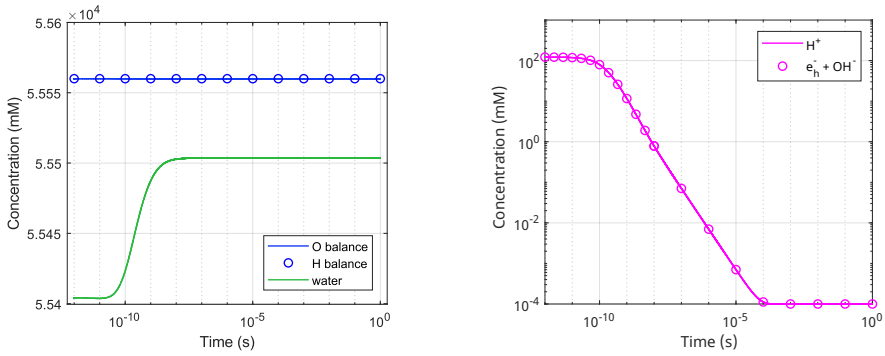

Figure 6.2: Conservation Laws Demonstrated in the Schwarz Radiolysis Kinetic Set. Figure **a)** focuses on the mass conservation of H and O species, showing the concentration of pristine water ($c_{H_2O} = 5.556 \times 10^4$ mM) before irradiation (blue line) and its subsequent variations (green line), which illustrate the dynamics of species creation and recombination. Figure **b)** addresses charge conservation, initiated by the balance of primary hydrated electrons and protons. This equilibrium is maintained by chemical reactions, notably reaction $n°3$ in Table B.3.

After the conditions of the kinetic solution were verified, the model was expanded to include a spatial "spur" description, thereby accounting for the heterogeneous diffusion kinetics of the species. Specifically, considering the lifetime of a spur (approximately $1\,\mu$s), the diffusion length of the species can reach hundreds of nanometres. Under these conditions, the reaction kinetics can change drastically, highlighting the importance of incorporating spatially resolved diffusion effects into the model.

6.3. The "Spur" model

A deterministic approach to the kinetics and diffusion of radiolytic species generated immediately after the deposition of energy along the path of an electron, namely the physical and physico-chemical stages of radiolysis (refer to Section 2.2) involves solving the temporal and spatial evolution of the species i with their concentrations c_i present in the short-time radiolysis kinetics (see above). This coupling of these equations is achieved using a set of differential equations, as noted previously in Section 3.3.3. The assumption behind a continuum "spur" description is that in one event of scattering, radiolytic primary species are formed in dense regions approximated as spherical when high LET or more elongated cylindrical regions for low LET cases [62].

The reality of generation events was found to be better reflected by employing initial concentration distributions of radiolytic species using preset functions. These functions explain why radicals are not formed homogeneously within a spur. A commonly used function is Gaussian, as prescribed in Schwarz's diffusion theory [55, 67]. Subsequently, a suggested shape distribution was developed for the evolution of fast-reacting radicals, with the aim of finding the best fit to the experimental yields observed in pulse radiolysis experiments.[62] In support of this approach, other studies have shown that examining zero-time reactions reveals a rapid depletion of radicals at the centre of the spur. [68] In particular, Trumbore proposed a novel functional form for hydrated electrons, which incorporates a central minimum. This adjustment provided a significantly improved fit to the experimentally observed decay profiles, further increasing the importance of accurately modelling spatial distributions in deterministic approaches.

Initial Concentration Distributions. Two distinct functions derived from established models [67, 62] are used to describe the initial spatial distributions of species concentrations (at time zero, corresponding to the first picosecond or the end of the physico-chemical stage). These functions were adapted to translate the spherical symmetry of a single spur into a 2D spatial framework in cylindrical coordinates (r, z), while rotational symmetry in ϕ was omitted to assume homogeneity around the axis.

The Gaussian distribution, commonly used to model spatial diffusion profiles, is employed as the basis for the initial concentrations. These distributions are expressed in terms of their radial and axial dependence as follows:

$$c_i(r,z) = \frac{N_i}{N_A(\,\pi\, b^2)^{3/2}} \cdot exp\left(-\frac{r^2+z^2}{b^2}\right) \quad (\mathrm{mol/m^3}) \tag{6.1}$$

where N_i represents the number of molecules and N_A the Avogadro constant. The characteristic length of the Gaussian, is derived from:

$$b = \sqrt{2}\,\sigma_{spur}^2 \tag{6.2}$$

related to the radius of the spur σ_{spur} at the point of inflection of Eq. 6.1. Additionally,

the function with a minimum at the centre was applied to e_h^-, as shown in the following equation:

$$c_{e_h^-}(r,z) = c_{e_h^-,max}\left(\frac{2}{3}\right)^{3/2} \cdot exp^{+3/2} \cdot \left(\frac{\sqrt{r^2+z^2}}{d}\right)^3 \cdot exp\left\{-\left(\frac{\sqrt{r^2+z^2}}{d}\right)^2\right\} \quad (\mathrm{mol/m^3}) \tag{6.3}$$

In this equation, $c_{e_h^-,max}$ is the maximum peak concentration based on the total concentration of a spur with radius σ_{spur} and multiplied by a factor for integral normalisation, as follows:

$$c_{e_h^-,max} = \frac{N_{e_h^-}}{N_A\left[\frac{4}{3}(\pi\,\sigma_{spur}^2)^3\right]} \cdot c_{norm} \tag{6.4}$$

The radial parameter d is based on r_{max}, the total radial distribution length was fixed at 10 nm:

$$d = (2/3)^{1/2}\, r_{max} \tag{6.5}$$

The resultant distribution of species are depicted in Figures 6.3a and 6.3b for Gaussian and central minimum function, respectively. The function displayed in Fig. 6.3a reaches a maximum at the coordinates $(r,z) = (0,0)$, located at the centre of the spur. The characteristic radius of the spur (σ_{spur}) determines the Gaussian length for all species. Moving to Fig. 6.3b, the function that fits the minimum electron is determined by a maximum radius fixed at $r_{e_h^-,max} = 10\,\mathrm{nm}$.

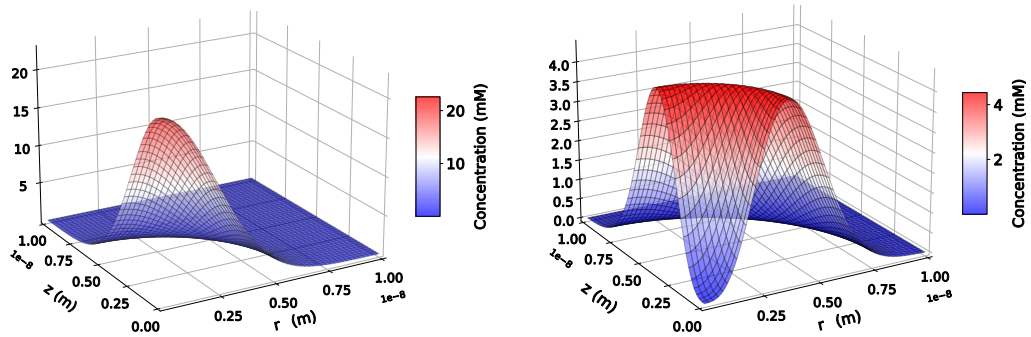

(a) **(b)**

Figure 6.3: Three-dimensional plots of the concentration of hydrated electrons, denoted as $c_{e_h^-}(r,z)$, set within a radius of $r_{e_h^-,max} = 10\,\mathrm{nm}$. Gaussian function in Fig. **a)**, represents the common distribution used in prescribed diffusion and numerical solutions. In contrast, Central minimum function in Fig. **b)**, adjusts the model at the centre to represent zero-time reactions.

In this study, the initial values of the molecules (N_i) were determined on the basis of their values g^0 and the energy deposited within a single spur (see Tables B.1 and B.2). These values are derived from direct time-dependent observations.[63, 64, 62] In some specific cases, these values can be adjusted to account for the presence of scavengers,[140] but here we focus exclusively on the distributions relevant to water radiolysis.[67, 62]

The initial concentration distributions depicted in Fig. 6.4a assume Gaussian profiles for all species. Fig. 6.4b introduces a modification in which only the e_h^- distributions are skewed away from the centre of the spur, reflecting a non-uniform spatial profile.

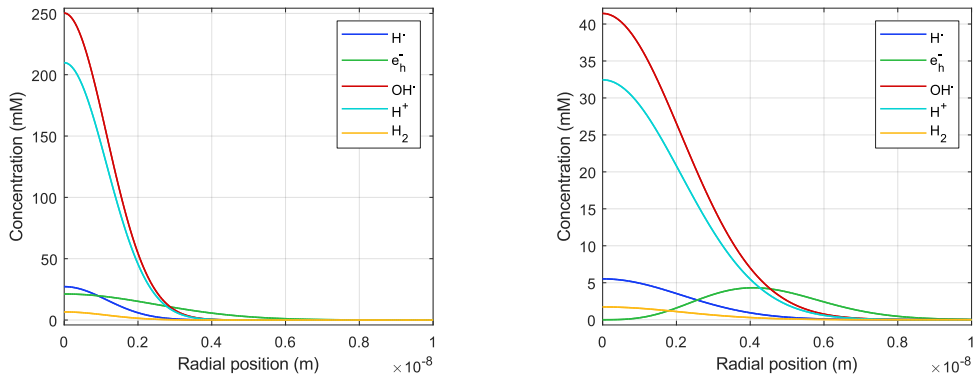

Figure 6.4: Initial concentrations profiles at time zero ($t_0 = 1\,ps$) for the radiolytic species associated with the g^0 values in Table B.1. In Figure **a)**, curves are modelled using Equation 6.1 for a spur energy of 62.5 eV and electron radius of $\sigma_{spur} = 2.458$ nm. The radius of $\sigma_{spur} = 1.145$ nm applies to all other species plotted. In Figure **a)**, the curves refer to a spur of 60 eV energy, modelled with Equation 6.3, where the electron radius is $\sigma_{spur} = 2.121$ nm and the radius of $\sigma_{spur} = 2.309$ nm again applies to all other species.

The selection of these initial concentrations, particularly the characteristic lengths of the distribution and other parameters that depended on the radial position, was based on the Schwarz and Trumbore data sets (refer to the Burns concentration profiles and Appendix B for reproduction of distribution functions).[69]

Geometry and Symmetries. The model was conceptualised using a spherical spur "paradigm" (see Fig. 6.5a), where the species are initially generated within a spherical domain and diffuse outward into a liquid medium. This assumes that the external environ-

ment is significantly larger than the spur itself, effectively acting as an infinite reservoir. To represent this, a 2D quarter-circle geometry was adopted. This geometry extends along the radial (r) and vertical (z) axes, with rotational symmetry around the azimuthal angle $\phi = 360°$, as illustrated in Fig. 6.5b. The implementation effectively represents half of a sphere, which is reconstructed by utilising mirror symmetry along the r-axis. Note that this geometry is exactly suitable for the spatial coordinates of the initial concentration distributions described in Figs. 6.3a and 6.3b.

This 2D geometry uses cylindrical coordinates $(r, z, \phi,)$ to allow simulations of multiple spurs. In contrast, using a spherical system, which requires a 1D distance described by r, θ, ϕ coordinates, fits well to model a single spur, but limits exploring interactions between multiple spurs. For the simple reason that replicating the distance between spurs requires a second distance or axis, such as z in this study.

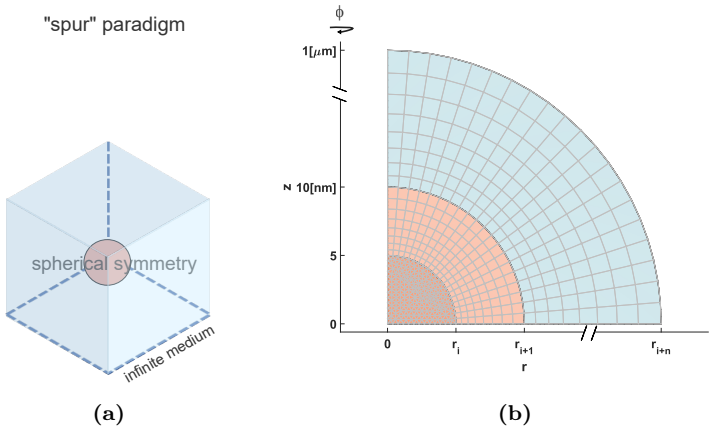

(a) **(b)**

Figure 6.5: Spur Paradigm and Geometry **a)** The 'spur' paradigm conceptualizes a problem in which a volume of densely concentrated species diffuse with isotropically until it reaches a homogeneous distribution. **b)** The 2D geometry with cylindrical coordinates revolves around the vertical z axis by $\phi = 360°$, while the r axis acts as a zero normal diffusive flux boundary for species. The entire structure features concentric zones, indexed from i, each ensuring a constant growth ratio of the mesh. Apart from the innermost zone, with a characteristic radius of $r_i = 10\,\text{nm}$, is the only one that applies a free triangular elements mesh as a seed. Subsequent zones, at r_{i+1}, enable consistent control of mesh growth (mapped mesh). The outermost zone, with a characteristic radius $r_{i+n} = 1\,\mu\text{m}$, is set large enough to apply open boundary.

The precision of the solution was handled using a mesh in which the nodes exhibited a constant growth rate along the radial axis, as shown in Fig. 6.5b. To allow for this process,

additional transition boundaries were employed, allowing mesh flexibility to resolve diffusion-induced concentration gradients. This structured approach was ensured by dividing the model into subdomains, highlighted in different colours for spur (pink) and water medium (light blue), described by concentric zones with characteristic nanometre radii (r_i), which depend on the initial distributions of the species. The subsequent transition boundary (r_{i+1}) was chosen only for the convergence of the mesh and the balance between the computational cost and the precision of the solution. The outermost boundary, defined by a radius of r_{i+n}, was set sufficiently large to act as an open wall, ensuring zero concentration for all species except those of neutral pH water.

6.4. Model Validation

The described spur model was used to solve the concentration gradients expressed in differential form as described in Section 6.3 and the solution was calculated using the PARDISO direct linear system solver in COMSOL. The temporal resolution was achieved by setting an initial forced time step of 10^{-15} s over 10^{-12} s resolved dynamics, and employing a Backward Differentiation Formula (BDF) algorithm, specifically the Euler method of first order, to effectively manage incremental increases in the time step. These solver settings covered a time-dependent study ranging from 1 ps to 1 μs within a logarithmic sequence (for more details, refer to *Numeric Solvers* in Section 3.4).

Boundaries. To prevent the flux of species, the open boundary located at position r_{i+n} in the geometric model was extended. Figures 6.6a and 6.6b illustrate the radial concentration profiles of all species at 1 μs, respectively. At the boundary, the concentrations of all species are zero, except for the self-protonating water species. These species maintain a concentration of 10^{-4} mM, consistent with the neutral pH conditions defined by the open boundary conditions.

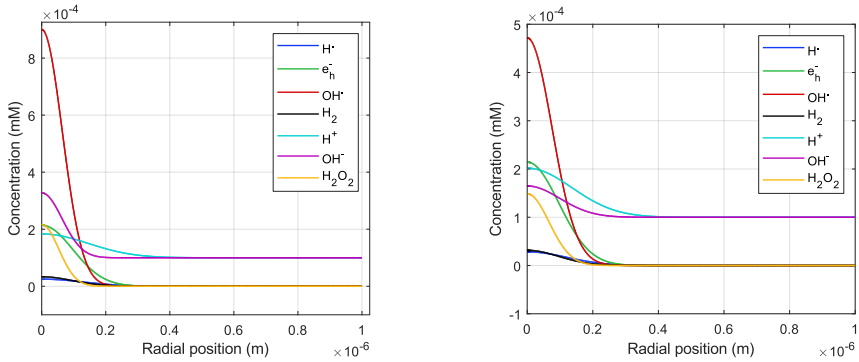

Figure 6.6: Concentration profile at final time of the calculation (t = 1 μs).**a)** Schwarz model initial parameters (see Appendix B.1)**a)** Trumbore model initial parameters (see Appendix B.1)

G values. The spur concentrations solved in COMSOL were compared using the approach outlined by Burns et al.:[69] the overall yield decay was first compared with the numerical solutions of the FACSIMILE code,[70] and then with the reference values of the pulse radiolysis experiments.[63, 64]

To achieve this, a surface integration was performed over the spur geometry illustrated in Fig. 6.5b using the operation described in Eq. 6.6.

$$\#M_i = 2\,\pi\,N_A \int_S c_i(r,z)\,r\,dr\,dz \tag{6.6}$$

The integration was doubled to account for the mirror symmetry, resulting in the total number of molecules $\#M_i$ across a sphere with a radius equivalent to the maximum extension of the model. This ensured coverage of the entire spatial diffusion domain of interest. Then it was normalised to standards of 100 eV energy deposition commonly used in radiation studies. The time evolution of #M/100 eV was compared to the values reported by Burns et al.[69] The curves that were not present in this comparison are extracted from other authors who tested these models of pure water against scavenged yields.[140] Figures 6.7a and b illustrate the agreement between the calculations presented in this study and the parametrised *ad hoc* calculations from Schwarz and Trumbore, respectively.

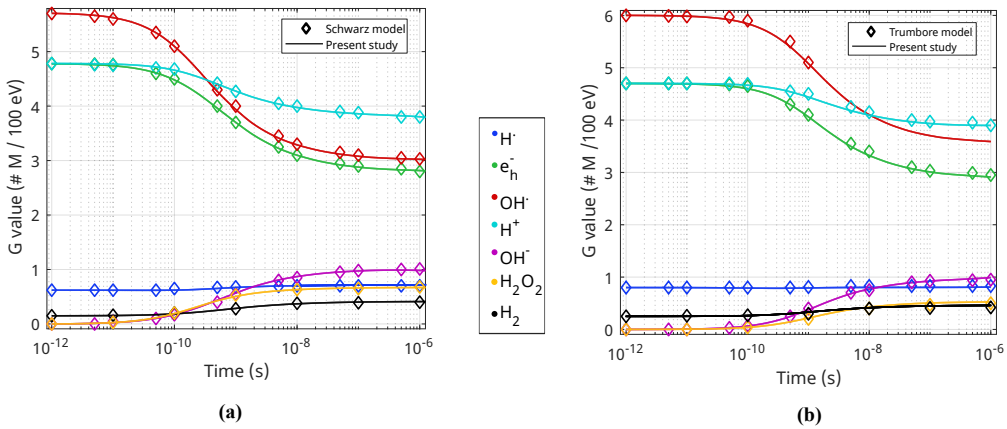

Figure 6.7: The estimated yields of molecules per 100 eV from 1 ps to 1 µs. Results from the "spur" model are indicated by the solid line, while the diamond markers represent values from **a)** Schwarz and **b)** Trumbore. Both sets of data utilize the parameter space found in Table B.3 for comparison.

After a successful reproduction of the models, in the next step, the values were compared with the experimental yield decay curves observed by Jonah et al., using a picosecond pulsed radiolysis system,[63, 64] with a resolution of hundreds of picoseconds. The experimentally predicted trends were used initially to adjust the initial parameters of the Schwarz and Trumbore models and fit the decay time range, from 100 ps to 3 ns for e_h^- and from 200 ps to 3 ns for $OH^\bullet$, as shown in the Burns comparative study.[69] More recent studies, such as those of El Omar et al.[141] have improved the resolution of experimental observations to 15 picoseconds. Although these adjustments did not produce substantial changes compared to the work of Jonah et al., they significantly improved the quality of the data and its fit through innovative setups. For the first time, Figures 6.8a and 6.8b compare a finite element model of this work, with past and present milestone experiments. Note that none of the initial distributions is capable of replicating both decays accurately. The values of hydrated electrons are better fitted by the central minimum distribution, while the Gaussian appears to agree reasonably well with the decay curve $OH^\bullet$.

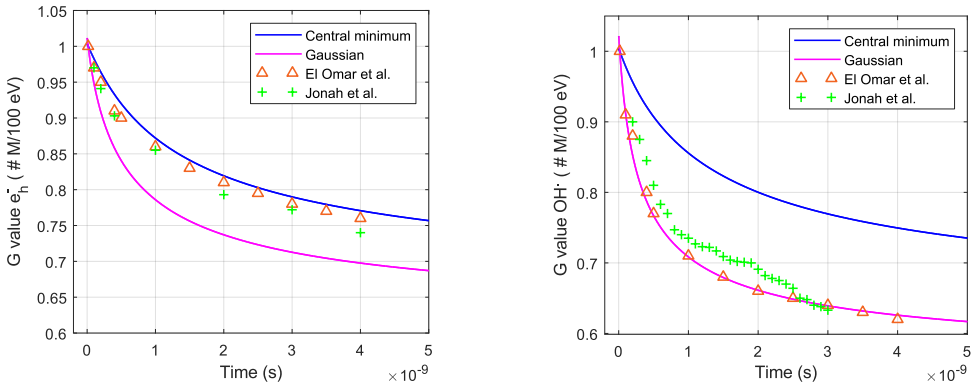

Figure 6.8: First comparison of a spur Finite Element Model (FEM) with experimental decay yields from pioneering studies by Jonah (1977) and El Omar (2011) using a picosecond radiolysis setup. In **a)**, yields of hydrated electrons show a better fit with the central minimum spatial distribution. In **b)**, $OH^{\bullet}$ yields correlate better with the Gaussian distribution.

As can be seen, the fit from the calculations is improved with the new values provided by El Omar and co-workers.[141] The fluctuations present in the data set of Jonah et al., which were attributed to electron beam artefacts, have been corrected. The discrepancies can be addressed by the review of kinetics constants and parameters screen of the spatial distribution to replicate both $e_h{}^-$ and $OH^{\bullet}$ temporal decays with a unique model.

Accuracy of Predictions. After comparing the model with theoretical and experimental references, it was optimised to improve its accuracy. For predicting the G values, optimisation focused on refining the mesh resolution to achieve reliable numerical results with an accuracy consistent with the standards of radiation chemistry (i.e., values accurate to 1 or 2 digits after the decimal point).

The mesh refinement analysis mainly targeted the inner unstructured triangular mesh (see Fig. 6.5b), as it dictates the subsequent growth rate of the elements throughout the model. In the outer regions, at a radius of r_{i+n} (where n represents the number of concentric zones), the mesh was parametrised to maintain a fixed growth ratio of elements along the radial profile (see Fig. 6.5b).

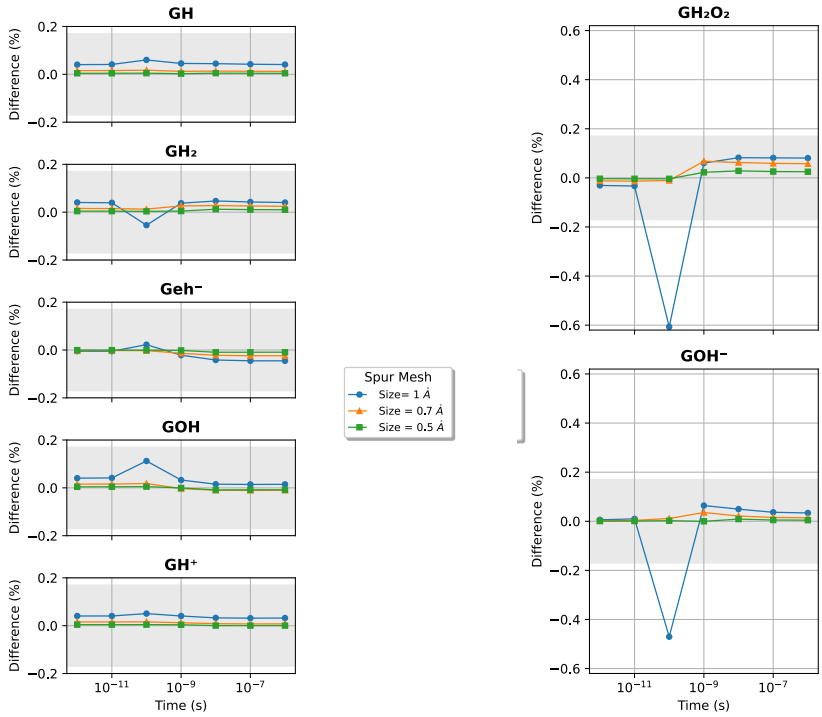

Figure 6.9: The differences in G values achieve accuracy at all times for element sizes at inner spur mesh sizes of 0.5 Å and 0.8 Å, compared to the finest mesh size of 0.4 Å. The values for primary radiolysis species **a)** and secondary species **b)** are calibrated to the highest initial G-value species, remaining within the precision range to the hundredths place (indicated with a Gray background).

Figures 6.9a and 6.9b illustrate the percentage differences in G values between meshes of different resolutions versus the finest resolution of 0.4 Å, two orders of magnitude smaller than spur reaction radii. Specifically, the differences in the G values with stable numerical solutions of 0.5 Å and 0.7 Å with accuracy up to the hundredth place. More pronounced but not substantial deviations (max 0.5 %) were observed within the temporal range of 10^{-11} to 10^{-9} seconds, when the mesh size increased to 1 Å. This time range coincides with the onset time of strong concentration gradients and the decay or rise of the G value curves (refer to Figure 6.7 for a detailed view).

Understanding the accuracy of the mesh at spur lengths allowed the division of elements in half, significantly enhancing computational efficiency when the spur domains were doubled

for the following simulations.

6.5. High LET Simulations - Results Discussion

Verification of the Schwarz and Trumbore models has enabled accurate comparisons at low spur densities. This value fits well with experiments using the femtosecond laser at ELYSE [141] that provided pulse doses typically around 22.5 Gy, orders of magnitude lower than the dose rates encountered in electron microscopy ($\sim 10^6 - 10^{15}$ Gy/s). Under such pulsed conditions, the spurs remain well separated, allowing single-spur simulations to match experimental curves with high precision (see Figs. 6.8a and 6.8b for comparisons).

The novelty presented in this section extends beyond existing models, offering the ability to predict fluctuations in G-values when the reaction radii ($r_i \sim 2$nm) of two spurs begin to overlap. This advancement enables a more accurate description of scenarios involving high LET energy deposition. The parameters analysed during this study include the screening of different average distances between spurs, which is derived from electron fluxes and beam volumes typical of LP-TEM techniques. It is also important to note that the spur model described provides an approximation for the energy deposition created by high-energy particles. Past studies have introduced suitable corrections for techniques involving low energy ionisation sources, as these influence energy deposition patterns.[73, 75] Future users of this model may need to adjust its parameters if simulating scavenged yields for specific experiments with solvents other than pure water.

For the tests outlined here, probe energies of 200 to 300 keV were assumed. This setup ensures relevance to in situ LP-TEM experiments, while providing a foundation for exploring other high LET irradiation scenarios, such as in X-ray sources [142] and their implications on water radiolysis.

Two Spur Implementation. The updated model evolves from the existing 2D quarter-circular geometry (see Fig. 6.5b) to a new double spur half-circular geometry, as shown in Figure 6.10. This configuration no longer allows for the mirror symmetry along the radial axis (r) that was present in the previous single spur model. The spurs are aligned along the vertical z-axis, which is assumed to exhibit rotational symmetry. The key parameter

along this axis is the distance d, defined as the measurement from the centre to the centre of the spurs, essential for analysing interspur interactions. The geometry, mesh and external boundary of the model are parametrised relative to this distance, aligning with the validation standards outlined in Section 6.4.

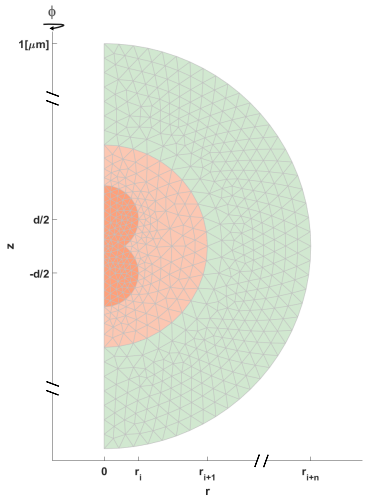

Figure 6.10: Double spur model employs a 2D geometry with 2 spurs lying in the axis revolving around an azimuthal angle of $\phi = 360°$. The model is parametrized to adjust the distance $d/2$, which is the half-distance from centre to centre of each spur. If the spurs overlap ($d \leq 2r_i$) or are close to each other ($d \geq 2r_i$), the geometry and mesh become more irregular. To address this, the concentric subdomains were all treated with an unstructured triangular mesh, as depicted from the radial position r_i to r_{i+n}.

The new implementation offers improvements over previous models that studied spur overlap in pulse dose scenarios. Previously, models allowed spurs to be generated at the same spatial coordinates in sequence,[62] posing the main limitation on the discontinuity of the overlap. The enhancements in the new simulation include:

- A more realistic geometry that better represents the actual irradiation scenario, including variable distances (d) between the spurs.
- The model now considers spurs that are close enough to initially overlap, with distances smaller than twice the reaction radius ($d \leq 2r_i$). This flexibility allows us to study the average interspur distance derived from any range of particle flux densities.

- The ability to simulate two or more spurs in a continuous manner, where spurs can be activated simultaneously or with a certain delay time.

In the simulations of double spur calculation, the spurs were placed at varying distances: overlapping ($d \leq 2r_i$), close ($d \geq 2r_i$), and non-interacting distances. Both spurs were activated simultaneously to explore how variations in average distances across different electron densities influence the chemical processes in radiolysis.

G-Values Influenced by Interspur Reactions. Initially, to determine a non-interacting average distance between spurs, the root mean square displacement for isotropic diffusion, λ, was calculated using the equation for the mean square displacement (see Eq. 3.15):

$$\lambda = \sqrt{6Dt}$$

where $D = 2 \times 10^{-9}\,\mathrm{m}^2/\mathrm{s}$ represents the diffusion coefficient for the slowest species in the set, $OH^{\bullet}$, and $t = 1\,\mu\mathrm{s}$ is the time interval corresponding to the chemical stage. This calculation yielded a λ approximately equal to 160 nm, suggesting this as the distance at which the chemical evolution of the neighbouring spurs is independent. Other distances were set arbitrarily at 0, r_i and $2r_i$ for overlapping spurs, and $4r_i$ and $8r_i$ for spurs closely interacting. The G value curves of the various species are presented in Figure 6.11, showing the kinetic and diffusion behaviour of the species from 1 ps to 1 μs. The curve for the λ distance aligns perfectly with the reference spur calculations (single spur distribution of Schwarz),[67] confirming that interactions between spurs are negligible at distances of more than hundreds of nanometres.

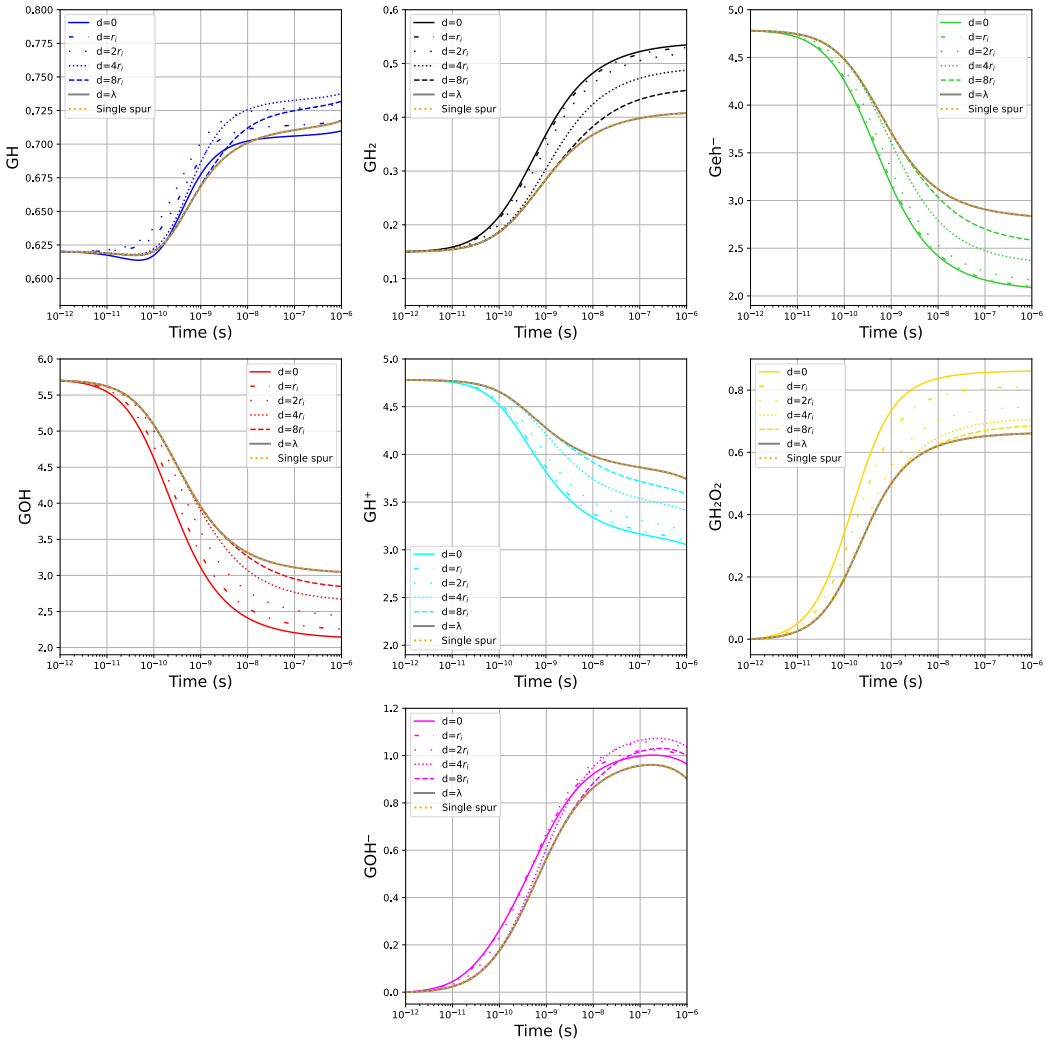

Figure 6.11: Calculated radiolysis time-dependent yields evolution at distances d of 0, r_i and $2r_i$ for overlapping spurs, and $4r_i$ and $8r_i$ for spurs closely interacting. The spatial distribution of all species is assumed to be Gaussian, as defined in Eq. 6.1, with spur parameters from Table B.1.

Throughout the simulation period $1\,\mu s$, significant changes in yield were clearly visible, as demonstrated by the shift between the coloured lines (showing overlap / close spurs) and the orange dotted line (representing a single spur) in Fig. 6.11. Interspur reactions occur already at $\sim 10^{-11}$ s for a total overlap ($d = 0$ nm), or later at a time $\sim 10^{-8}$ s for greater distances of $d = 8r_i$ (the curve of G values diverges from a single spur curve in Fig. 6.11). Observing the time-resolved curves approaching the microsecond domain, byproducts

such as OH^-, H^+, and $H^\bullet$ are created, initiating new reaction pathways. This suggests that the chemical processes are not yet complete, necessitating further research to elucidate these dependencies, likely related to the low density of spurs used in the simulation.[62] Importantly, these new pathways do not affect the yields of the recombination and formation processes, such as $G(OH^\bullet)$, $G(e_h^-)$, $G(H_2O_2)$, and $G(H_2)$, since the values reach stability at the final observed time.

Figure 6.12a shows the microsecond yields for interspur distances up to λ and a decrease, at shorter distances, is registered in the yields of intermediate reactive species such as $OH^\bullet$, ${e_h}^-$, and H^+. This decrease is consistent with rapid recombination processes that occur at lower interspur distances, thereby promoting the formation of stable molecular species, such as H_2 and H_2O_2.

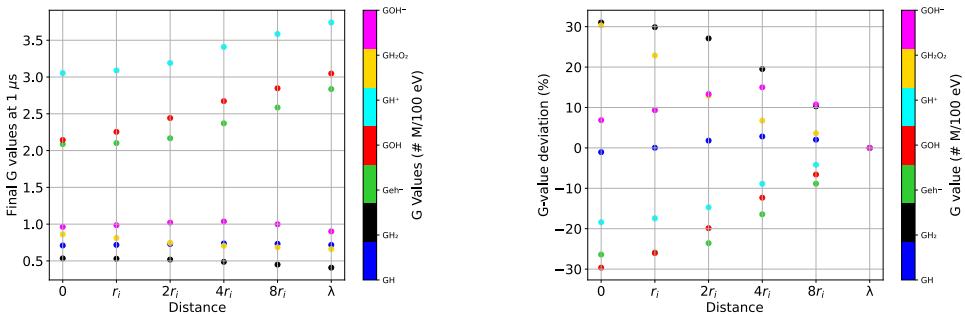

(a) **(b)**

Figure 6.12: a) Calculated radiolysis microseconds yields plotted against distances relative to the reaction radii (r_i= 2 nm) of spurs and a non interacting distance called λ. **b)** Calculated Percentage deviation of microseconds yields plotted against same distances.

Deviations from the values of the separated spurs ($d = \lambda$) are illustrated in Figure 6.12b. It is evident that the yields can vary within a range of 10% to 30%, as the spur separation decreases from $d = 8r_i$ to a state of complete overlap $d = 0$ nm.

However, to confirm that prevailing radiolysis calculations may overlook inter-spur deviations, we conduct an empirical evaluation of spur distances tailored to the operational settings of electron microscopy.

Interspur Distances in TEM and STEM. The characteristic distances (d) of the spurs generated under typical LP-TEM flux conditions are considered for electrons permeating a thin liquid layer and inducing only one scattering event for the condition of $\lambda_{IMFP} \sim t$, λ_{IMFP} the inelastic mean free path and t the thickness of the liquid layer.[82, 61] The estimation considers both TEM and STEM, acknowledging substantial differences in beam volume and current between these techniques,[26] which in turn affect the electron flux and thus the number of spurs and distances between them.

Starting from a TEM beam current of 1 nA and a beam radius of 0.5 μm. The electron rate, n_{e^-}, is determined by dividing the current, I, by the elementary charge, generating the electrons delivered per microsecond, $n_{\mu s}$ of 6000 e^-/μs. The electron density, ρ, within the beam volume is then calculated as $\rho = n_{\mu s}/V$. Given the thickness of the liquid of 100 nm, the beam volume, V, is derived as $V = \pi r^2 \times t$. The characteristic distance, d, representing the average separation between spurs, is finally obtained by taking the cube root $1/\rho$, resulting in approximately 23 nm. This calculation gives a measure of the average space each spur occupies along one dimension, assuming the entities are evenly distributed within a cubic volume.

In contrast, in STEM, a focused stationary beam with a current of 1 pA and a beam radius of 0.5 Å, with the same calculation scheme, brings a characteristic distance of 2.3 nm.

The G values presented in the previous calculations in Figure 6.12b are derived at spur separations relevant for TEM and STEM. Specifically, the values at $d = 8r_i \sim 16$ nm correspond to typical distances in TEM (d $\sim$ 23 nm), while the values at shorter distances, $d = r_i \sim 2$ nm, are representative of the conditions in STEM (d $\sim$ 2.3 nm). Table 6.1 compares the G values commonly used in electron microscopy, which were derived from stochastic calculations by Hill & Smith (that are the ones established in LPTEM),[32] and the G values for intense interactions between spurs, calculated in this study using a deterministic model.

Comparison of G values (#M/100 eV)			
	Hill & Smith [32]	This work	
	TEM	TEM	STEM
Species	$G_{(d\gg\lambda)}$	$G_{(d=8r_i)}$	$G_{(d=r_i)}$
e_h^-	3.47	2.58	2.10
H^+	4.42	3.58	3.09
$H^\bullet$	1.00	0.73	0.71
$OH^\bullet$	3.63	2.84	2.25
H_2	0.17	0.45	0.53
H_2O_2	0.47	0.68	0.81
OH^-	0.95	0.10	0.98

Table 6.1: Commonly used G values from Schneider are derived from low-electron fluxes of nuclear reactors, here denoted as $G_{(d\gg\lambda)}$, where spurs are separated by at least $\lambda \gg 160\,\text{nm}$, the distance of non interaction. In contrast, the calculations in this study assume significantly higher electron densities, with $\phi \sim 8000\,\frac{e^-}{nm^2\,s}$ and $d \sim 16\,\text{nm}$ for TEM settings, and $\phi \sim 8\cdot10^6\,\frac{e^-}{nm^2\,s}$ with $d \sim 2\,\text{nm}$ for STEM irradiation.

The tabulated values presented in this study deviate significantly from those commonly used in radiolysis calculations.[32] This discrepancy suggests that the initial conditions employed in the calculations for high-LET irradiation sources should be reconsidered.

6.6. Conclusions

This model lays a solid foundation for estimating microsecond-time G values in radiolysis, emphasising the critical role of changes in G values resulting from spur overlap in scenarios of high electron fluxes. The study establishes a reliable and experimentally verified framework for calculating G values, which is then applied to a set of pure water reactions. Upon examination of the influence of one parameter, the distance between spurs, d, it was shown that the differences in G values from the current simulations are substantial, as illustrated in Table 6.1. This finding underscores the importance of continuing research into these phenomena.

Despite its contributions, the study is preliminary and requires further verification of certain components to enhance the accuracy of the results. For example, examining more than two spurs within a single simulation could reveal whether the chemical development of spurs is

homogeneous over time, which, for some species, was observed later than 1 μs. Currently, spurs are activated simultaneously, but future models should consider the delay between the appearance of spurs and the impact on spatio-temporal chemistry.

Furthermore, this study opens the door to exploring different chemical environments, such as varying background concentrations of pure solvents or adding scavenger reactions, which could dramatically affect the assumed G values.

CHAPTER 7

SUMMARY AND OUTLOOK

7.1. Development of radiolysis modelling framework

This thesis developed a modelling framework to analyse radiolysis within chemical, physically, and geometrically complex scenarios of LP-TEM reactors. It significantly advanced state-of-the-art models by introducing new capabilities that hold the potential to enhance experimental methodologies in the field.

7.1.1. Methods Development

It became clear throughout this work that the implementation of hundreds of chemical equations in a model is a challenge in itself. The task of typing down the reaction formulas, constants, and initial values is tedious and errors can easily arise. An automated procedure was established to validate the reaction kinetics of homogeneously irradiated solutions (that is, AuRaCh).[29] In the context of this thesis, a collaboration was conducted with the AuRaCh developers to adapt their validation workflow for kinetics into a computational framework capable of expanding to geometric and physical real-world scenarios in LP-TEM. The new code is open access on Github [10], and a manuscript was submitted for publication (*De Salvo, Merkens et al., Manuscript under review at iScience*).

The initial conditions for radiolysis generation, specifically the G values, were revised for different beam densities in Chapter 6. High-density electron beams in microscopy were shown to induce distinct chemical developments in the initial microseconds of radiolysis. These models were validated against existing simulations and experiments. In addition, they were discussed in the context of STEM and TEM irradiation conditions.

7.1.2. Geometrical and Physical Expansion

The radiolysis models described by Schneider et al.[23] were accurately replicated and expanded. Theoretical studies include variations in geometries and boundary equations, and transport physics to better understand the radiolysis in the context of LP-TEM.

[10] https://github.com/GDSalvo/GDSalvo

To understand the impact of non-uniform irradiation on radiolytic species generated in liquid nanochannels (NC), we utilised a **reaction- diffusion** model (see Chapter 4). This approach considers the critical variables of open or closed boundaries and the ratio of irradiated to non-irradiated NC lengths, which significantly influence the spatio-temporal evolution of chemical species.

For systems where flow velocities are significant, a **reaction-diffusion-convection** model was introduced in Chapter 4 (*De Salvo, Merkens, Chuvilin, Nano Express, 2023*). This model incorporates the effects of convection by integrating laminar flow physics, highlighting the need for expansion to 3D models. The feasibility of replicating the results of this flow model using simplified 2D symmetric planes was evaluated. The main challenge in this study was to achieve the right balance between accuracy and computational costs, which can be challenging to implement for 3D FEM with multiple coupled equations.

The ability to predict outcomes lies in the careful construction of these models, with appropriate assumptions tailored to the experimental setup, which are summarised in Table 7.1.

Model	Requirements	Geometry	Applications
Reactions	k constants, initial concentrations (c_0), G-values μs	0D	Graphene liquid cells
Diffusion	Geometry, Diffusion coefficients, Radial symmetry, Open/closed boundary	1D	MEMS-chip
Convection	Mean flow velocity ($\mathbf{v}$), Planar symmetry	2D*	Flow setups

Table 7.1: Summary of initial values, geometries, boundary conditions of the framework of modelling for LP-TEM reactors. The Diffusion and Convection model include also the elements listed previously for simpler physics. *The 2D geometries on flow models are assumed as the most efficient computationally.

7.1.3. Implementation of STEM Simulations

A persistent challenge in LP-TEM modelling studies has been the neglect of spatial and temporal conditions specific to STEM irradiation. Although recent attempts have been made to replicate STEM conditions,[89] these efforts have not found broad application in experimental scenarios. The investigation in Chapter 5 addresses this gap by simulating radiolysis kinetics within an automatic scanning script, distinguishing it from the continuous TEM boundary conditions traditionally used as a modelling standard in many correlative studies. [23] The model is explained in its principles, will be available on Github under this link[11] (*De Salvo, Merkens, Chuvilin, manuscript in preparation.*), and is a subroutine explicitly tailored for STEM radiolysis simulations.

7.2. Basic Knowledge Obtained from Simulations

The spatial and temporal solutions analysed using novel models have significantly advanced the understanding of chemical networks in LP-TEM.

G-values change significantly under LP-(S)TEM conditions due to variations in the density of the irradiation. By extending the "spur" model to test high linear energy transfer (LET) irradiation, we verified changes in G values up to 30% compared to low LET irradi-

[11] https://github.com/GDSalvo/GDSalvo

ation. These findings pave the way for new scenarios in the future of LP-TEM simulations and suggest that the G values as a function of the electron flux may soon replace the assumed flux-independent G values.

Mass transport plays a key role for a wide range of LP-TEM nanoreactors. In the study of flow in the narrow channels of LP-TEM (*De Salvo, Merkens, Chuvilin, Nano Express, 2023*) it was found that laminar flow regimes dominate and convection transport can drastically alter the chemistry of radiolysis. In contrast, in new designs, known as diffusion cells (a concept developed in *Merkens, Tollan, De Salvo et al., Nature Communications, 2024*), the narrow island length scales make the diffusion overperform flow. Thus, radiolysis predictions were made by exploring a parameter space aligned with the advances highlighted in Table 7.2.

Study	Predictions	Parameters space	Advancements
Diffusion	Minimised gas accumulation, Faster steady state	NC width	diffusion cell [120]
Convection	Radical Increase	Flow velocities	Scavenging [28]

Table 7.2: Summary of the predictions with the novel model strategies.

The concept of a diffusion cell, characterised as an open cell with tunable diffusion nanochannel widths, has broad applicability. The open channel design promotes rapid diffusion of species from the imaging area, effectively eliminating the back diffusion effects seen in closed setups that could lead to gas accumulation in the irradiated zone.

In contrast, for setups where convection is dominant, species are flushed from the channel at varied rates, altering the chemical environment. Essentially, short-lived species may increase in concentration because self-scavengers are efficiently removed from the beam volume. Under such conditions, continuous-flow scavenging strategies may become necessary to maintain control over the system and ensure stable imaging conditions. However, these strategies have been found to be highly selective and generally not applicable.

Anisotropy in Beam Scanning in STEM Through stationary analysis of a single pulse probe, it has been clarified which species are predominantly generated within the microsecond timescale and nanometre dimensions of a STEM pixel, and how the dwell time affects this amount. Further investigations using fast scan lines of varying lengths have shown the significant impact of diffusion on species accumulation between pixels. Moreover, a model incorporating specific scan frames and sample boundaries has illustrated that the chemical environment changes depending on the length of the sample interface exposed to the scan line.

7.3. Correlation to Experiments.

Some models were successfully validated by correlating experimental data from the literature with solutions from a radiolysis model. This process was particularly evident in two specific cases:

The "spur" deterministic model reproduced from previous studies [67, 62], was rigorously validated by comparing the time-dependent radiolytic yield of $OH^{\bullet}$ found in recent studies by picosecond pulse radiolysis. [141] The advanced experimental setup exhibited reduced fluctuations, resulting in a better fit of the simulation data compared to the reference pulse radiolysis studies.[63]

The STEM workflow was designed to verify that the dynamics of dissolution at the interface between liquid and samples is influenced by the direction of scanning, through the accumulation of reactive species such as OH^{-}. Three specific case studies were used to explain anisotropic etching of particles SiO_2,[131, 135] the confirmation was obtained by correlating scan models with image data analysis.

7.4. Future Outlook on Radiolysis modelling

The expertise in radiolysis simulations and the fundamental understanding of mass transport and chemistry developed in this thesis provide a solid foundation for future advancements. Key developments envisioned include further investigation into submicrosecond kinetics and the implementation of a dose-dependent G-value generator. A modular and publicly available simulation toolbox is proposed, incorporating a chemical database for automatic reac-

tion set verification, a geometry and meshing database, dose-dependent G values, and options for scanning or continuous irradiation. Additionally, electrochemical charge migration will be implemented for liquid reactors with electrical bias, along with interface phenomena, to enable realistic simulations of surface chemistry at electron-transparent membranes, crystal growth interfaces, and bubble formation. These advances will further refine radiolysis modelling, enhancing its correlative power.

APPENDIX A

RADIOLYSIS KINETICS MODEL

A.1. Reaction set of Radiolysis of pristine water

A.1.1. Scheme of equilibrium reactions in the radiolysis of water (pk_a at 25°C) .[30]

n°	Equilibrium Reaction	pK_a
1	$H_2O \leftrightarrow H^+ + OH^-$	13.999
2	$H_2O_2 \leftrightarrow HO_2{}^- + H^+$	11.65
3	$OH \leftrightarrow O^- + H^+$	11.9
4	$HO_2 \leftrightarrow O_2{}^- + H^+$	4.57
5	$H \leftrightarrow e_h{}^- + H^+$	9.77

Table A.1: Reaction scheme of Acid-base reactions dependent on pK_a.

A.1.2. Scheme of Radiolysis of Pristine water (k at 25°C).[30] The units of k are always ($M^{-1}s^{-1}$) unless specified.

Acid-base Reactions dependent on pK_a		
n°	Reaction	Rate Constant ($M^{-1}s^{-1}$)
1	$H_2O \longrightarrow H^+ + OH^-$	k2 × K1/[H2O][a]
2	$H^+ + OH^- \longrightarrow H_2O$	1.43×10^{11}
3	$H_2O_2 \longrightarrow H^+ + HO_2{}^-$	k4 × K2[a]
4	$H^+ + HO_2{}^- \longrightarrow H_2O_2$	5.0×10^{10}
5	$H_2O_2 + OH^- \longrightarrow HO_2{}^- + H_2O$	1.3×10^{10}
6	$HO_2{}^- + H_2O \longrightarrow H_2O_2 + OH^-$	k5×K1/K2×[H2O]
7	$eh^- + H_2O \longrightarrow H + OH^-$	1.9×10^1
8	$H + OH^- \longrightarrow e_h{}^- + H_2O$	2.2×10^7
9	$H \longrightarrow e_h{}^- + H^+$	k10 × K5[a]
10	$e_h{}^- + H^+ \longrightarrow H$	2.3×10^{10}
11	$OH + OH^- \longrightarrow O^- + H_2O$	1.3×10^{10}
12	$O^- + H_2O \longrightarrow OH + OH^-$	k11×K1/K3×[H2O]
13	$OH \longrightarrow O^- + H^+$	k14 × K3[a]
14	$O^- + H^+ \longrightarrow OH$	1.0×10^{11}
15	$HO_2 \longrightarrow O_2{}^- + H^+$	k16 × K4[a]
16	$O_2{}^- + H^+ \longrightarrow HO_2$	5.0×10^{10}

(continued on next page)

17	$HO_2 + OH^- \longrightarrow O_2^- + H_2O$	5.0×10^{10}
18	$O_2^- + H_2O \longrightarrow HO_2 + OH^-$	k17×K1/K4×[H2O]
Chemical Reactions		
19	$e_h^- + OH \longrightarrow OH^-$	3.0×10^{10}
20	$e_h^- + H_2O_2 \longrightarrow OH + OH^-$	1.1×10^{10}
21	$e_h^- + O_2^- + H_2O \longrightarrow HO_2^- + OH^-$	$1.3 \times 10^{10}/[H2O]^b$
22	$e_h^- + HO_2 \longrightarrow HO_2^-$	2.0×10^{10}
23	$e_h^- + O_2 \longrightarrow O_2^-$	1.9×10^{10}
24	$e_h^- + e_h^- + H_2O + H_2O \longrightarrow H_2 + OH^-$	$5.5 \times 10^9/[H2O]^2$ [c]
25	$e_h^- + H + H_2O \longrightarrow H_2 + OH^-$	$2.5 \times 10^{10}/[H2O]^b$
26	$e_h^- + HO_2^- \longrightarrow O^- + OH^-$	3.5×10^9
27	$e_h^- + O^- + H_2O \longrightarrow OH^- + OH^-$	$2.2 \times 10^{10}/[H2O]^b$
28	$e_h^- + O_3^- + H_2O \longrightarrow O_2 + OH^- + OH^-$	$1.6 \times 10^{10}/[H2O]^b$
29	$e_h^- + O_3 \longrightarrow O_3^-$	3.6×10^{10}
30	$H + H_2O \longrightarrow H_2 + OH$	1.1×10^1
31	$H + O^- \longrightarrow OH^-$	1.0×10^{10}
32	$H + HO_2^- \longrightarrow OH + OH^-$	9.0×10^7
33	$H + O_3^- \longrightarrow OH^- + O_2$	1.0×10^{10}
34	$H + H \longrightarrow H_2$	7.8×10^9
35	$H + OH \longrightarrow H_2O$	7.0×10^9
36	$H + H_2O_2 \longrightarrow OH + H_2O$	9.0×10^7
37	$H + O_2 \longrightarrow HO_2$	2.1×10^{10}
38	$H + HO_2 \longrightarrow H_2O$	1.8×10^{10}
39	$H + O_2^- \longrightarrow HO_2^-$	1.8×10^{10}
40	$H + O_3 \longrightarrow HO_3$	3.8×10^{10}
41	$OH + OH \longrightarrow H_2O_2$	3.6×10^9
42	$OH + HO_2 \longrightarrow H_2O + O_2$	6.0×10^9
43	$OH + O_2^- \longrightarrow OH^- + O_2$	8.2×10^9
44	$OH + H_2 \longrightarrow H + H_2O$	4.3×10^7
45	$OH + H_2O_2 \longrightarrow HO_2 + H_2O$	2.7×10^7
46	$OH + O^- \longrightarrow HO_2^-$	2.5×10^{10}
47	$OH + HO_2^- \longrightarrow HO_2 + OH^-$	7.5×10^9
48	$OH + O_3^- \longrightarrow O_3 + OH^-$	2.6×10^9
49	$OH + O_3^- \longrightarrow O_2^- + O_2^- + H^+$	6.0×10^9
50	$OH + O_3 \longrightarrow HO_2 + O_2$	1.1×10^8
51	$HO_2 + O_2^- \longrightarrow HO_2^- + O_2$	8.0×10^7
52	$HO_2 + HO_2 \longrightarrow H_2O_2 + O_2$	7.0×10^5
53	$HO_2 + O^- \longrightarrow O_2 + OH^-$	6.0×10^9
54	$HO_2 + H_2O_2 \longrightarrow OH + O_2 + H_2O$	5.0×10^{-1}
55	$HO_2 + HO_2^- \longrightarrow O + O_2 + OH^-$	5.0×10^{-1}
56	$HO_2 + O_3^- \longrightarrow O_2 + O_2 + OH^-$	6.0×10^9
57	$HO_2 + O_3 \longrightarrow HO_3 + O_2$	5.0×10^8
58	$O_2^- + O_2^- + H_2O + H_2O \longrightarrow H_2O_2 + O_2 + OH^-$	$1 \times 10^2/[H2O]^2$ [c]
59	$O_2^- + O^- + H_2O \longrightarrow O_2 + OH^- + OH^-$	$6 \times 10^8/[H2O]^b$
60	$O_2^- + H_2O_2 \longrightarrow OH + O_2 + OH^-$	1.3×10^{-1}
61	$O_2^- + HO_2^- \longrightarrow O^- + O_2 + OH^-$	1.3×10^{-1}
62	$O_2^- + O_3^- + H_2O \longrightarrow O_2 + O_2 + OH^-$	$1 \times 10^4/[H2O]^b$
63	$O_2^- + O_3 \longrightarrow O_3^- + O_2$	1.5×10^9

(continued on next page)

64	$O^- + O^- + H_2O \longrightarrow HO_2{}^- + OH^-$	$1 \times 10^9/[H2O]^b$
65	$O^- + O_2 \longrightarrow O_3{}^-$	3.6×10^9
66	$O^- + H_2 \longrightarrow H + OH^-$	8.0×10^7
67	$O^- + H_2O_2 \longrightarrow O_2{}^- + H_2O$	5.0×10^8
68	$O^- + HO_2{}^- \longrightarrow O_2{}^- + OH^-$	4.0×10^8
69	$O^- + O_3{}^- \longrightarrow O_2{}^- + O_2{}^-$	7.0×10^8
70	$O^- + O_3 \longrightarrow O_2{}^- + O_2$	5.0×10^9
71	$O_3{}^- \longrightarrow O_2 + O^-$	3.3×10^3 [a]
72	$O_3{}^- + H^+ \longrightarrow O_2 + OH$	9.0×10^{10}
73	$HO_3 \longrightarrow O_2 + OH$	1.1×10^5 [a]
74	$H_2O_2 \longrightarrow OH + OH^*$	4.4×10^{-9} [a]
75	$HO_2{}^- \longrightarrow O^- + OH^*$	1.0×10^{-5} [a]

Table A.2: Table provided by Elliot and McCracken assembled to model radiolysis of the primary heat transport in CANDU, PWR, and BWR nuclear power reactors. Note Equations #74,#75 are note relevant and thus not included in the modelling. Note that indices differ by 6 of those in Schneider et al.
[a] (s^{-1})
[b] ($M^{-2}s^{-1}$)
[c] ($M^{-3}s^{-1}$).

APPENDIX B

RADIOLYSIS SPUR MODEL

B.1. Setting for Initial Values

Initial spur distributions and diffusion constants parameters			
Species	Schwarz [65]		
	g^0 values (#M/100 eV)	r_0 (nm)	D ($\times 10^9\ m^2\ s^{-1}$)
${e_h}^-$	4.78	2.458	4.5
H^+	4.78	1.145	9.0
H	0.62	1.145	7.0
OH	5.7	1.145	2.8
H_2	0.15	1.145	4.5
H_2O_2	-	-	2.2
OH^-	-	-	5.0

Table B.1: Set of initial values for Schwarz model implementation. In the spur, both hydrogen peroxide (H_2O_2) and hydroxide ions (OH^-) exhibit an initial concentration of zero.

Initial spur distributions and diffusion constants parameters			
Species	Trumbore [62]		
	g^0 values (#M/100 eV)	r_0 (nm)	D ($\times 10^9\ m^2\ s^{-1}$)
${e_h}^-$	4.7	2.309	4.5
H^+	4.7	2.121	10.0
H	0.8	2.121	8.0
OH	6.0	2.121	2.0
H_2	0.25	2.121	4.5
H_2O_2	-	-	1.4
OH^-	-	-	2.0

Table B.2: Set of initial values for Trumbore model implementation. In the spur, both hydrogen peroxide (H_2O_2) and hydroxide ions (OH^-) exhibit an initial concentration of zero.

B.2. Reactions and rate constants of chemical regime radiolysis

These equations represents the kinetic model of seven radiolytic initial species, $e_h{}^-$, H, OH, H^+,OH^-, H_2, H_2O_2 through g^0-values and the short-time kinetic reactions through conservation of mass for each species, accounting for production. Table B.3 lists the 10 reactions and rate constants included in the model.

Reaction Scheme of chemical regime		Schwarz [65]	Trumbore [62]
n°	Reaction	$k \times 10^{-10}$ $(M^{-1}\,s^{-1})$	
1	$H^+ + OH^- \rightarrow H_2O$	10.0	14.3
2	$e_h{}^- + H^+ \rightarrow H$	1.7	2.3
3	$e_h{}^- + OH \rightarrow OH^-$	2.5	3.0
4	$e_h{}^- + H_2O_2 \rightarrow OH + OH^-$	1.3	1.23
5	$e_h{}^- + e_h{}^- + H_2O + H_2O \rightarrow H_2 + OH^-$	0.55	0.50
6	$e_h{}^- + H + H_2O \rightarrow H_2 + OH^-$	2.5	3.0
7	$H + H \rightarrow H_2$	1.0	1.3
8	$H + OH \rightarrow H_2O$	2.0	3.2
9	$H + H_2O_2 \rightarrow OH + H_2O$	0.01	0.016
10	$OH + OH \rightarrow H_2O_2$	0.6	0.5
Scavenger Reactions (aerated water) [140]			
13	$H + O_2 \rightarrow O_2{}^-$	1.9	
14	$H^+ + O_2{}^- \rightarrow HO_2*$	2.1	
15	$e_h{}^- + O_2 \rightarrow O_2{}^-$	3.8	

Table B.3: Reaction scheme used for description of the chemical-diffusion regime of first microsecond.

BIBLIOGRAPHY

[1] Feynman, R. *Feynman and computation*; CRC Press, 2018; pp 63–76.

[2] Olabi, A. G.; Onumaegbu, C.; Wilberforce, T.; Ramadan, M.; Abdelkareem, M. A.; Al-Alami, A. H. Critical review of energy storage systems. *Energy* **2021**, *214*, 118987.

[3] Centi, G.; Perathoner, S. Catalysis by layered materials: A review. *Microporous and mesoporous materials* **2008**, *107*, 3–15.

[4] Bennett, C. H.; DiVincenzo, D. P. Quantum information and computation. *nature* **2000**, *404*, 247–255.

[5] Freundlich, M. M. Origin of the Electron Microscope: The history of a great invention, and of a misconception concerning the inventors, is reviewed. *Science* **1963**, *142*, 185–188.

[6] Ruska, E. The development of the electron microscope and of electron microscopy. *Reviews of modern physics* **1987**, *59*, 627.

[7] Abrams, I.; McBain, J. A closed cell for electron microscopy. *Science* **1944**, *100*, 273–274.

[8] Thiberge, S.; Nechushtan, A.; Sprinzak, D.; Gileadi, O.; Behar, V.; Zik, O.; Chowers, Y.; Michaeli, S.; Schlessinger, J.; Moses, E. Scanning electron microscopy of cells and tissues under fully hydrated conditions. *Proceedings of the National Academy of Sciences* **2004**, *101*, 3346–3351.

[9] De Jonge, N.; Ross, F. M. Electron microscopy of specimens in liquid. *Nature nanotechnology* **2011**, *6*, 695–704.

[10] Kim, B. H.; Yang, J.; Lee, D.; Choi, B. K.; Hyeon, T.; Park, J. Liquid-phase transmission electron microscopy for studying colloidal inorganic nanoparticles. *Advanced Materials* **2018**, *30*, 1703316.

[11] De Yoreo, J. J. In-situ liquid phase TEM observations of nucleation and growth processes. *Progress in Crystal Growth and Characterization of Materials* **2016**, *62*, 69–88.

[12] Parent, L. R.; Gnanasekaran, K.; Korpanty, J.; Gianneschi, N. C. 100th anniversary of macromolecular science viewpoint: polymeric materials by in situ liquid-phase transmission electron microscopy. *ACS Macro Letters* **2020**, *10*, 14–38.

[13] Yang, Y.; Feijóo, J.; Briega-Martos, V.; Li, Q.; Krumov, M.; Merkens, S.; De Salvo, G.; Chuvilin, A.; Jin, J.; Huang, H.; others Operando methods: A new era of electrochemistry. *Current Opinion in Electrochemistry* **2023**, 101403.

[14] Chao, H.-Y.; Venkatraman, K.; Moniri, S.; Jiang, Y.; Tang, X.; Dai, S.; Gao, W.; Miao, J.; Chi, M. In situ and emerging transmission electron microscopy for catalysis research. *Chemical Reviews* **2023**, *123*, 8347–8394.

[15] Yuk, J. M.; Park, J.; Ercius, P.; Kim, K.; Hellebusch, D. J.; Crommie, M. F.; Lee, J. Y.; Zettl, A.; Alivisatos, A. P. High-resolution EM of colloidal nanocrystal growth using graphene liquid cells. *Science* **2012**, *336*, 61–64.

[16] Park, J.; Koo, K.; Noh, N.; Chang, J. H.; Cheong, J. Y.; Dae, K. S.; Park, J. S.; Ji, S.; Kim, I.-D.; Yuk, J. M. Graphene liquid cell electron microscopy: Progress, applications, and perspectives. *ACS nano* **2021**, *15*, 288–308.

[17] Clark, N.; Kelly, D. J.; Zhou, M.; Zou, Y.-C.; Myung, C. W.; Hopkinson, D. G.; Schran, C.; Michaelides, A.; Gorbachev, R.; Haigh, S. J. Tracking single adatoms in liquid in a transmission electron microscope. *Nature* **2022**, *609*, 942–947.

[18] Jonaid, G.; Dearnaley, W. J.; Casasanta, M. A.; Kaylor, L.; Berry, S.; Dukes, M. J.; Spilman, M. S.; Gray, J. L.; Kelly, D. F. High-Resolution Imaging of Human Viruses in Liquid Droplets. *Advanced Materials* **2021**, *33*, 2103221.

[19] Abellan, P.; Woehl, T.; Parent, L.; Browning, N.; Evans, J.; Arslan, I. Factors influencing quantitative liquid (scanning) transmission electron microscopy. *Chemical Communications* **2014**, *50*, 4873–4880.

[20] Woehl, T. J.; Moser, T.; Evans, J. E.; Ross, F. M. Electron-beam-driven chemical processes during liquid phase transmission electron microscopy. *MRS Bulletin* **2020**, *45*, 746–753.

[21] Fritsch, B.; Hutzler, A.; Wu, M.; Khadivianazar, S.; Vogl, L.; Jank, M. P.; März, M.; Spiecker, E. Accessing local electron-beam induced temperature changes during in situ liquid-phase transmission electron microscopy. *Nanoscale Advances* **2021**, *3*, 2466–2474.

[22] Gupta, T.; Schneider, N. M.; Park, J. H.; Steingart, D.; Ross, F. M. Spatially dependent dose rate in liquid cell transmission electron microscopy. *Nanoscale* **2018**, *10*, 7702–7710.

[23] Schneider, N. M.; Norton, M. M.; Mendel, B. J.; Grogan, J. M.; Ross, F. M.; Bau, H. H. Electron–water interactions and implications for liquid cell electron microscopy. *The Journal of Physical Chemistry C* **2014**, *118*, 22373–22382.

[24] Ziegler, J. F. SRIM-2003. *Nuclear instruments and methods in physics research section B: Beam interactions with materials and atoms* **2004**, *219*, 1027–1036.

[25] Woehl, T.; Abellan, P. Defining the radiation chemistry during liquid cell electron microscopy to enable visualization of nanomaterial growth and degradation dynamics. *Journal of microscopy* **2017**, *265*, 135–147.

[26] Grogan, J. M.; Schneider, N. M.; Ross, F. M.; Bau, H. H. Bubble and pattern formation in liquid induced by an electron beam. *Nano letters* **2014**, *14*, 359–364.

[27] Abellan, P.; Gautron, E.; LaVerne, J. A. Radiolysis of Thin Water Ice in Electron Microscopy. *The Journal of Physical Chemistry C* **2023**, *127*, 15336–15345.

[28] Merkens, S.; De Salvo, G.; Chuvilin, A. The effect of flow on radiolysis in liquid phase-TEM flow cells. *Nano Express* **2023**, *3*, 045006.

[29] Fritsch, B.; Zech, T. S.; Bruns, M. P.; Körner, A.; Khadivianazar, S.; Wu, M.; Zargar Talebi, N.; Virtanen, S.; Unruh, T.; Jank, M. P.; others Radiolysis-Driven Evolution of Gold Nanostructures–Model Verification by Scale Bridging In Situ Liquid-Phase Transmission Electron Microscopy and X-Ray Diffraction. *Advanced Science* **2022**, *9*, 2202803.

[30] Elliot, A. J.; McCracken, D. R. Computer modelling of the radiolysis in an aqueous lithium salt blanket: Suppression of radiolysis by addition of hydrogen. *Fusion engineering and design* **1990**, *13*, 21–27.

[31] Buxton, G. V.; Greenstock, C. L.; Helman, W. P.; Ross, A. B. Critical Review of rate constants for reactions of hydrated electrons, hydrogen atoms and hydroxyl radicals (OH/ O- in Aqueous Solution. *Journal of physical and chemical reference data* **1988**, *17*, 513–886.

[32] Hill, M.; Smith, F. Calculation of initial and primary yields in the radiolysis of water. *Radiation physics and chemistry* **1994**, *43*, 265–280.

[33] Abbe, E. Beiträge zur Theorie des Mikroskops und der mikroskopischen Wahrnehmung. *Archiv für mikroskopische Anatomie* **1873**, *9*, 413–468.

[34] Goodhew, P. J.; Humphreys, J. *Electron microscopy and analysis*; CRC press, 2000.

[35] Rudenberg, H. G.; Rudenberg, P. G. *Advances in Imaging and Electron Physics*; Elsevier, 2010; Vol. 160; pp 207–286.

[36] De Broglie, L. Recherches sur la théorie des quanta. Ph.D. thesis, Migration-université en cours d'affectation, 1924.

[37] Broglie, L. d. XXXV. A tentative theory of light quanta. *The London, Edinburgh, and Dublin Philosophical Magazine and Journal of Science* **1924**, *47*, 446–458.

[38] Egerton, R. F.; others *Physical principles of electron microscopy*; Springer, 2005; Vol. 56.

[39] Rose, A. *Advances in Electronics and electron Physics*; Elsevier, 1948; Vol. 1; pp 131–166.

[40] Libera, M. R.; Egerton, R. F. Advances in the transmission electron microscopy of polymers. *Polymer Reviews* **2010**, *50*, 321–339.

[41] Carter, C. B.; Williams, D. B. *Transmission electron microscopy: Diffraction, imaging, and spectrometry*; Springer, 2016.

[42] Egerton, R.; Malac, M. EELS in the TEM. *Journal of Electron Spectroscopy and Related Phenomena* **2005**, *143*, 43–50.

[43] Bruchhaus, L.; Mazarov, P.; Bischoff, L.; Gierak, J.; Wieck, A.; Hövel, H. Comparison of technologies for nano device prototyping with a special focus on ion beams: A review. *Applied Physics Reviews* **2017**, *4*.

[44] Egerton, R.; Li, P.; Malac, M. Radiation damage in the TEM and SEM. *Micron* **2004**, *35*, 399–409.

[45] Hobbs, L. Radiation effects in analysis by TEM. *Introduction to analytical electron microscopy* **1987**, 399–445.

[46] Zubeltzu, J.; Chuvilin, A.; Corsetti, F.; Zurutuza, A.; Artacho, E. Knock-on damage in bilayer graphene: indications for a catalytic pathway. *Physical Review B—Condensed Matter and Materials Physics* **2013**, *88*, 245407.

[47] Egerton, R. Radiation damage to organic and inorganic specimens in the TEM. *Micron* **2019**, *119*, 72–87.

[48] Mould, R. Röntgen and the discovery of X-rays. *The British journal of radiology* **1995**, *68*, 1145–1176.

[49] Allen, A. Radiation chemistry of aqueous solutions. *The Journal of Physical Chemistry* **1948**, *52*, 479–490.

[50] Jonah, C. D.; Kroh, J. Early Developments in Radiation Chemistry. *Radiation Research* **1990**, *123*, 239.

[51] Hart, E. J.; Boag, J. W. Absorption spectrum of the hydrated electron in water and in aqueous solutions. *Journal of the American Chemical Society* **1962**, *84*, 4090–4095.

[52] Le Caër, S. Water radiolysis: influence of oxide surfaces on H2 production under ionizing radiation. *Water* **2011**, *3*, 235–253.

[53] Pimblott, S. M.; LaVerne, J. A. Molecular product formation in the electron radiolysis of water. *Radiation research* **1992**, *129*, 265–271.

[54] Magee, J. L. Theory of Radiation Chemistry. I. Some Effects of Variation in Ionization Density1, 2. *Journal of the American Chemical Society* **1951**, *73*, 3270–3275.

[55] Samuel, A. H.; Magee, J. L. Theory of radiation chemistry. II. Track effects in radiolysis of water. *The Journal of Chemical Physics* **1953**, *21*, 1080–1087.

[56] Ganguly, A.; Magee, J. Theory of radiation chemistry. III. Radical reaction mechanism in the tracks of ionizing radiations. *The Journal of Chemical Physics* **1956**, *25*, 129–134.

[57] Mozumder, A.; Magee, J. Model of tracks of ionizing radiations for radical reaction mechanisms. *Radiation research* **1966**, *28*, 203–214.

[58] Mozumder, A.; Magee, J. Theory of radiation chemistry. VII. Structure and reactions

in low LET tracks. *The Journal of Chemical Physics* **1966**, *45*, 3332–3341.

[59] Bethe, H. A.; Ashkin, J.; others Experimental nuclear physics. *Wiley, New York* **1953**,

[60] Pimblott, S. M.; LaVerne, J. A.; Mozumder, A.; Green, N. J. Structure of electron tracks in water. 1. Distribution of energy deposition events. *Journal of Physical Chemistry* **1990**, *94*, 488–495.

[61] LaVerne, J. A.; Pimblott, S. M. Electron energy-loss distributions in solid, dry DNA. *Radiation research* **1995**, *141*, 208–215.

[62] Trumbore, C. N.; Short, D. R.; Fanning Jr, J. E.; Olson, J. H. Effects of pulse dose on hydrated electron decay kinetics in the pulse radiolysis of water. A computer modeling study. *The Journal of Physical Chemistry* **1978**, *82*, 2762–2767.

[63] Jonah, C.; Matheson, M.; Miller, J.; Hart, E. Yield and decay of the hydrated electron from 100 ps to 3 ns. *The Journal of Physical Chemistry* **1976**, *80*, 1267–1270.

[64] Jonah, C. D.; Miller, J. R. Yield and Decay of the Hydroxyl Radical from 200ps to 3ns. *The Journal of Physical Chemistry* **1977**, *81*, 1974–1976.

[65] Schwarz, H. A. The effect of solutes on the molecular yields in the radiolysis of aqueous solutions1. *Journal of the American Chemical Society* **1955**, *77*, 4960–4964.

[66] Kuppermann, A.; Belford, G. G. Diffusion kinetics in radiation chemistry. I. Generalized formulation and criticism of diffusion model. *The Journal of Chemical Physics* **1962**, *36*, 1412–1426.

[67] Schwarz, H. A. Applications of the spur diffusion model to the radiation chemistry of aqueous solutions. *The Journal of Physical Chemistry* **1969**, *73*, 1928–1937.

[68] Green, N. J.; Pilling, M. J.; Clifford, P.; Burns, W. G. Stochastic and deterministic models of spur kinetics. Initial distributions and comparisons. *Journal of the Chemical Society, Faraday Transactions 1: Physical Chemistry in Condensed Phases* **1984**, *80*, 1313–1322.

[69] Burns, W.; Sims, H.; Goodall, J. Radiation chemical diffusion kinetic calculations with prescribed and non-prescribed diffusion—I: Spherical and cylindrical cases. *Radiation Physics and Chemistry (1977)* **1984**, *23*, 143–180.

[70] Chance, E.; Jones, I.; Kirby, C.; Curtis, A. *FACSIMILE: a computer program for flow and chemistry simulation, and general initial value problems*; 1977.

[71] Brenner, D. J. Stochastic calculations of the fast decay of the hydrated electron in the presence of scavengers—tests of model consistency. *International Journal of Radiation Applications and Instrumentation. Part C. Radiation Physics and Chemistry* **1988**, *32*, 157–162.

[72] Green, N. J.; Pilling, M. J.; Pimblott, S. M. Stochastic models of short-time kinetics

in irradiated liquids. *International Journal of Radiation Applications and Instrumentation. Part C. Radiation Physics and Chemistry* **1989**, *34*, 105–114.

[73] Short, D. R.; Trumbore, C. N.; Olson, J. H. Extension of a spur overlap model for the radiolysis of water to include high linear energy transfer regions. *The Journal of Physical Chemistry* **1981**, *85*, 2328–2335.

[74] Pimblott, S. M.; LaVerne, J. A. Comparison of stochastic and deterministic methods for modeling spur kinetics. *Radiation research* **1990**, *122*, 12–23.

[75] Pimblott, S. M.; LaVerne, J. A. Effect of electron energy on the radiation chemistry of liquid water. *Radiation research* **1998**, *150*, 159–169.

[76] Pastina, B.; LaVerne, J. A. Effect of molecular hydrogen on hydrogen peroxide in water radiolysis. *The Journal of Physical Chemistry A* **2001**, *105*, 9316–9322.

[77] Bronskill, M.; Hunt, J. W. Pulse-radiolysis system for the observation of short-lived transients. *The Journal of Physical Chemistry* **1968**, *72*, 3762–3766.

[78] Muroya, Y.; Lin, M.; Wu, G.; Iijima, H.; Yoshii, K.; Ueda, T.; Kudo, H.; Katsumura, Y. A re-evaluation of the initial yield of the hydrated electron in the picosecond time range. *Radiation Physics and Chemistry* **2005**, *72*, 169–172.

[79] Porter, G.-N. Flash photolysis and spectroscopy. A new method for the study of free radical reactions. *Proceedings of the Royal Society of London. Series A. Mathematical and Physical Sciences* **1950**, *200*, 284–300.

[80] Bartels, D. M.; Cook, A. R.; Mudaliar, M.; Jonah, C. D. Spur decay of the solvated electron in picosecond radiolysis measured with time-correlated absorption spectroscopy. *The Journal of Physical Chemistry A* **2000**, *104*, 1686–1691.

[81] Hagberg, A.; Conway, D. Networkx: Network analysis with python. *URL: https://networkx. github. io* **2020**,

[82] Schneider, N. M. Electron beam effects in liquid cell TEM and STEM. *liquid cell electron microscopy* **2016**, *140*.

[83] Liu, L.; Sassi, M.; Zhang, X.; Nakouzi, E.; Kovarik, L.; Xue, S.; Jin, B.; Rosso, K. M.; De Yoreo, J. J. Understanding the mechanisms of anisotropic dissolution in metal oxides by applying radiolysis simulations to liquid-phase TEM. *Proceedings of the National Academy of Sciences* **2023**, *120*, e2101243120.

[84] Korpanty, J.; Parent, L. R.; Gianneschi, N. C. Enhancing and mitigating radiolytic damage to soft matter in aqueous phase liquid-cell transmission electron microscopy in the presence of gold nanoparticle sensitizers or isopropanol scavengers. *Nano letters* **2021**, *21*, 1141–1149.

[85] Korpanty, J.; Wang, C.; Gianneschi, N. C. Upper critical solution temperature polymer assemblies via variable temperature liquid phase transmission electron microscopy and

liquid resonant soft X-ray scattering. *Nature Communications* **2023**, *14*, 3441.

[86] Ambrožič, B.; Prašnikar, A.; Hodnik, N.; Kostevšek, N.; Likozar, B.; Rožman, K. Ž.; Šturm, S. Controlling the radical-induced redox chemistry inside a liquid-cell TEM. *Chemical science* **2019**, *10*, 8735–8743.

[87] Fritsch, B.; Korner, A.; Couasnon, T.; Blukis, R.; Taherkhani, M.; Benning, L. G.; Jank, M. P.; Spiecker, E.; Hutzler, A. Tailoring the Acidity of Liquid Media with Ionizing Radiation: Rethinking the Acid–Base Correlation beyond pH. *The Journal of Physical Chemistry Letters* **2023**, *14*, 4644–4651.

[88] Crook, M. F.; Moreno-Hernandez, I. A.; Ondry, J. C.; Ciston, J.; Bustillo, K. C.; Vargas, A.; Alivisatos, A. P. EELS Studies of Cerium Electrolyte Reveal Substantial Solute Concentration Effects in Graphene Liquid Cells. *Journal of the American Chemical Society* **2023**, *145*, 6648–6657.

[89] Lee, J.; Nicholls, D.; Browning, N. D.; Mehdi, B. L. Controlling radiolysis chemistry on the nanoscale in liquid cell scanning transmission electron microscopy. *Physical Chemistry Chemical Physics* **2021**, *23*, 17766–17773.

[90] Binggeli, M.; Shen, T.-H.; Tileli, V. Simulating current distribution of oxygen evolution reaction in microcells using finite element method. *Journal of The Electrochemical Society* **2021**, *168*, 106508.

[91] Merkens, S.; De Salvo, G.; Kruse, J.; Modin, E.; Tollan, C.; Grzelczak, M.; Chuvilin, A. Quantification of reagent mixing in liquid flow cells for Liquid Phase-TEM. *Ultramicroscopy* **2023**, *245*, 113654.

[92] Zhang, Y.; Keller, D.; Rossell, M. D.; Erni, R. Formation of Au nanoparticles in liquid cell transmission electron microscopy: from a systematic study to engineered nanostructures. *Chemistry of Materials* **2017**, *29*, 10518–10525.

[93] Wang, M.; Park, C.; Woehl, T. J. Quantifying the nucleation and growth kinetics of electron beam nanochemistry with liquid cell scanning transmission electron microscopy. *Chemistry of Materials* **2018**, *30*, 7727–7736.

[94] Kelly, D. J.; Zhou, M.; Clark, N.; Hamer, M. J.; Lewis, E. A.; Rakowski, A. M.; Haigh, S. J.; Gorbachev, R. V. Nanometer resolution elemental mapping in graphene-based TEM liquid cells. *Nano letters* **2018**, *18*, 1168–1174.

[95] Buxton, G. V.; Mulazzani, Q. G. Radiation-Chemical Techniques. *Electron Transfer in Chemistry* **2001**, 503–557.

[96] Robberstad Møller-Nilsen, R. E.; Canepa, S.; Jensen, E.; Sun, H.; Moreno-Hernandez, I. A.; Yesibolati, M. N.; Alivisatos, A. P.; Mølhave, K. S. Quantifying Aqueous Radiolytic Products in Liquid Phase Electron Microscopy. *The Journal of Physical Chemistry C* **2023**, *127*, 15512–15522.

[97] Karamitros, M.; Brown, J.; Lampe, N.; Sakata, D.; Tran, N. H.; Shin, W.-G.;

Mendez, J. R.; Guatelli, S.; Incerti, S.; LaVerne, J. A. Implementing the Independent Reaction Time method in Geant4 for radiation chemistry simulations. *arXiv preprint arXiv:2006.14225* **2020**,

[98] Karamitros, M.; Luan, S.; Bernal, M. A.; Allison, J.; Baldacchino, G.; Davidkova, M.; Francis, Z.; Friedland, W.; Ivantchenko, V.; Ivantchenko, A.; others Diffusion-controlled reactions modeling in Geant4-DNA. *Journal of Computational Physics* **2014**, *274*, 841–882.

[99] Tian, Z.; Jiang, S. B.; Jia, X. Accelerated Monte Carlo simulation on the chemical stage in water radiolysis using GPU. *Physics in Medicine & Biology* **2017**, *62*, 3081.

[100] Dhatt, G.; Lefrançois, E.; Touzot, G. *Finite element method*; John Wiley & Sons, 2012.

[101] Chandran, R. *Finite element methods and their applications*; IntechOpen, 2020.

[102] Pryor, R. W. *Multiphysics modeling using COMSOL®: a first principles approach*; Jones & Bartlett Publishers, 2009.

[103] Fritsch, B.; Malgaretti, P.; Harting, J.; Mayrhofer, K. J.; Hutzler, A. Precision of radiation chemistry networks: Playing Jenga with kinetic models for liquid-phase electron microscopy. *Precision Chemistry* **2023**, *1*, 592–601.

[104] Joy, D.; Luo, S. An empirical stopping power relationship for low-energy electrons. *Scanning* **1989**, *11(4)*, 176–180.

[105] Tabata, T. A simple calculation for mean projected range of fast electrons. *Journal of Applied Physics* **1968**, *39*, 5342–5343.

[106] Wesseling, P. *Principles of computational fluid dynamics*; Springer Science & Business Media, 2009; Vol. 29.

[107] Uhlenbeck, G. E.; Ornstein, L. S. On the theory of the Brownian motion. *Physical review* **1930**, *36*, 823.

[108] Pozrikidis, C. *Fluid dynamics: theory, computation, and numerical simulation*; Springer Science & Business Media, 2009.

[109] Kirby, B. J. *Micro-and nanoscale fluid mechanics: transport in microfluidic devices*; Cambridge university press, 2010.

[110] Delplace, F. Laminar flow of Newtonian liquids in ducts of rectangular cross-section a model for both physics and mathematics. *Open Access J. Math. Theor. Phys.* **2018**, *1*, 198–201.

[111] Shewchuk, J. R. Triangle: Engineering a 2D quality mesh generator and Delaunay triangulator. Workshop on applied computational geometry. 1996; pp 203–222.

[112] Crowell, M. W. *Automated Installation Verification of COMSOL via LiveLink for MATLAB*; 2015.

[113] Nelli, F. *Python data analytics: Data analysis and science using PANDAs, Matplotlib and the Python Programming Language*; Apress, 2015.

[114] Leigh, G. J. *Principles of chemical nomenclature: a guide to IUPAC recommendations*; Royal Society of Chemistry, 2011.

[115] Atkins, P. W.; De Paula, J.; Keeler, J. *Atkins' physical chemistry*; Oxford university press, 2023.

[116] Petruk, A. A.; Allen, C.; Rivas, N.; Pichugin, K.; Sciaini, G. High flow rate nanofluidics for in-liquid electron microscopy and diffraction. *Nanotechnology* **2019**, *30*, 395703.

[117] van Omme, J. T.; Wu, H.; Sun, H.; Beker, A. F.; Lemang, M.; Spruit, R. G.; Maddala, S. P.; Rakowski, A.; Friedrich, H.; Patterson, J. P.; others Liquid phase transmission electron microscopy with flow and temperature control. *Journal of Materials Chemistry C* **2020**, *8*, 10781–10790.

[118] Wang, M.; Leff, A. C.; Li, Y.; Woehl, T. J. Visualizing ligand-mediated bimetallic nanocrystal formation pathways with in situ liquid-phase transmission electron microscopy synthesis. *Acs Nano* **2021**, *15*, 2578–2588.

[119] Yesibolati, M. N.; Laganá, S.; Kadkhodazadeh, S.; Mikkelsen, E. K.; Sun, H.; Kasama, T.; Hansen, O.; Zaluzec, N. J.; Mølhave, K. Electron inelastic mean free path in water. *Nanoscale* **2020**, *12*, 20649–20657.

[120] Merkens, S.; Tollan, C.; De Salvo, G.; Bejtka, K.; Fontana, M.; Chiodoni, A.; Kruse, J.; Iriarte-Alonso, M. A.; Grzelczak, M.; Seifert, A.; others Toward sub-second solution exchange dynamics in flow reactors for liquid-phase transmission electron microscopy. *Nature Communications* **2024**, *15*, 2522.

[121] Koo, K.; Li, Z.; Liu, Y.; Ribet, S. M.; Fu, X.; Jia, Y.; Chen, X.; Shekhawat, G.; Smeets, P. J.; Dos Reis, R.; others Ultrathin silicon nitride microchip for in situ/operando microscopy with high spatial resolution and spectral visibility. *Science Advances* **2024**, *10*, eadj6417.

[122] Beker, A. F.; Sun, H.; Lemang, M.; van Omme, J. T.; Spruit, R. G.; Bremmer, M.; Basak, S.; Garza, H. H. P. In situ electrochemistry inside a TEM with controlled mass transport. *Nanoscale* **2020**, *12*, 22192–22201.

[123] Koo, K.; Park, J.; Ji, S.; Toleukhanova, S.; Yuk, J. M. Liquid-Flowing Graphene Chip-Based High-Resolution Electron Microscopy. *Advanced Materials* **2021**, *33*, 2005468.

[124] Grogan, J. M.; Bau, H. H. The nanoaquarium: a platform for in situ transmission electron microscopy in liquid media. *Journal of Microelectromechanical Systems* **2010**, *19*, 885–894.

[125] Tileli, V. Quasi-operando Transmission Electron Microscopy Diagnostics for Electrocatalytic Processes in Liquids. *Chimia* **2024**, *78*, 339–343.

[126] Klein, K. L.; Anderson, I. M.; De Jonge, N. Transmission electron microscopy with a liquid flow cell. *Journal of microscopy* **2011**, *242*, 117–123.

[127] Muller, D. A. Structure and bonding at the atomic scale by scanning transmission electron microscopy. *Nature materials* **2009**, *8*, 263–270.

[128] Carter, D. B. W. C. B. *Transmission electron microscopy A textbook for materials science*; 2009.

[129] Browning, N.; Buban, J.; Chi, M.; Gipson, B.; Herrera, M.; Masiel, D.; Mehraeen, S.; Morgan, D.; Okamoto, N.; Ramasse, Q.; others The application of scanning transmission electron microscopy (STEM) to the study of nanoscale systems. *Modeling nanoscale imaging in electron microscopy* **2012**, 11–40.

[130] Sang, X.; Lupini, A. R.; Unocic, R. R.; Chi, M.; Borisevich, A. Y.; Kalinin, S. V.; Endeve, E.; Archibald, R. K.; Jesse, S. Dynamic scan control in STEM: spiral scans. *Advanced Structural and Chemical Imaging* **2016**, *2*, 1–8.

[131] Zečević, J.; Hermannsdörfer, J.; Schuh, T.; de Jong, K. P.; de Jonge, N. Anisotropic shape changes of silica nanoparticles induced in liquid with scanning transmission electron microscopy. *Small* **2017**, *13*, 1602466.

[132] Stevens, A.; Yang, H.; Carin, L.; Arslan, I.; Browning, N. D. The potential for Bayesian compressive sensing to significantly reduce electron dose in high-resolution STEM images. *Microscopy* **2014**, *63*, 41–51.

[133] Belloni, J. Nucleation, growth and properties of nanoclusters studied by radiation chemistry: application to catalysis. *Catalysis today* **2006**, *113*, 141–156.

[134] Dissanayake, T. U.; Woehl, T. J. Liquid Phase Transmission Electron Microscopy Visualization of Surface Pattern Formation during Chemical Reaction Driven Assembly of Nanoparticles. *Microscopy and Microanalysis* **2022**, *28*, 1828–1830.

[135] Meijerink, M. J.; Spiga, C.; Hansen, T. W.; Damsgaard, C. D.; de Jong, K. P.; Zečević, J. Nanoscale imaging and stabilization of silica nanospheres in liquid phase transmission electron microscopy. *Particle & Particle Systems Characterization* **2019**, *36*, 1800374.

[136] Woehl, T. J.; Evans, J. E.; Arslan, I.; Ristenpart, W. D.; Browning, N. D. Direct in situ determination of the mechanisms controlling nanoparticle nucleation and growth. *ACS nano* **2012**, *6*, 8599–8610.

[137] Körner, A.; Fritsch, B.; Morales, A. L.; Malgaretti, P.; Hutzler, A. Panta Rhei-Tuning Silver Nanostructure Evolution with Flow in Liquid Phase Stem.

[138] Spitzmüller, L.; Nitschke, F.; Rudolph, B.; Berson, J.; Schimmel, T.; Kohl, T. Dis-

solution control and stability improvement of silica nanoparticles in aqueous media. *Journal of Nanoparticle Research* **2023**, *25*, 40.

[139] Alexander, G. B.; Heston, W.; Iler, R. K. The solubility of amorphous silica in water. *The Journal of Physical Chemistry* **1954**, *58*, 453–455.

[140] LaVerne, J. A.; Pimblott, S. M. Scavenger and time dependences of radicals and molecular products in the electron radiolysis of water: examination of experiments and models. *The Journal of Physical Chemistry* **1991**, *95*, 3196–3206.

[141] El Omar, A. K.; Schmidhammer, U.; Jeunesse, P.; Larbre, J.-P.; Lin, M.; Muroya, Y.; Katsumura, Y.; Pernot, P.; Mostafavi, M. Time-dependent radiolytic yield of OH• radical studied by picosecond pulse radiolysis. *The Journal of Physical Chemistry A* **2011**, *115*, 12212–12216.

[142] Arble, C.; Guo, H.; Strelcov, E.; Hoskins, B.; Zeller, P.; Amati, M.; Gregoratti, L.; Kolmakov, A. Radiation damage of liquid electrolyte during focused X-ray beam photoelectron spectroscopy. *Surface Science* **2020**, *697*, 121608.